

**Non-invasive Estimation of an Arterial Input function for Quantitative Positron
Emission Tomography using a Wrist Scanner**

A Thesis Presented

by

Aarti Kriplani

to

The Graduate School

in Partial fulfillment of the

Requirements

for the Degree of

Doctor of Philosophy

in

Biomedical Engineering

Stony Brook University

December 2007

Copyright by
Aarti Kriplani
December 2007

**State University of New York
at Stony Brook**

The Graduate School

Aarti Kriplani

We, the thesis committee for the above candidate for the

Dr. of Philosophy degree,

hereby recommend acceptance of this thesis.

David Schlyer, Thesis Advisor

Joanna Fowler, Prof. of Chemistry program

Paul Vaska, Asst. Prof. of BME program

Craig Woody, Physicist of Brookhaven National Laboratory

Terry Button, Prof. of BME program

Jean Logan, Prof. of BME program

This thesis is accepted by the Graduate School

Dean of the Graduate School

Acknowledgements

It is a pleasure to thank the many people who made this thesis possible.

It is difficult to overstate my gratitude to my Ph.D. advisor, Dr. David Schlyer, for guiding me through the convoluted world of research. He has patiently taught, corrected and encouraged me in my work. Under his tutelage, I have groomed from a bachelor's to a doctoral student. Thank you for your guidance on this research topic, and on research and life in general.

I would like to extend my thanks to Dr. Paul Vaska for guiding discussions and for teaching me the intricacies of the field of Positron Emission Tomography. Also, each and every member of the RatCAP team for making my stay as a doctoral student educative and enjoyable.

I am also indebted to Dr. Joanna Fowler and Dr. Jean Logan for sharing their chemistry and modeling expertise. They have been a great inspiration to me and many women in the field of science.

With the help of many people, I was able to perform experiments and would like to thank Michael Schueller for cyclotron operations, Donald Warner for PET operations, Barbara Hubbard, Pauline Carter and Bud Jayne for nursing care, Payton King for plasma analysis and Colleen Shea, David Alexoff, Youwen Xu and Lisa Muench for radiotracer preparation. Thank you all!

I want to say a big 'thank you' to my husband, Vikas Desai for his unprecedented support, endless love and encouragement throughout this entire journey. Without whom I would have struggled to find the inspiration and motivation needed to complete this dissertation.

I want to thank my parents-in-law for their blessings and support.

Lastly, and most importantly, I wish to thank my parents, Manohar Kriplani and Sarla Kriplani and brother Anand Kriplani. They raised me, supported me, taught me, and loved me.

To them I dedicate this thesis.

Abstract of the Thesis

**Non-invasive Estimation of an Arterial Input function for Quantitative Positron
Emission studies using a Wrist Scanner**

by

Aarti Kriplani

Doctor of Philosophy

in

Biomedical Engineering

Stony Brook University

2007

Positron emission tomography (PET) is a widely-used Neuroimaging assessment tool that assists with disease diagnosis, treatment evaluation and study of brain function. In addition to its use for qualitative assessment, PET may also be used, especially for basic research and/or treatment evaluation, to provide quantitative estimates of physiological or metabolic parameters of interest. For such quantification, an input function, the administered radiotracer concentration in plasma, is required. Unfortunately, using current technology, the acquisition of this input function often demands invasive procedures that produce discomfort for the patient and a potential health risk for medical personnel. This thesis aims to develop and characterize a blood radioactivity scanner for noninvasive estimation of an input function. The detector module consists of a 32 element Lutetium oxyorthosilicate (LSO) crystal array coupled to an Avalanche Photodiode (APD). To establish the fundamental parameters required to meet the needs proposed in research and design methods, a simple two detector pair system was built. Preliminary work included detection of an input bolus of a radioactive tracer flowing through an arterial hole in a phantom representing the human wrist, determining the sensitivity and spatial resolution of the scanner. These initial tests helped characterize and optimally design the prototype. The prototype was then used in a real clinical setting for feasibility studies. Non negligible effects of partial volume and spillover were assessed and corrected for using a small animal full ring tomograph for the wrist scans and a brain tomograph for human internal carotid arteries. Venous samples were used to calibrate the image derived time activity curve and correct for unchanged radiotracer to obtain an input function. Monte Carlo based simulations were done to validate the use of a full ring tomograph for absolute quantification of radioactivity from the wrist arteries. Thus, an arterial input function can be obtained without arterial catheterization thereby greatly reducing patient discomfort while increasing medical personnel safety.

Table of Contents

List of figures.....	viii
List of tables	x
1. Introduction	1
2 Physiological Quantification of PET Data	4
2.1 Radioactivity Quantification Using PET	5
2.1.1 Image Acquisition and Reconstruction	5
2.1.2 Image Characteristics.....	23
2.2 Compartmental Modeling	24
2.2.1 Concepts of Compartmental Modeling.....	24
2.2.2 Input Function	27
2.2.3 Enzyme Kinetics.....	29
2.2.4 Compartmental Models	31
2.2.5 Parameter Estimates.....	33
2.3 PET Radiotracer Mechanisms and Models.....	40
2.3.1 ^{18}F -flourodeoxyglucose (FDG)	40
2.3.2 [^{11}C] Raclopride.....	43
2.3.3 [^{11}C] Clorgyline.....	46
3. Wrist Scanner: Characterization and Feasibility Studies	48
3.1 Overview	48
3.2 Introduction.....	49
3.2.1 Problem Definition.....	49
3.2.2 Specific Aims	50
3.2.3 Literature Review.....	50
3.3 Prototype Scanner	52
3.3.1 Light collection efficiency.....	53

3.3.2 Electronics and readout system.....	57
3.4 Preliminary experiments	60
3.4.1 Wrist Phantom.....	60
3.4.2 Detection Efficiency.....	61
3.4.3 Data Acquisition and Image Formation.....	67
3.4.4 Normalization	71
3.4.5 Resolution.....	73
3.4.6 Scatter fraction.....	76
3.4.7 Contrast	77
3.4.8 Count Rate Performance	78
3.5 Human Studies.....	79
3.6 Effects of Nearby Sources	82
3.7 Discussion	84
3.8 Conclusion	86
4. Tomographic Images of the Human Wrist using a Full Ring Tomograph	87
4.1 Overview.....	87
4.2 Specific Aims	88
4.3 Correction for Partial Volume and Spillover on ROIs.....	89
4.4 Region of Interest Analysis	92
4.5 Compartmental Analysis: Sokoloff Model	92
4.6 Results.....	93
4.6.1 MicroPET acquisitions of the wrist.....	93
4.6.2 Correction for Partial Volume and Spillover.....	94
4.6.3 Input functions direct comparisons	96
4.6.4 Metabolic rate of Glucose	99
4.7 Discussion.....	100
4.8 Conclusion.....	101
5. Derivation of a Blood Time-Activity Curve from Brain Images	102
5.1 Overview.....	102

5.2 Introduction	103
5.3 Materials and Methods.....	104
5.3.1 Correction for Partial Volume and Spillover on ROIs.....	104
5.3.2 Data Acquisition.....	104
5.3.3 Data Analysis.....	107
5.4 Results	110
5.4.1 Arterial and venous radioactivity concentration.....	110
5.4.2 % unchanged radiotracer	110
5.4.3 Correction for Partial Volume and Spillover.....	112
5.4.4 Image derived input function.....	115
5.4.5 Direct Comparison of Input functions.....	116
5.4.6 Compartmental models and Graphical Analyses.....	120
5.5 Discussion	121
5.6 Conclusion.....	124
 6. Comparison of Methods Studies	 125
6.1 Data Acquisition Consideration for Compartmental Modeling	125
6.2 Comparing the MicroPET scanner and Wrist Scanner.....	127
6.2.1 Considerations for a full ring tomograph.....	127
6.2.2 Full Ring Wrist Tomograph: Monte Carlo Simulations.....	128
6.3 Error estimates in Kinetic Parameters	131
6.4 Internal and External Dispersion:	134
6. 5 Methods of extracting the peak of an input function	135
6.5.1 Independent Component Analysis	135
6.5.2 Preprocessing of data	137
6.5.3 Fast ICA	137
6.5.4 Application of EPICA to Dynamic Wrist Images.....	140
6.5.5. ICA vs. ROI analysis	141
6.6 Future Work	142

Appendix A: Description of the commercial robot system used for metabolite analysis.

Appendix B: Catalog of Independent Component Analysis: Motivation, Derivation and Process

Bibliography

List of Figures

- Figure 1.1 Schematic structure of this thesis
- Figure 2.1 a. Types of coincidence events (depicted in axial view): Scatter (S), random (R) and true (T) coincidences.
- Figure 2.1 b. Prompts and delayed random coincidence windows with a window size $\pm\tau$
- Figure 2.2: One compartmental model
- Figure 2.3: Two compartmental model, Reversible
- Figure 2.4: Two compartmental model, Irreversible
- Figure 2.5: The transport and reaction pathways of FDG as compared to glucose in cerebral tissue.
- Figure 2.6 Three-compartment FDG model with four first order rate constants
- Figure 2.7 [^{11}C]raclopride Chemical Structure
- Figure 2.8 Chemical Structure of [^{11}C]clorgyline
- Figure 3.1 Wrist Scanner system
- Figure 3.2 Typical Ge-68 spectrum for an LSO array / APD channel.
- Figure 3.3 Diagram of the analog front end of the ASIC
- Figure 3.4a Data Acquisition
- Fig. 3.4b Coincidence timing resolution of the analog front end
- Figure 3.5 Wrist Phantom
- Figure: 3.6 Solid angle cover range of diameter 1.9 and 3.3 cm
- Figure 3.7: Vertical efficiency calculation for artery at a depth of 1.9 cm
- Figure 3.8 : Experimental setup for efficiency measurement.
- Figure 3.9 Determination of LLD threshold for detection of photo peak
- Figure 3.10: Basic flow of data acquisition and limited-angle projection used in formation of wrist images.
- Figure 3.11: Schematic of the focal plane algorithm used for reconstruction of the blood vessels.
- Figure 3.12 : Lines of response between detector pixels of 2 detectors.
- Figure 3.13: Formation of planar images
- Figure 3.14: Normalization: Planar image of detector efficiencies for the 2 detector pairs
- Figure 3.15: Validation of Normalization: Rod source
- Figure 3.16: Resolution: Line Spread Function
- Fig 3.17: Planar image resolution
- Figure 3.18: Experimental setup for scatter estimate
- Figure 3-19: Rates of true coincidences, random coincidences and noise equivalent counts as a function of activity concentration.
- Figure 3.20: Human Wrist Scan
- Figure 3.21: Planar images for a [^{18}F]FDG study.
- Figure 3.22: Time activity curves for arterial ROI, background ROI and subtracted curve.
- Figure: 3.23: Comparison of the TACs from the Wrist Scanner and Arterial samples
- Figure 4.1: Partial volume and Spillover Effects
- Figure 4.2 Sagittal and transaxial view of the wrist in the MicroPET
- Figure 4.3: Time activity curves from the MicroPET images for the arterial and surrounding tissue
- Figure 4.4: Derenzo and anti-Derenzo phantom used for RC calculation in the MicroPET

Figure 4.5: The recovery coefficients measured experimentally are compared with those derived analytically for the tubes of the Derenzo Phantom.

Figure 4.6: Variation in the recovery coefficient with the choice of the ROI diameter for a tube of a particular diameter

Figure 4.7: Image Derived input functions derived from wrist images are compared to the invasive arterial plasma input functions for five subjects.

Figure 4.8: MRGLc calculated for the 5 subjects compared for IDIF and arterial blood samples.

Figure 5.1: Schematic diagram of the phantom used for estimating RC for the ECAT HR+.

Figure 5.2: Coregistered PET-MR image for ROI tracing

Figure 5.3 Region of interest on the co-registered PET-MRI image.

Figure 5.4: Comparison of an arterial TAC with venous radioactivity concentration for [^{11}C]raclopride at 1, 5, 10 and 30 minutes.

Figure 5.5: The % unchanged radiotracer values of arterial and venous plasma samples for [^{11}C] Clorgyline and [^{11}C] Raclopride

Figure 5.6: Comparison between experimentally measured and analytically derived recovery coefficients for tubes of varying diameters

Figure 5.7: TOP: Variation in the recovery coefficient with a) the uncertainty in the diameter for the ECAT/HR+ (FWHM 6.8mm), and b) the choice of the ROI diameter for a tube of 5mm in diameter.

Figure 5.8: Comparison of Time activity curves from ROIs and invasive samples.

Figure 5.9: Plot compares the image derived TAC after corrections (partial volume effects, whole blood to plasma ratio and % unchanged radiotracer) with the invasive arterial samples

Figure 5.10: Peak differences between IDIF and AIF

Figure 5.11: Regression Plot for a [^{11}C]raclopride study comparing the integral under the curve for AIF and IDIF.

Figure 5.12: Plot shows the early peak time and overestimation for [^{11}C]clorgyline, indicating the danger of using carotid artery ROI past 5 minutes.

Figure 6.1: Process of obtaining an input function

Figure 6.2: Simulation Design

Figure 6.3: Estimated error bars for the sensitivity and partial volume effects for the 4 detector prototype.

Figure 6.4: Estimated error bars for the sensitivity and partial volume effects for the 16 detector full ring tomograph.

Figure 6.5: Temporal differences in the peak of the input functions

List of Tables

- Table 2.1: Properties of positron emitting isotope commonly used in PET studies.
- Table 2.2: Properties of Scintillators
- Table 3.1: Contrast for and SNR values for the venous return experiment.
- Table 3.2: Data from a measurement of count rate with sources inside and outside the field of view
- Table 4.1: Recover Coefficient and Spill over from the phantoms
- Table 4.2: Comparison of the input functions: Peak position, height and AUC
- Table 5.1: Average % difference between arterial and venous metabolite samples
- Table 5.2: Recovery coefficients of different size tubes for a ROI of half the diameter of the tube.
- Table 5.3: Comparison between the shape of the directly sampled and the corrected ROI-based blood time activity curves for a) [^{11}C]clorgyline b) [^{11}C]raclopride
- Table 5.4: Kinetic terms for [^{11}C]clorgyline using the arterial plasma input function and the image derived input function (n=4)
- Table 5.5: The Distribution Volumes (DV) for [^{11}C]raclopride using the invasive arterial plasma input function and the image derived input function. (n=5)
- Table 6.1: Comparison of advantages and disadvantages of methods related to this thesis
- Table 6.2: Simulated estimates of the Wrist Tomograph Sensitivity
- Table 6.3: Simulated resolution of the Wrist Tomograph compared with measured simulations of the MicroPET
- Table 6.4: Comparison between important parameters of the MicroPET and Wrist Scanner
- Table 6.5: Comparison CMRglu values for Arterial samples, MicroPET and simulated input functions for the Wrist Scanner

Chapter 1

Introduction

PET is an imaging technique that allows the *in vivo* measurement of tissue functions in animals and humans. After the administration of tracer quantities of a radiolabeled pharmaceutical, the distribution of radioactivity is followed over time with a temporal resolution of seconds and a spatial resolution of millimeters. Mathematical modeling techniques, like compartmental or graphical analyses, can then be applied to the dynamic images in order to extract physiological parameters of interest such as the rates of transport, metabolism or binding of radiotracers. This requires the accurate characterization of the function that describes the time course of radiotracer delivery to the tissue, known as the input function. The input function is usually derived from multiple blood samples drawn from an arterial cannula and processed to obtain the radiotracer concentration in plasma. Because this method is invasive, time consuming and prone to errors, it cannot always be implemented and practical alternatives are called for.

The goal of this work is the non-invasive estimation of an input function using a small PET scanner to quantify the radioactivity detected in the wrist arteries. While the idea of an independent scanner for the estimation of an image derived input function seemed like an ideal solution, the 4 detector prototype lacked characteristics, such as sensitivity for absolute quantification of radiotracer concentration needed in kinetic analyses. Access to a full ring tomograph, with higher sensitivity, allowed proof of principle studies. Because the caliber of the wrist arteries (~ 2 mm) is smaller than twice the spatial resolution of the tomograph (~ 2.6 mm), the radioactivity concentration extracted from these PET images must be corrected for partial volume and spillover. Furthermore, these values are prone to statistical noise due to small size of the regions of interest and the short time frames required to capture the rapidly changing time course of radioactivity concentration following a bolus injection of the radiotracer.

To make complete use of the wrist scanner data, a correction for the partitioning of radioactivity between plasma and erythrocytes as well as for peripheral metabolism of a radiotracer needs to be applied in order to extract the contribution of the injected radiotracer in plasma from the total radioactivity measured in the blood.

The structure of this thesis is illustrated in Figure 1.1. Chapter 2 gathers the general background information required to address the multi-faceted problem at hand. Section 2.1 explains how the radioactivity concentration in an object is measured using PET. Section 2.2 follows with an overview of mathematical modeling techniques most commonly applied to dynamic PET data. The interpretation of a PET study does not only rely on knowledge of the technical aspects of the data generation and processing, but as importantly, on the understanding of the biological aspects underlying the radiotracer in the study. Because there are three radiotracers used in the thesis, section 2.3 reviews the biochemical data and the mathematical models for these tracers. A non-invasive method to generate a plasma input function is developed in steps in the next three chapters. The feasibility of the method is first demonstrated in chapter 3 where basic characterization of the scanner is detailed. Chapter 4 provides a proof of principle evaluating the constraints of the 4 detector scanner. An equation correcting for partial volume effect is introduced. Chapter 5 refines the use of these corrections by employing the internal carotid arteries from human PET brain scans. This chapter completes the use of a non-invasive approach, correcting for the presence of metabolites of the parent radiotracer. It validates the use of venous blood samples to substitute for arterial blood samples. For the completeness of this thesis, it demonstrates a non invasive approach for estimating of a blood time activity curve, a less invasive calibration of the curve and correction for unchanged radiotracer for estimation of an input function. The thesis concludes with chapter 6 which wraps analysis and comparison of methods studied in the preceding chapters. Similarities, differences, constraints and practical implementations are compared for clinical implementation of the work derived from this thesis.

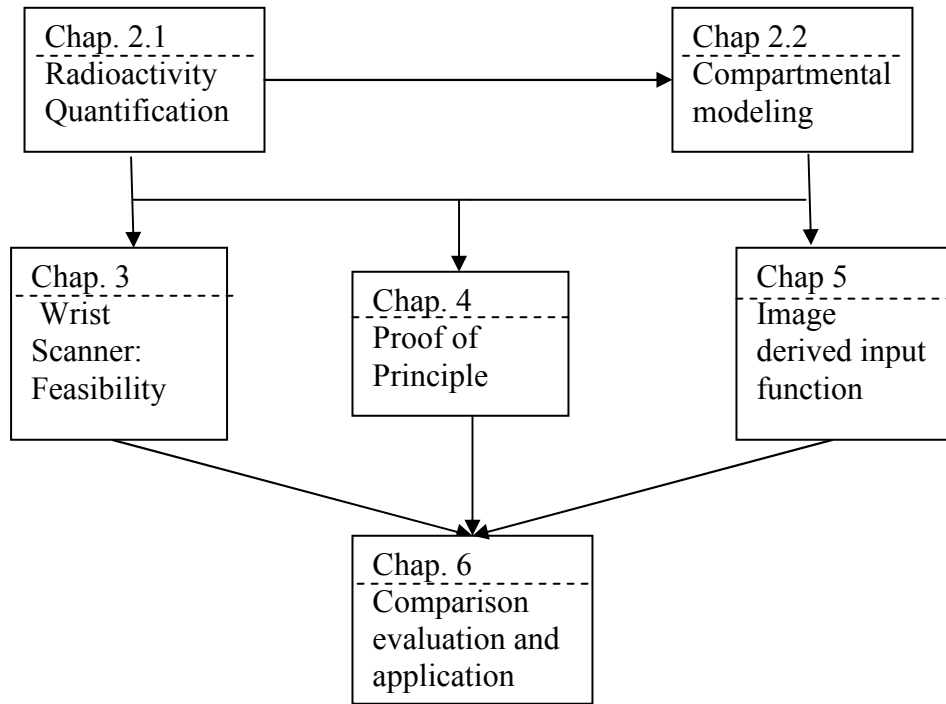


Figure 1.1 Schematic structure of this thesis

Chapter 2

Physiological Quantification of PET Data

Positron emission tomography (PET) is a Nuclear Medicine imaging technique that uses a dedicated tomograph to detect the annihilation photons emitted following the administration of a pharmaceutical labeled with a positron-emitting isotope. These molecules are designed to accumulate in the tissue of interest, and this accumulation and the rate of accumulation will ideally reflect specific physiological or biochemical processes. The acquired data are processed using reconstruction techniques to generate cross-sectional images of the spatio-temporal distribution of the radioactivity. PET studies aim at quantifying regional and/or global changes in tissue function, for example, between normal and disease states, or before and after treatment. The ability to detect these changes depends on the signal-to-noise characteristics of the PET data and the magnitude of the changes. One of the motivations behind the development of mathematical compartmental models is to increase the power to detect changes in the physiological parameters of interest brought about by different conditions (Carson, 1991). This is accomplished by explicitly accounting for changes in extraneous factors (e.g. radiotracer delivery), thus reducing intersubject variations. On the other hand, inaccuracies in the model itself can increase intersubject variations either by introducing biases due to incorrect assumptions, or by propagating errors from additional measurements required by the model (e.g. input function). The application of a mathematical model to PET data is beneficial if the variations that it removes override those that it produces. When significant physiological changes are detected, however, the model facilitates the quantification and interpretation of these changes.

This thesis is concerned with the extraction of regional information from PET images of the wrist (using the wrist scanner) and the brain (using a dedicated brain scanner) and the use of these data in the determination of physiological parameters that will distinguish between normal and disease states. This task requires that each voxel

value in the reconstructed image represents the absolute radioactivity concentration in the corresponding tissue volume. The acquisition and reconstruction of PET images are explained in section 2.1. Section 2.2 presents the compartmental modeling approaches used in the analysis of the calibrated PET data. The last section focuses on the quantification of the kinetics of the radiotracers concerned with the thesis, F-18 Fluoro-2-Deoxyglucose (F-18 FDG), C-11 Clorgyline and C-11 Raclopride.

2.1 Radioactivity Quantification Using PET

2.1.1 Image Acquisition and Reconstruction

The PET signal is generated in several steps and captured by a sophisticated radiation detection system. The detected signal also undergoes several processing steps in its transformation into a volumetric image representing the distribution of radioactivity concentration in tissues.

2.1.1.1 Signal Generation: The Radiotracers

Radiopharmaceuticals

A radiopharmaceutical is a radioactive compound which can be administered safely to humans for diagnosis or treatment purposes. It is usually made up of radioisotope bound to a pharmaceutical (a biomolecule or a drug). When used as an imaging agent, the decaying radioisotope emits the signal detected in PET, and the physico-chemical properties of the pharmaceutical determine the spatial distribution of the emitted signal. Radiopharmaceuticals which are not designed to interact with the system, but only to assess the function are called radiotracers. Ideally, the radiotracer would not perturb the physiological or biochemical pathways it is designed to measure. The lightest PET radioisotopes (^{11}C , ^{13}N , ^{15}O and ^{18}F) can be used to label organic compounds isotopically. Furthermore, the radiotracer should not elicit a pharmacological response. These radioisotopes can be produced in high specific activities so that very tiny amounts of the radiopharmaceutical can be administered. Their short half life means

that the radiation dose to the patient is usually quite small. It still remains that most often the magnitude of the amount of activity administered (and therefore the signal) is limited by the radiation dose given to the subject. On the other hand, the fast decay imposes restrictions on the production of the radioisotope - ideally on site using a dedicated particle accelerator or cyclotron - and on the speed and complexity of the chemical synthesis. PET radiochemistry has become very versatile, with the capacity to label a wide variety of biomolecules at many positions. However, the number of useful PET radiotracers is restricted since they must satisfy a number of criteria, the most important ones being selectivity to one or few pathways, delivery to the organ of interest, limited peripheral metabolism and suitable kinetics for the duration of a PET study (Pike, 1993).

Radioisotopes

Nuclei that contain an excess of protons decay either by electron capture or positron emission. In positron emission, a proton is converted to a neutron and a positive electron, called positron (β^+), is emitted along with an electronic neutrino (ν_e):



An orbital electron is also ejected so that the daughter nuclide remains neutral. Whereas any proton rich nucleus can decay by electron capture, only nuclei whose parent (A_ZX) mass exceeds the daughter (${}^A_{Z-1}Y$) mass by at least $1022 \text{ keV}/c^2$ - the combined mass of the positron and the ejected electron - can decay by positron emission, so that the two processes are in competition. The remainder of the mass difference is transformed into kinetic energy that is shared between the positron and the neutrino.

Positron interactions and Annihilation

In matter, the positron subsequently loses its kinetic energy by ionizing and exciting the surrounding material. Most energy is transferred by inelastic collisions with atomic electrons. When the positrons reach thermal energies, they start to interact with electrons either by annihilation, which produces two 511 keV photons which are anti-

parallel in the positron's frame, or by the formation of a hydrogen-like orbiting couple called positronium. In its ground-state, positronium has two forms - ortho-positronium, where the spins of the electron and positron are parallel, and para-positronium, where the spins are anti-parallel. Para-positronium again decays by self-annihilation, generating two anti-parallel 511 keV photons. Ortho-positronium self-annihilates by the emission of three photons (Evans, 1955). Both forms are susceptible to the pick-off process, where the positron annihilates with another electron. Free annihilation and the pick-off process are responsible for over 80% of the decay events. Variations in the momentum of the interacting particles result in an angular uncertainty in the direction of the 511 keV photons of around 4 mrad in the observer's frame (Rickey *et al* 1992). In a PET camera of diameter 1m and active transaxial FOV of 0.6m this results in a positional inaccuracy of 2-3 mm. The probability of positron emission (or the positron branching ratio), the positron energy and range in water for the radioisotopes commonly used in human PET studies are gathered in Table 2.1. The range values indicate that the position of the radiolabeled molecule at the time of the positron emission can be inferred with at best a precision of about 1 mm.

Table 2.1 Properties of positron emitting isotope commonly used in PET studies.

Isotope	Half Life (min)	β^+ branching ration	Maximum β^+ energy (Mev)	β^+ range in water (FWHM mm)
^{11}C	20.4	1	0.96	1.2
^{13}N	9.97	1	1.19	1.4
^{15}O	2.04	1	1.70	1.5
^{18}F	109.8	0.97	0.64	1.0
^{68}Ga	67.7	0.89	1.89	1.7
^{82}Rb	1.27	0.95	3.15	1.7

(Bailey et al, 1996)

Photon interactions

The annihilation photons further interact with the surrounding material, predominantly through the photoelectric effect or Compton scattering, pair production

not being energetically possible. The photoelectric effect occurs when a photon interacts with an atomic electron, most often bound in the K-shell. The photon is completely absorbed and the photoelectron is ejected with a kinetic energy equal to the difference between the photon energy and the electron binding energy. The probability of photoelectric absorption, τ , increases with the atomic number, Z of the surrounding material and decreases with the incident photon energy, $E\gamma$ approximately as $\tau \sim Z^5 / E\gamma^{3.5}$ (Knoll, 1989). In Compton scattering, the photon interacts with a free or weakly bound electron. The photon is deflected through an angle θ from its incident direction and transfers part of its initial energy to the recoil electron. The energy lost by the annihilation photon to the recoil electron in a single interaction varies between 0 at $\theta = 0^\circ$ to 341 keV at $\theta = 180^\circ$. For a wide range of materials, the probability of Compton scattering, α increases linearly with the atomic number of the surrounding material and falls gradually with the incident photon energy (Knoll, 1989). The scattered photon can undergo more interactions with the surrounding material, either another Compton scatter or a photoelectric absorption. The overall probability of interaction, called the linear attenuation coefficient, is the sum of the photoelectric absorption and Compton scattering probabilities, $\mu = \tau + \alpha$.

2.1.1.2 Signal Detection: The Tomograph

Detection systems are a key component of any imaging system, and an understanding of their properties is important for establishing appropriate operating criteria or designing schemes for obtaining quantitative information. In this section scintillation detection systems, which are used in the majority of PET tomographs, are discussed.

Detectors

The scintillation process involves the conversion of high-energy photons into visible light via interaction with a scintillating material, and consists of the following steps:

- 1) A photon incident on the scintillator creates an energetic electron, either by Compton scatter or by photoelectric absorption.
- 2) As the electron passes through the scintillator, it loses energy and excites other electrons in the process.
- 3) These excited electrons decay back to their ground state, giving off light as they do so. The higher the energy of the electron (and the photon that created it), the larger the number of collisions it must undergo to slow down and the more light that will be given off.

On the face of the crystal opposite to the face of photon incidence, a photomultiplier tube (PMT) collects the visible light and generates an amplified electronic pulse.

The choice of a detector material for PET is based on an ideal combination of properties. In order to determine precisely the position of the annihilation event, the size of each crystal should ideally be kept as small as possible. Because annihilation photons have a high probability of escaping from small detectors, the scintillator material must have a high stopping power if the detection efficiency is not to be compromised. Compton scattered photons have a lower energy than unscattered photons and discrimination between the two types of events requires good energy resolution from the scintillator which means an ideal scintillator will give off more light per unit energy deposited. At high count rates, the number of random coincidences and dead time losses (*see section Corrections for High Count Rates below*) is limited with a scintillator that offers good time resolution. The properties of some recent scintillators are shown in table 2.2.

Table 2.2 Properties of Scintillators

	LYSO	LSO	GSO	BGO
Decay time (ns)	53	40	60/600	60/300
(fast/slow ratio)			(7/1)	(1/10)
Light output(PMT)	75	75	20	15
Light Output (APD)	85	85	40	30
Peak Emission (nm)	420	420	430	480
Index of refraction	1.81	1.82	1.85	2.15
Density	5.37	7.35	6.71	7.13

Effective Z	54	65	58	73
1/μ 511 keV (mm)	20.0	12.3	15.0	11.6

Bismuth germanate ($\text{Bi}_4\text{Ge}_3\text{O}_{12}$ or BGO) has a high density (7.13 g/cm³) and a large effective atomic number ($Z=83$ for Bi), resulting in the largest probability per unit volume for photoelectric absorption of commonly available scintillation materials (Knoll, 1989). The high stopping power of BGO overrides its other less desirable properties of a relatively low light yield (15% of that of thallium activated sodium iodide (NaI(Tl))) and a slow light decay (300 ns). The slower scintillation process of BGO combined with its lower scintillation efficiency results in an overall time resolution that is about a factor of two worse than that of NaI(Tl) (FWHM=6.8 ns for BGO vs. 3.8 ns for NaI(Tl)) (Cho and Farukhi, 1977). Because fewer visible light photons are being produced per unit of energy deposited in the BGO crystal, its energy resolution is about a factor of two worse than that of NaI(Tl) (11% for BGO and 6% for NaI(Tl) at 662 keV) (Ludziejewski, 1995). With a density of 7.4 g/cm³ and an atomic number of $Z=71$ for Lu, cerium-doped lutetium oxyorthosilicate ($\text{Lu}_2(\text{SiO}_4)\text{O}:\text{Ce}$ or LSO) has a detection efficiency for annihilation photons comparable to that of BGO. Its much higher scintillation efficiency (>50% of that of NaI(Tl)) and faster scintillation process (decay time constant of 47 ns) compared to that of BGO yield a superior time resolution of 0.400 ns (FWHM) (Ludziejewski et al. 1995). Inconsistencies in the production of LSO in both light output and decay time have hampered the improvement in energy resolution of LSO over that of BGO (Karp, 2002). Because of its favorable combination of properties, LSO has superseded BGO as a detector material for PET in 3D mode (section Detection Geometry below) (Nutt 2002, Cherry 1997)

The performance of a detector for PET does not depend only on the material properties, but also on the detector design. By grooving a scintillator block into, for example, an eight by eight matrix of crystal elements coupled to four PMTs (Casey and Nutt, 1986), the block detector improves both the sampling frequency and detection efficiency over that of the single-crystal detector. The visible light is channeled down the individual crystal elements and distributed to the PMTs in different combinations by

slotting the block at increasing depths with increasing distance from the centre of the block. The crystal in which the interaction occurred is identified by comparing the sums of the outputs of adjacent PMTs. The output of all four PMTs is also summed and sent to a pulse processing unit, in order to determine the energy absorbed in the detector (from the pulse height,) and the time of arrival of the incident photon (from the pulse leading edge). This design, initially created for BGO, is also applied to LSO. More recently Avalanche photodiodes (APDs) are being employed as PET detectors. These are photodetectors that can be regarded as the semiconductor analog to photomultipliers. The main advantage of the avalanche photodiode over the usual photodiode is its internal gain, which can be 300X or higher. An APD is a type of photodiode that internally amplifies the photocurrent. The basic APD structure is a p-n junction under a reverse bias voltage. Near the pn junction the silicon becomes depleted of electrical charge. This is known as the depletion region. The thickness of the depletion region can be varied with the reverse voltage. Photons created in the scintillator enter the depletion region and create charge carriers that drift towards the electrodes. In APD's, the electric field is high enough to accelerate the charge carriers so that they can produce more electron-hole pairs by ionization. Hence, each photon can produce an avalanche of charge carriers.

Coincidence counting

When a positron annihilates, the mass is converted completely into energy and two annihilation photons are emitted simultaneously at $180^\circ \pm 0.25^\circ$ to each other. Coincidence events are detected by comparing the output of two detectors to a coincidence unit. Whenever two pulses are received within a given time interval, called the coincidence time window, a binary pulse is generated by the coincidence unit. The width of the coincidence time window is selected to include the time resolution of the detectors, time variations between branches due to additional electronic components in the detector circuits, and the maximum time that a photon can take to cross the entire field of view (FOV).

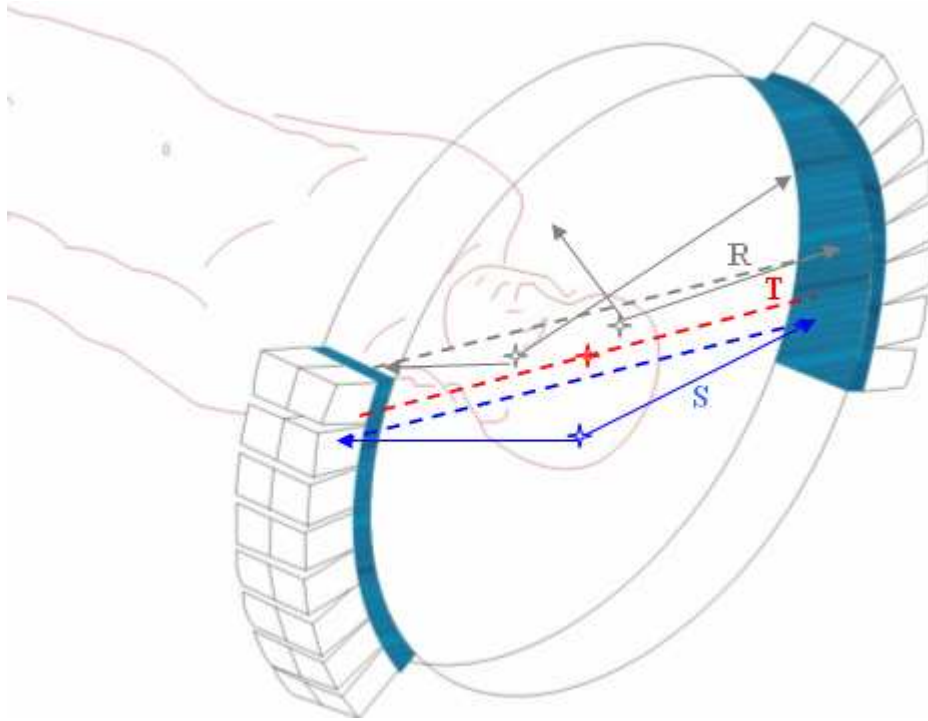


Figure 2.1a: Types of coincidence events (depicted in axial view): Scatter (S), random (R) and true (T) coincidences.

As illustrated in figure 2.1, three types of coincidence events are detected by the tomograph: True, scatter and random. If two photons created from the same annihilation event reach their respective detectors without being scattered, then a true coincidence is recorded. True coincidences are the events of interest since their count rate is proportional to the regional radioactivity concentration. If either or both photons are scattered while crossing the FOV; then a scatter coincidence can be detected. Scatter coincidences carry incorrect positioning information since the photon paths are no longer collinear. Due to the limited energy resolution of scintillators, many scattered photons successfully pass through the pulse processing unit. Even though the scattered photons travel an extra distance, they are not sufficiently delayed to fall outside the coincidence time window. A random coincidence occurs when two photons that originated from two different annihilation events are detected within the coincidence time window. The count rate of the random coincidences is proportional to the product of the count rate in the two individual detectors (singles), with the constant of proportionality given by the coincidence time window. Therefore, the random count rate increases faster than the true

count rate with increasing radioactivity in the FOV, but can be reduced by shortening the coincidence time window. More than two photons can strike the detectors within the coincidence time window. Even though these multiple coincidence events are not recorded, in most cases, they can prevent the detection of true coincidences while being processed (see Corrections for High Count Rates below).

Detection Geometry

The most common design for PET cameras makes use of the cylindrical geometry by stacking together individual rings of detectors. In the two-dimensional (2D) acquisition mode, annular septa are inserted between rings to shield most coincidence events that occur between non-adjacent rings. Coincidence events detected within the same rings form direct planes, whereas those detected between adjacent rings define cross planes. This configuration minimizes the detection of out-of-plane random and scatter coincidences. Removing inter ring septa eliminates physical collimation in the axial direction, thus allowing for more oblique coincidence events to be detected. The expansion to the three-dimensional (3D) acquisition mode increases the tomograph overall sensitivity to true coincidences, but also to random and scatter coincidences from both inside and outside the FOV (Cherry, 3rd edition).

Data Sampling

The near simultaneous detection of a pair of annihilation photons represents one event or count in the image. The line joining two detectors is called a line of response (LOR). An LOR represents the line integral through the radioactivity distribution connecting a given pair of detectors. All parallel LORs correspond to a projection of the radioactivity distribution. Multiple projections are obtained by rotating the set of parallel LORs. In 2D mode, an LOR, can thus be described by a radial distance x_r , from the center of the transaxial FOV and a projection angle θ . The number of events in each LOR is stored in a bin or element (x_r, θ) of a matrix called sinogram. The term sinogram is derived from the observation that a point source located off-center in the FOV traces a sine wave in the matrix of LOR values. In 2D mode, a sinogram is generated for each (direct and cross) plane. In 3D mode, a sinogram is generated for each ring pair. When

the sinograms are sparse matrices as is often the case in 3D mode, it becomes advantageous to store the data on an event-by-event basis called list mode. Information on the pair of detectors corresponding to the coincidence event together with the time of the events is recorded as the events are detected: and sorted into sinograms later once the data acquisition is completed.

2.1.1.3 Corrections

Not all annihilation events are detected as coincidence events. And not all coincidence events carry accurate positioning information. Corrections thus need to be applied to the total coincidence events in order to restore the linear relationship with the radioactivity concentration before recovering the radioactivity distribution.

High Count Rates

It takes a minimum time for a detection system, comprising the detector itself and the associated electronics; to generate and process an electronic pulse. If more than one event is detected within that time, called dead time, pulses are lost or distorted. The probability of losing an event is always present in PET because of the random nature of radioactive decay, but becomes increasingly significant at higher count rates. The large number of detectors and the complexity of the pulse processing and recording electronics render the modeling of the dead time behavior difficult (Moisan, 1997). Instead, a more *ad hoc* method is used to correct for dead time losses. The count rate response of the tomograph is characterized by counting a high activity source of known strength over several half lives. When a source of unknown activity is subsequently measured, the true source activity is obtained by interpolating the count rate response curve.

At count rates just below saturation of the detectors, the count rate is dominated by random coincidences. As the count rate decreases, a greater proportion of the count rate is attributed to true coincidences. Two methods are commonly used to estimate random events. If the coincidence time window is known accurately, the random coincidence rate can be calculated from the singles count rates at a pair of detectors. Alternatively, the random coincidence rate can be measured by introducing a variable

delay in one branch of the coincidence unit. The arrival times of the true (and scatter) events fall within the coincidence window, whereas the arrival times of the photons associated to random events are uniformly distributed in time and the number of random events is approximately equal from one coincidence window to the next. The delay is first adjusted such that the centre of the coincidence time window is aligned with the true (and scatter) coincidence peak; and all three types of coincidences are measured. The delay is then changed such that the coincidence time window is moved away from the peak and only random coincidences are measured (figure 2.1 b). Whether the random coincidences are calculated or measured, they are subtracted from the total coincidences. The singles method is more precise because the singles rates are much higher than the coincidence rates. Unlike the singles, the delayed coincidences are measured under the same conditions of dead time as the true coincidences, making the delayed window method more accurate (Casey and Hoffman, 1986).

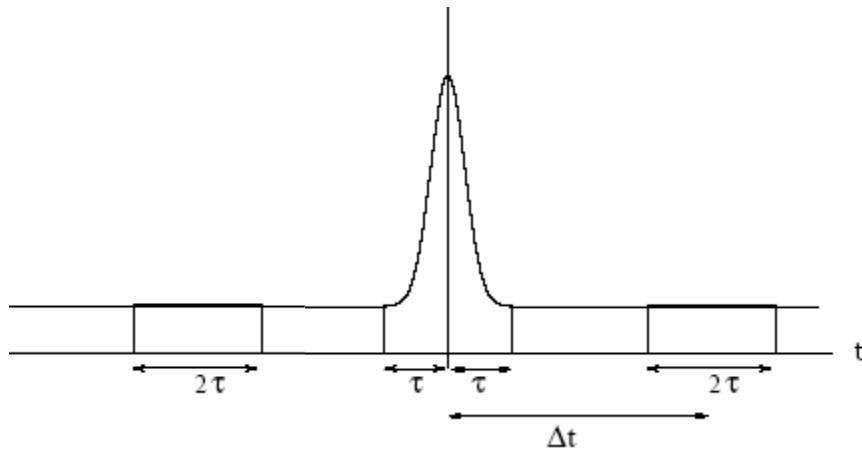


Figure 2.1 b. Prompts and random coincidence windows with a window size $\pm\tau$

If not corrected for, the effect of dead time is an underestimation of the radioactivity concentration in the reconstructed PET images whereas that of random coincidences is an overestimation (Hoffman, 1981). In dynamic PET studies, where the source activity in the FOV varies with time due to changes in the bio-distribution of the radiotracer and radioactive decay, the recovery of the count rate linearity between true coincidences and source activity is crucial.

Photon Attenuation and Scatter

Most annihilation photons emitted inside the body are scattered or absorbed on their way out. The probability P_i that a photon does not interact as it propagates through tissues is given by

$$P_i = \exp\left(\int_l -\mu(x)dx\right) \quad (2.2)$$

where $\mu(x)$ is the linear attenuation coefficient. The integral is evaluated along a path l defined by the pair of detectors i (located at a given distance x , from the center of the projection at a given angle θ). Since a pair of annihilation photons undergoes the same attenuation regardless of the origin of the annihilation event along the path, PET data can be corrected for attenuation before reconstruction, i.e. without knowledge of the radioactivity distribution.

A map of the survival probabilities can be obtained from two separate scans using an external radioactive source which is rotated about the center of the FOV. Prior to injection of the radiotracer, a transmission scan is performed while the subject is lying inside the tomograph. These data provide an estimate of the attenuated flux of photons (T_i) along each path. Under the same conditions as the transmission scan, a blank scan is acquired without anything in the tomograph. These data give an estimate of the incident flux of photons (B_i) along the same paths. The survival probabilities are approximated by the ratio of the two maps:

$$\hat{P} \sim \frac{T_i}{B_i} \quad (2.3)$$

When obtained using a positron emitting source ($^{68}\text{Ge}/^{68}\text{Ga}$), these estimates are noisy because the source strength must be kept low in order not to saturate the detector close to the source. This problem can be overcome by using a source emitting γ -rays of energy close to 511 keV (662 keV for ^{137}Cs) and sequentially switching off the detector close to the source. Corrections must be made for the diameter difference between the detector ring and the source orbit (DeKemp and Nahmias, 1994), and for the energy difference of the linear attenuation coefficients (Yu and Nahmias, 1995). For comparable statistics; the singles method is ten times faster than the coincidence method (Karp, 1995). The noise

propagation from the measured attenuation map to the emission data can be eliminated by segmenting the attenuation map and assigning theoretical values of linear attenuation coefficients to the corresponding anatomical regions (Xu, 1994).

The fraction of scatter coincidences is approximately 10-15% of total coincidences in 2D mode, but rises to 30-50% in 3D mode. The scatter fraction can be estimated using an analytical model of the radiation transport through an object from emission to detection (Watson, 1996; Ollinger, 1996). Given the attenuation map, a physical description of the tomograph and an initial estimate of the radioactivity distribution, the algorithm simulates the number of single scatters. The multiple scatter contribution can be modeled empirically from the single scatter distribution (Ollinger, 1996). Because of the presence of scatter in the preliminary emission image, the algorithm is run iteratively, correcting each time the estimate of the radioactivity distribution using the improved scatter estimate. This method fails to account for radioactivity outside the FOV since information is only available from inside the FOV. For brain PET studies, the scatter fraction can also be inferred from measurements of coincidence events made in a second lower energy window in addition to the photopeak window (Grootenck, 1996). A scaled subtraction of the two energy windows yields the number of scatter events in the upper energy window. This method offers the advantage of correcting for scatter events originating from radioactivity outside the FOV.

Mismatches between the true and assumed attenuation correction factors, e.g. due to subject movement, lead to image artifacts, particularly at the boundary between tissue of different densities, and to inaccurate estimates of the radioactivity concentration across the PET images (Huang, 1979). Residual scatter coincidences degrade the spatial resolution in the PET image by transferring radioactivity from high to low radioactivity regions (Watson, 1996). Whereas scatter correction can be omitted in 2D mode or compensated for by adjusting the linear attenuation coefficients; it is essential in 3D mode in order to obtain quantitative PET images.

Non-Uniform Detector Response

The detection efficiency of annihilation photons varies not only from block detector to block detector, but also across the elements of a block detector, depending on the location of the energy deposition in the crystal and the incidence angle of the photon. The detection efficiency of crystal elements located in the center of the block detector is higher than those located on the edges. Because Compton scattered photons have lower energies and more oblique incidence angles than unscattered photons, the detection efficiency is also different between the two types of coincidences (Ollinger, 1995). These differences are exacerbated in 3D mode with the larger scatter fraction and the wider range of acceptance angles than in 2D mode.

Normalization can be approached from two directions. In the direct method, a uniform low activity source illuminates sequentially all LORs. The measured data are inverted to provide an efficiency value for each LOR. Given the very large number of LORs in 3D mode, the acquisition time required to obtain good counting statistics for each LOR is prohibitively long. Component-based models of increasing complexity (Hoffman, 1989; Bailey, 1996; Badawi and Marsden, 1999) have been proposed along with measurement protocols in order to determine the main factors contributing to the efficiency separately. This indirect method allows for the effects of the individual factors to be investigated. Failure to correct for the differential detector response and geometric effects creates artifacts in PET images of a uniform cylindrical phantom - ranging from the addition of high frequency noise to low frequency characteristic (transaxial and axial) patterns - that can lead to severe quantification errors in the radioactivity distribution (Badawi and Marsden, 1999).

The number of annihilation events N_i originating from photons emitted at a given angle can be expressed as a function of the number of total coincidences Y_i , recorded in a pair of detectors i by combining the above described corrections in the appropriate sequence as summarized in the following equation (Ollinger and Fessler, 1997):

$$N_i = \frac{1}{d_i \eta_i^t \hat{P}_i} [Y_i - d_i \eta_i^r \hat{R}_i - d_i \eta_i^s \hat{S}_i] \quad (2.4)$$

where d_i is the probability of an event being lost due to dead time, P_i is the measured survival probability as previous defined (equations (2.2) and (2.3)), η_i are the detection probabilities of a true (superscript t); random (superscript r) or scatter (superscript s) events, and R_i and S_i are the estimated number of random and scatter coincidences. Note that the corrections for dead time, detector efficiency and photon attenuation are multiplicative while those for random and scatter coincidences are subtractive.

2.1.1.4 Signal Localization: Image Reconstruction

A pair of annihilation photons striking two opposite detectors connected in coincidence carries the information that an annihilation event occurred somewhere along the LOR. The point of origin of the annihilation event is inferred back by combining multiple LORs

2D Filtered Backprojection (FBP) Algorithm

In 2D mode, a projection $p(x_r, \theta)$ corresponds to a line integral at an angle θ and at a distance x_r , from the center of the FOV through the unknown radioactivity distribution $\lambda(x, y)$

$$p(x_r, \theta) = \int_l \lambda(x, y) dy_r \quad (2.5)$$

where (x_r, y_r) is the coordinate system (x, y) rotated by an azimuthal angle θ . Equation (2.5) describes the forward projection operation of the PET data acquisition process. The backprojection operation, given by equation (2.6), is the adjoint to the forward projection operation.

$$b(x, y) = \int_0^\pi p(x_r, \theta) d\theta \quad (2.6)$$

where $b(x, y)$ is the backprojected radioactivity distribution. Back projecting basically consists of assigning the value of the line integral to all the points that fall on the path of the line integral, and repeating this operation for all line integrals. Using the central-

section theorem which states that the 1D Fourier transform ($F_1\{\}$) of a projection at an angle θ is equivalent to a line through the origin of the 2D Fourier transform ($F_2\{\}$) of the original radioactivity distribution, the filtered backprojected radioactivity distribution can be calculated as

$$\lambda(x, y) = \int_0^\pi [p(x_r, \theta) \otimes h1(x_r)] d\theta \quad (2.7a)$$

$$= \int_0^\pi F_1^{-1}[\{|v_{xr}| F1\{p(x_r, \theta)\}\}] d\theta \quad (2.7b)$$

where $h1(x_r) = F_1^{-1}\{|v_{xr}|\}$ is the 1D filter kernel, and $|v_{xr}|$ is the ramp filter arising from the change of variables from rectangular to polar coordinates (the Jacobian of the transformation). In practice, the projections are sampled at discrete intervals Δx_r , setting the maximum recoverable frequency to Nyquist frequency $v_{\max} = (2\Delta x_r)^{-1}$. Furthermore, the projections are contaminated by high frequency noise which can be attenuated by multiplying the ramp filter with an apodizing window that rolls off the higher frequencies. A 3D volume image can then be formed by separately acquiring and reconstructing a set of 2D cross-sectional images, and stacking them together.

3D Reprojection (RP) Algorithm

Since the set of projections acquired in 2D mode is sufficient to reconstruct a 3D image, the additional projections collected in 3D mode provide redundant data that can be used to improve image variance. However, the finite axial extent of the PET scanner hinders the measurement of the complete set of projections in 3D. Kinahan and Rogers (1989) proposed to reconstruct the 3D volume image in two steps. First, reconstruct with the 2D FBP algorithm a first-pass image $\lambda_{2D}(x, y, z)$ from the subset of direct projections corresponding to the complete set of projection acquired in 2D, and use this image to forward project in 3D the missing projections. Then, reconstruct with the 3D FBP algorithm a second pass image $\lambda(x, y, z)$ from the merged set of measured and estimated projections in 3D. The 3D FBP algorithm is simply the extension of the 2D FBP

algorithm to one more dimension with the ramp filter being replaced by the Colsher filter (Colsher, 1980). This procedure is equivalent to extending the axial FOV of the PET scanner by adding virtual rings of detectors (Defrise, 1990). Image variance increases from the center to the periphery of the axial FOV, reflecting the axial variations in the tomograph sensitivity (Kinahan and Rogers, 1989). To restrict noise amplification, the Colsher filter can be multiplied by a 2D apodizing window.

Rebinning Algorithms

The time it takes to reconstruct a 3D volume image using the 3D reprojection algorithm is more than an order of magnitude longer than that to reconstruct the subset of direct projections using the 2D FBP algorithm (Defrise, 1997). If the 3D PET dataset, could be sorted or rebinned into a 2D dataset prior to reconstruction, the high sensitivity of the 3D acquisition mode could be combined with the fast computational speed of the 2D reconstruction algorithm to yield low variance images in short times. A number of rebinning algorithms have been developed for 3D PET data, e.g. the single-slice rebinning (SSRB) algorithm (Daube-Witherspoon and Muehllehner 1987; Erlandsson, 1994), the multi slice rebinning (MSRB) algorithm (Lewitt et al; 1994), and the approximate and exact Fourier rebinning (FORE and FOREX) algorithms (Defrise, 1995; Defrise et al, 1997), with varying degree of accuracy and computational speed.

Iterative Reconstruction

The FBP methods ignore the discrete nature of the data and the measurement noise, and further amplify (via the ramp and Colsher filters) the noise in the reconstructed PET images. In contrast, iterative reconstruction algorithms are based on models of the PET data acquisition process, incorporating the tomograph physical characteristics as well as the Poisson distributed measurement noise. The radioactivity distribution $\lambda(x)$ can be discretised into a finite set of basis functions $b_j(x)$, usually voxels:

$$\lambda(x) = \sum_{j=1}^p \theta_j b_j(x) \quad (2.8)$$

In the reconstruction, $\Theta = (\theta_j)$ are the unknown coefficients that must be computed from the comparison between the measured projection data Y_i and the model predictions $Y_i(\Theta)$:

$$Y_i(\Theta) = \sum_{j=1}^p a_{ij} \theta_j + s_i + r_i + e_i \quad (2.9)$$

where

$$a_{ij} = T \left(di \int p_i(x) b_j(x) dx \right) \quad (2.10)$$

Equations (2.9) and (2.10) are simply equation (2.4) rewritten in terms of counts over the scan time T (rather than count rates) and to which a term for measurement errors e_i was added. The point response of the detector pair $p_i(x)$ now combines the measured linear attenuation coefficients and detector (intrinsic and geometric) efficiency estimates, and represents the probability of a photon emitted at location x to be counted in detector pair i . Although a non-trivial problem, the system matrix $A = \{a_{ij}\}$ offers the possibility of accounting for the detector dimensions and the positron range in the reconstruction process. The random r_i and scatter s_i counts are estimated independently and incorporated into equation (2.9). Given the linear form of the model and measurement errors distributed as independent Poisson noise, the unknown coefficients can be estimated by maximizing the log-likelihood $L(\Theta)$ defined as:

$$L(\Theta) = \sum_{i=1}^n ((Y_i \ln Y_i(\Theta) - Y_i(\Theta) - \ln(Y_i!)) \quad (2.11)$$

Finding the maximum of equation (2.11) is a non-linear problem which is solved iteratively. The computation time for each iteration is comparable to that of the 3D RP method, and the number of iterations depends on noise in the projection data. Several algorithms have been developed in order to limit the number of iterations required to reach convergence. The problems of slow convergence and image noise can be overcome by adding priors and replacing the log-likelihood criterion by a penalized-likelihood objective function where a measure of the image roughness (the penalty function) can be adjusted (with Bayes weights). Regularization can also be accomplished

by filtering at different stages on the reconstruction. However, these modifications can introduce non-uniformities in the spatial resolution and the noise variance in the reconstructed PET image (Ollinger and Fessler, 1997).

2.1.2 Image Characteristics

PET images are noisy and offer poor tissue delineation compared to detailed anatomical images. For a given signal, improvement in the image variance is usually achieved with a concomitant degradation of the spatial resolution.

2.1.2.1 Signal-to-Noise Ratio

The noise in the projections is independent and Poisson distributed since it originates from counting radioactive sources. After reconstruction, the noise in the PET images is correlated via the point spread function. The noise equivalent count rate (NEC) attempts to relate the image signal-to-noise ratio (SNR) to the scatter S, random R and true T coincidence rates (Strother, 1990) via

$$NEC = \frac{T}{(1 + SF^2) \left(1 + \frac{S}{T} + 2 \frac{R}{T} \right)} \quad (2.12)$$

where SF is the scatter fraction $SF = S/(S + T)$, ignoring the deadtime and attenuation corrections. Setting $S = R = 0$ in equation (2.12) shows that the NEC can be interpreted as the reduced true coincidence rate which, without random and scatter coincidence events, would produce the same SNR as the true coincidence rate obtained after subtracting random and scatter coincidence rates from the total coincidence rate (Strother et al, 1990).

The spatial noise distribution in the PET images is also influenced by the attenuation and emission distributions and by the reconstruction method. When the PET images are reconstructed with 3D reprojection algorithm, the noise distribution is uniform for a homogeneous or heterogeneous radioactivity distribution and homogeneously

attenuating media like in the brain. The image variance can then be considered to be similar throughout the image, and mostly dependent on the count rate. This approximation no longer holds in the presence of heterogeneously attenuating media like in the chest, where the noise distribution becomes non-uniform (Pajevic, 1998). By definition, the image variance is strongly dependent on the radioactivity distribution when the PET images are reconstructed using an iterative reconstruction algorithm.

2.2 Compartmental Modeling

Image reconstruction in conjunction with the appropriate corrections to the measured projection data yields quantitative measures of a PET radiotracer's spatial radioactivity distribution within the body. This distribution is time varying and depends on a number of factors such as tracer delivery, binding to cell surface receptors, diffusion or transport into cells, metabolism, washout from the tissue and excretion from the body. Dynamic sequences of PET measurements enable radiotracer concentration to be measured as a function of time. With an understanding of the biologic fate of the radiotracer in the body, it is possible to construct mathematical models with a set of one or more parameters that can be fit to explain the observed time activity curves. This analysis process is called tracer kinetic or compartmental modeling

2.2.1 Concepts of Compartmental Modeling

Biologic systems can be represented or modeled as a collection of compartments, sometimes referred to as pools or spaces, linked by kinetic processes that provide a mechanism of exchange of tracer between adjoining compartments. A compartmental model is a model consisting of a finite number of compartments with specified interconnections among them. A compartment is an amount of material that acts as though it is well-mixed and kinetically homogenous. It may represent a distinct physical space or chemical form or pharmacologic state of the radiotracer that occupy the same physical space.

Various compartments of a kinetic model are linked by a set of parameters called rate constants (k). It is a proportionality constant and links the amount of tracer exiting a compartment to the amount of tracer in the compartment. First order rate constants have the units of inverse time. Second order rate constants have units of inverse concentration and inverse time, etc. The concentration of the enzyme is so high in relationship to the tracer concentration that the kinetic equation is sometimes a pseudo first order, for example the reaction of [^{11}C]deprenyl with the enzyme MAO B. The inverse sum of all first order rate constants is called the turnover time of the compartment.

In the standard representation of compartmental systems, a box is used to represent a compartment and an arrow for the transfer of material into or out of that compartment. The amount or concentration of radiotracer in the model compartments can be described as a function of time by a set of first-order differential equations in terms of the model parameters. Mathematically, the exchange of material between compartments is expressed as a system of mass-balance equations in which the rate of change in the amount of material in each compartment is equal to the difference between the amount of material entering and exiting that compartment.

2.2.1.1 Theory of Linear Compartmental Systems with Constant Transfer Coefficients

A typical PET data set contains the time course of radioactivity concentration, or time-activity curve (TAC), in plasma and in various tissues, measured after the injection of a radiotracer. The tissue TACs constitute the measured output of a system probed by an exogenous input, the plasma TAC. The purpose of making these measurements is to quantify the characteristic response of the physiological system given these input and output data.

Using mass balance differential equations, the description of a general n -compartment model is:

$$\frac{dm_i(t)}{dt} = -k_{0i}m_i(t) - \sum_{j \neq i} k_{ji}m_i(t) + \sum_{j \neq i} k_{ij}m_j(t) + u_i(t) \quad (2.13)$$

where $m_i(t)$ and $m_j(t)$ are the amount of material in compartments j and i respectively, and k_{ji} is the rate constant for the transfer of material from compartment i to

compartment j . The term $u_i(t)$ is the rate at which material enters compartment i from the outside whereas $-k_{0i}m_i(t)$ is the rate at which material leaves compartment i to the outside. If the rate constants k 's are independent of the time interval (stationary assumption) and the conjugate m 's (linearity assumption), equation (2.13) becomes a first-order linear differential equation with constant coefficients. In matrix form; equation (2.13) can then be rewritten as

$$\dot{m} = Km(t) + u(t) \quad (2.14)$$

where K is called the compartmental matrix and $k_{ii} = -k_{0i} - \sum_{j \neq i} k_{ji}$.

If $u(t) = 0$: the solution to the system of n homogeneous differential equations is the sum of the n linearly independent exponential functions $m(t) = v \exp(\lambda t)$, of equation (2.14):

$$m(t) = \sum_{i=1}^n c_i v_i \exp(\lambda_i t) \quad (2.15)$$

where n is the number of compartments. The λ 's are the system eigen values which are the non trivial solutions to the characteristic polynomial $(K - \lambda I)v = 0$, where I is the identity matrix. The v s are the corresponding system eigenvectors and each is found by solving the equation $Kv_i = \lambda_i v_i$. The constants c_i 's are determined by the initial conditions. When the initial conditions are set to $m_i(0) = 1$ and $m_{j \neq i} = 0$ for $j = 1, 2, \dots, n$, equation (2.15) represents the characteristic impulse response of the system.

Most often in PET, the compartments are not measured individually, but instead only the sum of the compartments of the system is available. From the theory of linear differential equations, the solution of compartmental model equations when the k_{ij} are all constant and the input into the system is a single bolus injection in an arbitrary compartment is a sum of exponentials.

$$m_t(t) = c_1 \left(\sum_{i=1}^n v_{i1} \right) \exp(\lambda_1 t) + c_2 \left(\sum_{i=1}^n v_{i2} \right) \exp(\lambda_2 t) + \dots + c_n \left(\sum_{i=1}^n v_{in} \right) \exp(\lambda_n t) \quad (2.16)$$

$$= \sum_{i=1}^n A_i \exp(\lambda_i t),$$

where the macro parameters A_i and λ_i are a combination of the microparameters k_{ji} . The number of microparameters must be less than or equal to the number of macroparameters ($2n = nA\text{'s} + n\lambda\text{'s}$) in order to uniquely identify the microparameters (Cobelli and DiStefano, 1980). Otherwise, either certain k 's must be set to zero or some estimation strategy (like including a priori information or performing additional independent measurements) must be adopted in order to reduce the number of microparameters to be determined (Cobelli and DiStefano, 1980; Landaw and DiStefano, 1984). Identifiability of all microparameters does not however guarantee a unique solution (Cobelli and DiStefano, 1980).

2.2.2 Input Function

If the tracer is introduced in the system of interest as an impulse-bolus, the measured tracer activity as a function of time will be a sum of exponential components. This sum of exponentials is usually called the impulse response function of the system. The number of exponential components in the response function is equal to the number of compartments in the model.

When the input function is not an impulse, the measured tracer quantities will be the convolution of the input function with the response function of the system. The radiotracer for PET studies is injected into the blood stream such that the time course of radioactivity concentration in arterial plasma represents a time varying input function, $u_i(t)$, to the system.

$$y(t) = \int_0^t u_i(\tau) q_i(t - \tau) d\tau = u_i(t) \otimes \sum_{i=1}^n A_i \exp(\lambda_i t) \quad (2.17)$$

The convolution is a direct result of the linearity of the compartmental models. Not many physiological processes are linear, but because the amount of tracer introduced

is always very small as compared to the natural substance, the transport or chemical transfer of tracer usually can be considered as linear. Measurement of the input function allows it to be deconvolved from the tissue tracer curve to yield the impulse response of the tissue. This impulse response reflects kinetic process in the tissue without interference from effects in the rest of the body.

The input function is typically measured by sampling blood from the radial artery, fairly rapidly initially and at longer time intervals as the PET study continues. The blood data acquired in this way are inevitably distorted by delay and dispersion between the points of radiotracer assay and delivery to tissue (Meyer, 1989). For radiotracers with kinetics slower than blood flow, these effects can be accounted for by the inclusion of a delay (A_t) and a blood volume (V_b) term in the equation of the compartmental model:

$$y(t) = u_i(t + \Delta t) \otimes q_t(t) + V_b \times u_i(t + \Delta t) \quad (2.18)$$

When the blood and tissue data are acquired with different devices, these must be cross calibrated such that the units of the input function and the tissue TAC are the same. This can be achieved by preparing a phantom and an aliquot from the same solution and measuring their respective radioactivity concentration in the PET camera and in the radiation detector used to measure the blood concentration. Alternatively, each device can be calibrated against a third device that has previously been calibrated with a standard radioactive source.

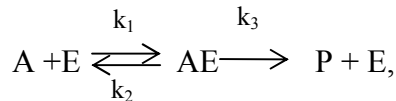
Additional measurements are required when the radiotracer is compartmentalized in the erythrocytes and/or metabolized in peripheral tissue. The effect of the former is to reduce the availability of the radiotracer to cross the blood-brain barrier. The effect of the latter is to transfer the radiolabel to molecules other than the injected radiotracer. The partition of radioactivity between plasma and erythrocytes can be corrected for by measuring the radioactivity concentration in both plasma and whole blood. The contribution of the metabolites to the total plasma radioactivity can be separated from that of the unmetabolized parent using analytical chemistry procedures, most commonly high pressure liquid chromatography (HPLC) analysis. Unlike whole blood which can be sampled continuously and counted on-line, the measurements for the determination of

blood partition and peripheral metabolism can only be performed at a few discrete times. Interpolation and extrapolation of these corrections over the duration of the PET study is therefore necessary.

2.2.3 Enzyme Kinetics

Enzymes are proteins that catalyze biochemical reactions. They are specific to both the binding substrates and the catalyzing reactions. In general, enzymes take the name of their substrate, followed by a word ending in -ase that specifies the type of reaction. The catalytic activities of many enzymes are regulated in two ways: The enzyme availability is determined by both its rate of synthesis and its rate of degradation, and the enzyme activity is controlled by alteration in the binding-substrate affinity. The binding affinities of substrates and inhibitors to an enzyme; the maximum catalytic reaction rate of an enzyme, and ultimately the amount of enzyme present can be inferred from the study of enzyme kinetics (Voet and Voet, 1995).

Most chemical reactions in living tissue are enzyme catalyzed reactions. Generally, they can be represented as



where A denotes the substrate which is being converted to the product P through the catalytic action of enzyme E. The k's are the rate constants for the reaction steps. The reaction could involve only a single substrate or multiple substrates. In the latter case, the concentrations of all substances not shown are assumed to be constant. By assuming the enzyme concentration to be constant, the rate of reaction from A to P can be shown to be related to the concentration of A as

$$\begin{aligned} R &= \frac{k_3 C_0 [A]}{(k_2 + k_3) / k_1 + [A]} \\ &= \frac{V_m [A]}{K_m + [A]}, \end{aligned} \tag{2.19}$$

where C_0 is the total enzyme concentration. This equation is known as Michaelis-Menton equation and variable V_m and K_m that characterize the equation are called Michaelis-Menton constants. V_m is maximum velocity of the reaction because it is the fastest rate possible for a given enzyme concentration. K_m is called half saturation concentration and is equal to the concentration of A that would produce half the maximal rate. (Voet and Voet, 1995)

Now, suppose a tracer A' is similar to A in its reaction with the enzyme E, i.e.



If the association and dissociation rates of the substrate-enzyme complex are much faster than the rate of variation in the concentration of A' , the conversion fluxes from A and A' to P and P' are

$$\begin{aligned} R &= \frac{V_m [A] / K_m}{[A] / K_m + [A'] / K'_m + 1} \\ R' &= \frac{V'_m [A'] / K'_m}{[A] / K_m + [A'] / K'_m + 1} \end{aligned} \quad (2.20)$$

where V'_m and K'_m are Michaelis-Menton constants of the enzymatic reaction for the tracer A' . If A' satisfies the tracer requirement that its concentration is much smaller than that of A (i.e. $[A'] \ll [A]$), then the above equations can be written as

$$\begin{aligned} R &= \frac{V_m [A]}{[A] + K_m} \\ R' &= \frac{V'_m K_m / K'_m [A']}{[A] + K_m} \end{aligned} \quad (2.21)$$

dividing R'/R ,

$$\frac{R'}{R} = \frac{V'_m K_m [A']}{V_m K'_m [A]}$$

The equation for the natural substrate is the same as the one without the tracer added, because the tracer A' has low concentration and is assumed to have a negligible effect of steady state condition of the reaction. This equation is similar to the natural substrate except that it is linear with respect to the concentration of the tracer. This is a critical relationship as far as tracer kinetic modeling is concerned. It is the fundamental basis for modeling enzyme catalyzed reactions with linear models.

2.2.4 Compartmental Models

General models for description of tracer distribution are described below. C_p represents the plasma concentration of labeled tracer. C_F is the free concentration of the tracer in tissue C_{NS} . K_1 and k_2 are the ligand transport constants, plasma to tissue and tissue to plasma respectively. Units of K_1 are $(\text{ml tissue}) (\text{ml plasma})^{-1} \text{min}^{-1}$ so that the product $K_1 C_p(t)$ gives the rate of influx of the radiotracer to the first compartment, the input function.

K_1 and k_2 are functions of blood flow and the permeability surface area

A one-compartment two rate constant is shown in figure 2.2. This model is typically used for reference tissue, i.e. tissue in which no specific binding or metabolism of the tracer occurs.

$$\frac{dC_{NS}}{dt} = -k_2 C_{NS}(t) + K_1 C_p(t) \quad (2.22)$$

Integration yields

$$C_{NS}(t) = C_{NS}(0) \exp(-k_2 t)$$

Solving for initial condition $C_{NS}(0)=1$

$$C_{NS}(t) = \exp(-k_2 t)$$

Convolving with the input function yields

$$y(t) = \exp(-k_2 t) \otimes K_1 C_p(t) \quad (2.23)$$

A two-compartment four rate constant model is shown in figure 2.3. This model adds a specifically bound tracer, C_s .

Figure 2.4 demonstrates a case where the binding is irreversible on the time scale of the experiment. This is a commonly used model for receptor binding, and the differential equations are given by equations 2.24 and 2.25.

$$\frac{dC_1^{NS}}{dt} = K_1 Cp(t) - k_2 C_1^{NS} - k_{on} f_{NS} (B_{\max} - L - N_B) + k_4 C_2^S \quad (2.24)$$

$$\frac{dC_2^S}{dt} = k_{on} (B_{\max} - L - N_B) + k_4 C_2^S \quad (2.25)$$

The assumption implicit in the model of specific binding is that the receptor occupancy is unchanged during the course of the experiment. k_3 is given by $k_3 = f_{NS} k_{on} (B_{\max} - N_b - L)$ where B_{\max} is the total receptor/transporter concentration, N_B is the endogenous neurotransmitter concentration. L is the concentration of unlabeled ligand bound to receptors.

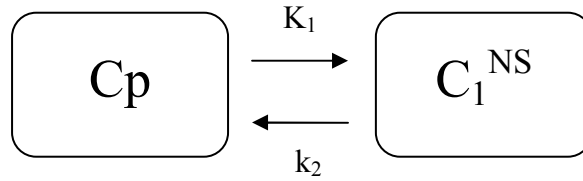


Figure 2.2: One compartmental model

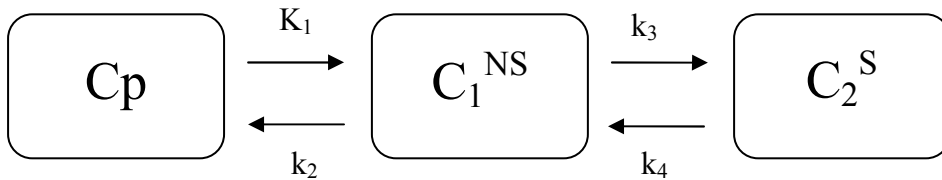


Figure 2.3: Two compartmental model, Reversible

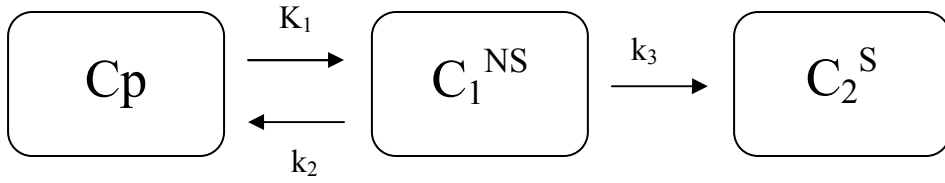


Figure 2.4: Two compartmental model, Irreversible

2.2.5 Parameter Estimates

The application of compartmental modeling can be divided into three separate steps (Jacquez, 1988).

- 1) Developing plausible models which should be based on background knowledge of the system under study and the chosen structures should lead to a physiological interpretation of the model parameters.
- 2) Formulating and solving the equations that predict the behavior of the system. These first two steps constitute the forward problem and are treated in the previous sections.
- 3) Finding the parameter estimates and the plausible model that best describe the collected data. This is an inverse step and is addressed in this section

2.2.5.1 Non-Linear Least-Squares Analysis

Let us assume that the only source of deviation between the measurements $\mathbf{z}(t)$ and the model predictions $\mathbf{y}(t, \mathbf{p})$ is random measurement errors $\mathbf{e}(t)$:

$$\mathbf{z}(t) = \mathbf{y}(t, \mathbf{p}) + \mathbf{e}(t) \quad (2.26)$$

Let us further assume that $\mathbf{e}_i(t)$ are independent and Gaussian distributed with zero mean and variances σ_i^2 . The least-squares method then tries to find an estimate of $\mathbf{p}(\hat{\mathbf{p}})$ that minimizes the weighted residual sum of squares (WRSS) between the N measurements $\mathbf{z}(t)$ and model predictions $\mathbf{y}(t)$:

$$WRSS(\hat{p}) = \sum_{i=1}^N w_i [z(t_i) - y(t_i, \hat{p})]^2 \quad (2.27)$$

where the weights are set to $w_i = 1/\sigma_i^2$. Data points having the smallest associated errors are given the greatest relative importance in the least-squares estimation procedure. Equation (2.27) has a unique minimum when the model $y(t_i, \mathbf{p})$ is linear in all its parameters \mathbf{p} . However, equation (2.16) is linear in the parameters A_i but non-linear in the parameters λ_i . Multiple minima can thus exist, and an iterative search of the parameter space does not guarantee finding the absolute minimum. Furthermore, starting values for \mathbf{p} are required which influence both the number of iterations and the minimum (local or absolute) found. It is recommended to guide the search procedure by imposing boundary conditions on the values of \mathbf{p} , in particular that the values of k_{ji} must be non-negative or those of λ_i non-positive (Landaw and DiStefano, 1984).

Precision on the Parameter Estimates

The standard error (SE) on the estimate \hat{p}_i can be calculated by taking the square root of the i^{th} diagonal element of the covariance matrix COV (Landaw and DiStefano, 1984) which is defined as

$$COV(t, \hat{p}) = (J^T W^{-1} J)^{-1} \hat{\sigma}^2 \quad (2.28)$$

where \mathbf{J} is the Jacobian matrix with elements $j_{ij} = \partial y(t_i, \mathbf{p}) / \partial p_j$ for $i = 1, 2, \dots, N$ data points and $j = 1, 2, \dots, P$ parameters, and \mathbf{W} is the diagonal matrix with elements w_i . When σ^2 is unknown, the unbiased estimate $\hat{\sigma}^2 = WWRSS(\hat{p}) / (N - P)$ can be used. The i, j^{th} element of the covariance matrix corresponds to the covariance between the two parameters \hat{p}_i and \hat{p}_j . The correlation coefficient, which takes values between -1 and 1, can also be derived from the covariance matrix by dividing the i, j^{th} element by the product $SE(\hat{p}_i)SE(\hat{p}_j)$.

Strong correlations between parameters and poor precision on parameter estimates are signs that the covariance matrix is ill-conditioned (Landaw and DiStefano,

1984). This problem can result from a poor experimental design. The data sampling must be long and frequent enough to capture the full dynamic range of the model. Otherwise, two exponential terms that are close but distinct will not be distinguished. Ill-conditioning of the covariance matrix can also be caused by over-parametrization, i.e. fitting the measurements to a model of order $n + 1$ when the system should really be modeled with n compartments. The least squares method then attempts to separate two exponential terms that have indistinguishable λ 's and for which only the sum of the corresponding A 's can be estimated precisely. Confirmation of this diagnosis can be obtained with statistical tests.

Discrimination amongst compartmental models

Models of increasing order can sequentially be compared by performing an F-test under the null hypothesis that the model of order $n+1$ does not give a better fit to the measurements than the model of order n (Landaw and DiStefano, 1984):

$$F = \frac{(WRSS_n - WRSS_{n+1}) / (P_{n+1} - P_n)}{WRSS_{n+1} / (N - P_{n+1})} \quad (2.29)$$

The F distribution has $(P_{n+1} - P_n, N - P_{n+1})$ degrees of freedom where again P_i is the number of parameters in model i and N is the number of data points. When the probability of obtaining a larger F value is no longer significant, the lower-order model is accepted as the best model in a statistical sense. It is then usually symptomatic to find, in the higher-order model, one value of A_i that cannot be distinguished from zero within its SE.

2.2.5.2 Measures of receptor availability

Composite parameters such as binding potential (BP) (Mintun et al. 1984), the total tissue distribution volume (DV), the distribution volume ratio (DVR) (the ratio of the DV of a receptor region to that of a reference region without the receptor), an effective binding potential derived from the DVR or a difference between the receptor

DV (DV_{ROI}) and the DV of the reference region (DV_{REF}) are sometimes used instead of individual model parameters. The binding potential is defined as

$$BP = \frac{B_{\max}}{K_d} \quad (2.29)$$

The distribution volume is given by the ratio of the tissue to plasma under equilibrium conditions, i.e. $DV = C_{ROI}/C_p$, C_{ROI} is the tissue concentration of a region of interest. Alternatively for on equilibrium experimental conditions, the DV given by as

$$DV = \frac{\int_0^{\infty} C_{ROI}(t)dt}{\int_0^{\infty} C_p(t)dt} \quad (2.30)$$

DV can also be defined by graphical analysis or equilibrium measurement.

The DVR is given by (assuming that the ratio of transport constants is the same for both receptor and reference region)

$$\begin{aligned} DVR &= \frac{DV_{ROI}}{DV_{REF}} \\ &= 1 + \frac{k_3}{k_4} \\ &= 1 + \frac{B_{\max}}{K_d} \end{aligned} \quad (2.31)$$

Binding potential can then be calculated as $DVR-1$.

2.2.5.3 Solving Models with measured plasma input function

A. Reversible Compartmental Models

For one and two compartmental models the linear equations are

$$C_{ROI}(t_i) = K_1 \int_0^{t_i} Cp dt - k_2 \int_0^{t_i} C_{ROI}(t) dt \quad (2.32)$$

$$C_{ROI}(t_i) = K_1(k_3 + k_4) \int_0^{t_i} \int_0^{t'} Cp dt dt' - \kappa \int_0^{t_i} C_{ROI}(t) dt - k_2 k_4 \int_0^{t_i} \int_0^{t'} C_{ROI}(t) dt dt' + K_1 \int_0^{t_i} Cp dt$$

Where $k=k_2+k_3+k_4$

To overcome the bias in equation 2.32, Feng et al,(1993) introduced a generalized linear least squares (GLSS) method.

$$C_1(t_i) - \hat{k}_2 e^{-\hat{k}_2 t_i} \otimes C_1(t_i) = K_1 e^{-\hat{k}_2 t_i} \otimes Cp(t_i) - k_2 e^{-\hat{k}_2 t_i} \otimes C_1(t_i) \quad (2.33)$$

Graphical Analysis

Graphical analysis transforms a set of linear equations describing a model into a single equation which becomes linear for time $t > t^*$ (Logan et al. 1990). Two parameters are determined, the slope and the intercept which are combinations of the model parameters. The graphical analysis equation for points determined by scan times t_i is

$$\frac{\int_0^{t_i} C_{ROI}(t) dt}{C_{ROI}(t_i)} = [DV + V_p] \frac{\int_0^{t_i} Cp(t) dt}{C_{ROI}(t_i)} + \text{int} \quad (2.34)$$

where $DV+V_p$ is the slope for the linear region which occurs for times $t_i > t^*$ and V_p is the contribution of the tissue blood volume. The condition for linearity of the above is that the intercept (int) which for a two tissue compartment model is given by equation below is constant.

$$-\frac{1}{k_2} \left[1 + \frac{k_3}{k_4} \right] - \frac{C_2(t)}{k_4(C_1(t) + C_2(t))}$$

B. Irreversible compartmental models

Irreversibly binding ligands are essentially trapped for the time course of the scanning procedure. Information about receptor availability is contained in model parameter k_3 . The three model parameters can be estimated using an optimization procedure and solving the differential equations directly.

A model independent graphical method (Patlak 1983; Patlak, 1985) evaluates the rate constant (K_i) for the transfer of tracer from plasma to the irreversible compartment. The equation for this is

$$\frac{C_{ROI}(T)}{Cp(T)} = K_i \frac{\int_0^T Cp(t)dt}{Cp(T)} + (Ve + Vp) \quad (2.35)$$

which is linear for the times $T > t^*$ when Ve , the distribution volume of the reversible part (the ratio of the concentration in the reversible compartment to plasma) is constant. Relating this to the two tissue compartment irreversible model, the influx K_i can be expressed as

$$K_i = \frac{K_1 k_3}{k_2 + k_3} = \frac{K_1 \lambda k_3}{K_1 + \lambda k_3} \quad (2.36)$$

K_i is expressed in terms of two parameters, K_1 which represents the transport of ligand from plasma to tissue and the combination parameter λk_3 which also contains the ratio of transport constants ($\lambda = K_1/k_2$). Although K_1 and k_2 are functions of blood flow, λ is not.

2.2.5.4 Solving Models without measured plasma input function

The complications associated with blood sampling and analyses have led to the development of reference tissue approaches which use a reference tissue as an indirect input, function to the target tissue.

A. Reversible Compartmental Models

Determining important kinetic parameters without a plasma input function requires a reference region, a region devoid of the receptor/transporter or other binding

site. Lammertsma et al. (1996) presented a reference region method assuming the reference region could be described by a one tissue compartment model.

$$C_T(t) = R_1 C_{REF}(t) + [k_2 - R_1 k_2 / (1 + BP)] C_{REF}(t) \otimes \exp(-k_2 t / (1 + BP)) \quad (2.37)$$

where C_{REF} and C_t are the concentration in the reference region and total tissue concentration. R_1 is the ratio K_1 / K_1^{REF} . k_2 , R_1 and BP are determined using non-linear analysis. Gunn et al revised this equation so that R_1 and β are determined by linear least square optimization for a set of values of γ

$$C_T(t) = R_1 C_{REF}(t) + \beta C_{REF}(t) \otimes \exp(-\gamma t) \quad (2.38)$$

Graphical analysis method is modified such that DVR can be calculated using data from a reference region ($C_{REF}(t)$) with an average efflux constant, \bar{k}_2 to approximate plasma integral.

$$\frac{\int_0^T C_{ROI}(t) dt}{C_{ROI}(T)} = DVR \left[\frac{\int_0^T C_{REF}(t) dt + C_{REF}(T) / \bar{k}_2^{REF}}{C_{ROI}(T)} \right] + int \quad (2.39)$$

where int' is $int + \delta$, δ is the error term given by

$$\delta = DVR \left(\frac{1}{k_2^{REF}} - \frac{1}{k_2} \right) \frac{C_{REF}(T)}{C_{ROI}(T)}$$

B. Irreversible Compartmental Models

Patlak and Blasberg (1985) extended the graphical analysis for irreversible ligands to an analysis using a reference region in place of the plasma input. It is assumed that the reference region has no specific binding so that in the steady state condition $C_{REF}(t) = C_p(t)$ for $t > t^*$

$$\frac{C_{ROI}(t_i)}{C_{REF}(t_i)} = K' \frac{\int_0^{t_i} C_{REF}(t) dt}{C_{REF}(t_i)} + b \quad (2.40)$$

When this is true so that a plot of $\frac{C_{ROI}(t_i)}{C_{REF}(t_i)}$ vs $\frac{\int_0^{t_i} C_{REF}(t)dt}{C_{REF}(t_i)}$ is a straight line for $t_i > t^*$ with slope $K' = Ki/(DV_{REF} + V_p')$ where V_p' is the blood volume of the reference region and DV_{REF} is the DV of the reference region.

2.3 PET Radiotracer Mechanisms and Models

Tracer kinetic modeling is used to describe the response of a system and to estimate the physiologic and biochemical parameters from the observations. In this section three different tracers (used in the course of the thesis for experiments and modeling) will be explained. The assumptions for compartmental modeling, biochemical data and implementation of the model will be discussed.

2.3.1 ^{18}F -flourodeoxyglucose (FDG)

The most frequently used tracer for measuring glucose utilization with PET is ^{18}F -flourodeoxyglucose (FDG). The chemical structure of FDG is identical to glucose, except that hydroxyl group in the second carbon is replaced by a fluoride atom. This alteration of natural glucose results in FDG only tracing the glycolytic pathway through transport and phosphorylation to the end product of FDG-6-PO₄. FDG-6-PO₄ does not leave the cell except slow hydrolysis back to free FDG, which can be transported to plasma or rephosphorylated. Figure 2.5 illustrates the transport and reaction pathways of FDG as compared to glucose in cerebral tissue.

A compartmental configuration for FDG model is shown in figure 2.6. The three-compartment model consists of FDG in plasma, FDG in tissue and FDG-6-PO₄ in tissue corresponding to comparable concentration of glucose, although glucose continues on to metabolism. The first order rate constants k_1^* and k_2^* describe the transport of FDG from blood to brain and brain to blood, respectively. k_3^* and k_4^* describe the phosphorylation of FDG and dephosphorylation of FDG-6-PO₄. The asterisk * refers to FDG indices and corresponding term for glucose do not have asterisk.

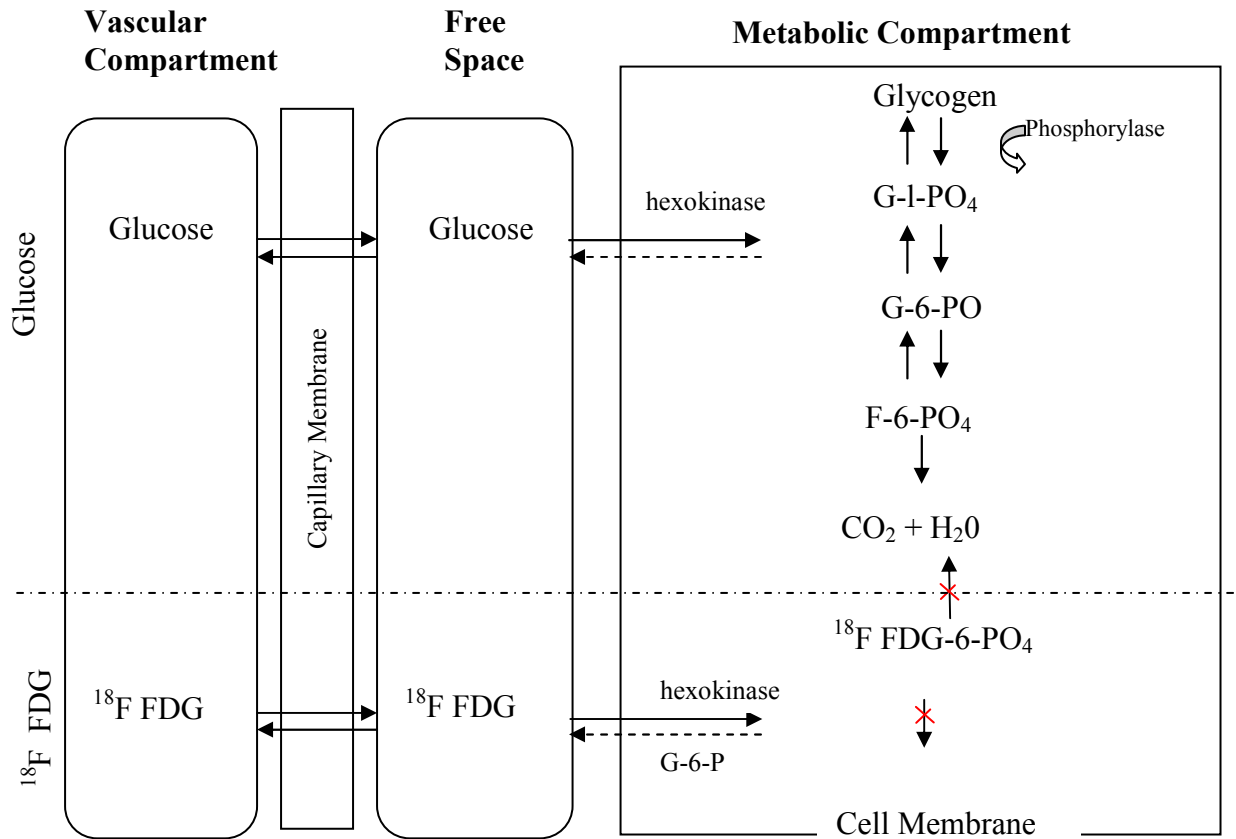


Figure 2.5: The transport and reaction pathways of FDG as compared to glucose in cerebral tissue.

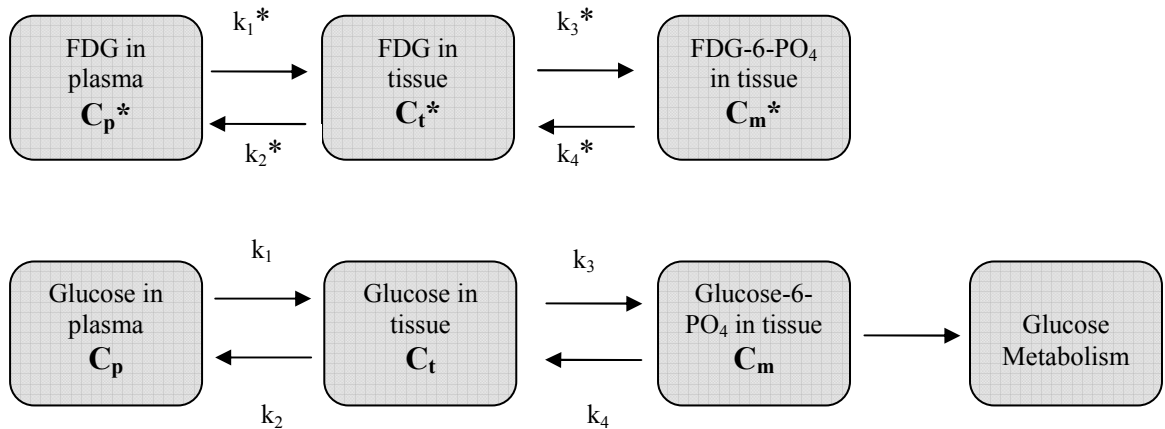


Figure 2.6 Three-compartment FDG model with four first order rate constants.

Let MRGLc^* ($\mu\text{mol}/\text{min}/\text{g}$) refer to metabolic rate of FDG and MRGLc ($\mu\text{mol}/\text{min}/\text{g}$) be the metabolic rate of glucose. From equation 2.22 and from the fact that the rate of phosphorylation equals $k_3 C_t$ for glucose and $k_3^* C_t^*$ for FDG,

$$\begin{aligned}\frac{\text{MRGLc}^*}{\text{MRGLc}} &= \frac{V_m^* K_m C_t^*}{V_m K_m^* C_t} \\ &= \frac{k_3^* C_t^*}{k_3 C_t}\end{aligned}\quad (2.41)$$

Equation 2.41 assumes that k_4 and k_4^* are very small and the forward rate of phosphorylation of glucose and FDG approximate the net metabolic rate

If the ratio of equation 2.41 is a constant

$$\text{MRGLc} = \text{MRGLc}^* / \text{constant} \quad (2.42)$$

Multiplying equation 2.41 by C_p/C_p^* ,

$$\frac{\text{MRGLc}^*/C_p^*}{\text{MRGLc}/C_p} = \frac{V_m^* K_m C_t^* / C_p^*}{V_m K_m^* C_t / C_p} \quad (2.43)$$

The ratio C_t^*/C_p^* and C_t/C_p are defined as partition coefficients for FDG (λ^*) and glucose (λ). Further dividing left hand side of equation 2.43 by blood flow F ,

$$\frac{\text{MRGLc}^*/(C_p^* \times F)}{\text{MRGLc}/(C_p \times F)} = \frac{V_m^* K_m \lambda^*}{V_m K_m^* \lambda} \quad (2.44)$$

This ratio is defined as Lumped constant, LC , for the FDG model. The left side of equation 2.44 is the net extraction of FDG (E_{net}^*) divided by the net extraction of glucose (E_{net}).

$$LC = \frac{E_{net}^*}{E_{net}} \quad (2.45)$$

MRGLc is given by (Phelps et al, 1986)

$$MRGLc = \frac{C_p}{LC} \left(\frac{k_1^* k_3^*}{k_2^* + k_3^*} \right) \quad (2.46)$$

Hence, a measurement of cold glucose level in plasma, an assumed value of lumped constant and estimates of k_1^* , k_2^* and k_3^* from a dynamic sequence of PET scans, provide metabolic rate of glucose.

An approximation of MRGLc can be derived from a set of data acquired at a relatively late time postinjection due to kinetics of deoxyglucose and FDG. The rate of phosphorylation is reasonably high while the rate of dephosphorylation is very low, trapping the radiotracer once phosphorylated. The fraction of the radiotracer trapped inside a pool increases throughout the study and the clearance from the tissue is relatively rapid, hence a single “late” static scan closely reflects the relative metabolic rate of glucose. By assuming population average values for the individual rate constants for FDG and given a value for cold glucose concentration in plasma, a population average MRGLc can be calculated as

$$MRGLc_{pop} = \frac{C_p}{LC} \left(\frac{k_{1pop}^* k_{3pop}^*}{k_{2pop}^* + k_{3pop}^*} \right) \quad (2.47)$$

MRGLc_{ind} is then calculated as

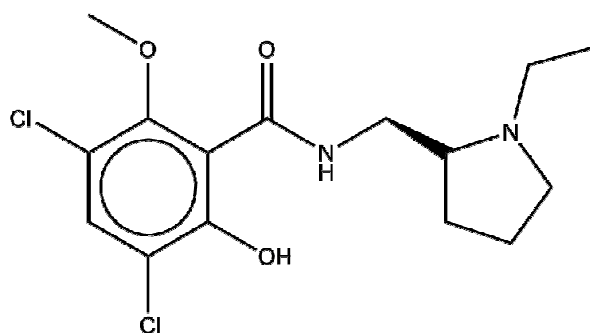
$$MRGLc_{ind} = MRGLc_{pop} \times \left(\frac{C_{tot_{ind}} - C_{f_{pop}}}{C_{m_{pop}}} \right) \quad (2.48)$$

where $C_{m_{pop}}$ is the FDG average concentration in the phosphorylated compartment and $C_{f_{pop}}$ is the free concentration based on the population averages, $C_{tot_{ind}}$ is the measured PET value of the individual.

2.3.2 [¹¹C] Raclopride

[¹¹C]Raclopride is used as a PET research tool to determine dopamine type 2 (D2) receptor density under normal and pathological conditions. Raclopride (figure 2.7), a

compound of the salicylamide series, is an antipsychotic drug with high selectivity and affinity for central D₂-dopamine receptors. It is retained in tissue as a result of binding to a neurotransmitter receptor.



¹¹C Raclopride Chemical Structure

Described below are the dopamine metabolism, pathway and importance of studying the dopaminergic system using PET radiotracers.

The Brain Dopaminergic System

Dopamine Metabolism and Pathways

Two types of cells are found in brain tissues (McGeer et al; 1987): Nerve cells (or neurons), which carry the electrical nerve impulse, are interleaved with supporting glial cells, broadly divided into oligodendroglia, astroglia and microglia. Neurons are composed of a cell body (or soma) from which extend a single long stem (or axon) and multiple branches (or dendrites). The electrical nerve impulse is propagated between neurons via the transmission of specific chemical messengers (called neurotransmitters) across the small cleft separating two nerve terminals, together forming a junction (called synapse). In the brain, the transport of substances from capillary blood to tissue is tightly regulated. Unlike elsewhere in the body, the capillary endothelial cells overlap and are enclosed by sealed astroglial cells together creating a diffusion barrier, the blood-brain barrier (BBB). Furthermore, specific active transport systems allow penetration of critical substances, amongst others glucose and essential amino acids, against concentration gradients.

Dopamine (DA) is a catecholamine neurotransmitter present in the brain in concentrations of nmol/g of tissue (McGeer et al, 1987). It is synthesized in situ from the

successive action of tyrosine hydroxylase (TH) on the endogenous amino acid L-tyrosine (pT) followed by aromatic L-amino acid decarboxylase (AADC) on L-3,4-dihydroxyphenylalanine (L-DOPA). DA is packaged into pre-synaptic vesicles by the vesicular monoamine transporter (VMAT) where it is protected from further metabolism by monoamine oxidase (MAO). Upon stimulation, DA is released into the synaptic cleft. From there DA can either bind to post-synaptic dopamine receptors (eliciting an excitatory or inhibitory metabotropic action on the D1 like or D2-like receptors, respectively), be transformed by the combined actions of catechol-O-methyl transferase (COMT) and MAO into several metabolites (3-methoxy-tyramine (3MTA), 3,4-dihydroxy-phenylacetic acid (DOPAC) and homovanillic acid (HVA)) which diffuse away from the synapse, or be recaptured at the pre-synaptic reuptake site, the dopamine transporter (DAT). The synthesis of dopamine is regulated at the tyrosine hydroxylation step. Newly synthesized dopamine is preferentially released and metabolized over stored dopamine. The turnover time of dopamine in the striatum has been estimated to be of the order of 1.5 to 4 hours (McGeer et al; 1987). There are three major dopaminergic pathways in the brain (Volkow et al, 1996; McGeer et al, 1987): The nigrostriatal pathway originates from cell bodies located in the substantia nigra (in the brainstem) which project predominantly to the striatum (in the basal ganglia); cells bodies in the ventral tegmental area (in the brainstem) projecting to regions in the limbic system (hippocampus, amygdala, nucleus accumbens, cingulate gyrus and frontal cortex) form the mesolimbic-mesocortical pathway; the tuberoinfundibular pathway plays a role in coupling the hypothalamus (in the diencephalon) to the pituitary gland (outside the BBB), thereby contributing to the stimulation and inhibition of various hormones. Disruption of dopamine function in the nigrostriatal pathway, which is involved in the initiation and execution of movements, leads to neurological disorders such as Parkinson's disease (PD). The mesolimbic mesocortical pathway is associated with mood, reinforcement and thought organization, and is implicated in psychiatric illnesses such as schizophrenia and substance abuse. The number of dopamine neurons declines with age (McGeer et al, 1977). Dopamine function can be selectively altered, whether reversibly or irreversibly, at different levels using various pharmacological agents. Dopamine function can also be probed with PET in combination with a variety of radiotracers labeling dopamine

precursors, degrading enzymes, transporters or receptors, and pharmacological or behavioral challenges (Volkow et al, 1996).

Raclopride is a selective dopamine antagonist with a high affinity for dopamine type 2 (D_2) receptors. Since the neurotransmitter dopamine may be involved in various neuropsychiatric diseases, the in vivo binding of raclopride to dopamine receptors in the striatum can be measured by PET with radiolabeled raclopride used as a tracer. [^{11}C]raclopride has a long time been one of the most widely used PET tracers, and even worked as a model tracer in development and validation of new analysis methods.

Lammertsma et al. (1996) compared one- and two-tissue compartment models, and found that two tissue compartments were required to achieve decent fit, also in cerebellum, but BP estimates from two-tissue compartment model had too high standard errors. BP was calculated from DV values of striatum and cerebellum, calculated from K_1-k_4 (2 Compartmental model) or K_1-k_2 (1 Compartmental Model) estimates. MTGA for reversible tracers (Logan plot) with metabolite corrected plasma input has been shown to provide reproducible DV and DVR maps (Wang, 1999). The cerebellum is nearly devoid of D_2 and D_3 receptors, and specific binding of RP is thought to be negligible in the cerebellum. Therefore, cerebellum is commonly used as reference tissue in [^{11}C]raclopride PET studies. Multiple time graphic analysis (MTGA) for reversible tracers (Logan plot) can be applied to [^{11}C]raclopride PET data with cerebellum curve instead of metabolite corrected plasma input to produce DVR estimates ($\text{BP}=\text{DVR}-1$).

2.3.3 [^{11}C] Clorgyline

[^{11}C]clorgyline is a ^{11}C -labeled PET tracers have been used for imaging MAO A. Clorgyline (figure 2.8) antagonizes MAO-A, an enzyme that catabolizes dopamine. [^{11}C]-Clorgyline has been monitored in the human brain and body by PET. It is an irreversible inactivator of MAO A (Johnston, 1968)

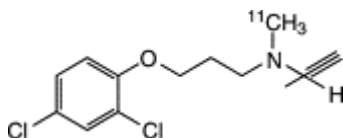


Figure 2.8 Chemical Structure of [^{11}C]clorgyline

Monoamine oxidase (MAO) is an integral protein of outer mitochondrial membranes and occurs in neuronal and non-neuronal cells in the brain and in peripheral organs. It oxidizes amines from both endogenous and exogenous sources thereby influencing the concentration of neurotransmitter amines as well as many xenobiotics (Singer, 1995; Richards, 1998). It occurs as two subtypes, MAO A and MAO B which have different inhibitor and substrate specificities. MAO A preferentially oxidizes norepinephrine and serotonin and is selectively inhibited by clorgyline (Johnston, 1968) while MAO B preferentially breaks down the trace amine phenylethylamine and is selectively inhibited by L-deprenyl (Knoll, 1972). Both forms oxidize dopamine, tyramine and octopamine. Oxidation is accompanied stoichiometrically by the reduction of oxygen to hydrogen peroxide. The relative ratios of MAO A and B are organ and species specific (Saura, 1994).

Because the regional and cellular compartmentalization of MAO and its subtypes determines to a large extent the access of specific substrates to each subtype, a knowledge of the distribution of MAO A and B in the brain and the peripheral organs is a crucial element in understanding neurotransmitter regulation and in understanding the MAO inhibitory properties of drugs (Fowler, 1996).

For kinetic analysis in studies employing [^{11}C]clorgyline, a three-compartment model is used to estimate $k(3)$, the model term proportional to MAO A activity. Setting the k_4 term (rate of dissociation from specifically bound compartment) to zero accounts for the irreversible trapping of radiotracer during metabolic oxidation. The k_3 term is related not only to specific binding to the protein but also to the catalytic bond-breaking process. The most robust model parameter was found to be the product λk_3 . This phenomenon has been investigated further and found to be related to the larger permeability term (K_1/k_2) in smokers (Logan, 2005)

Chapter 3

Wrist Scanner: Characterization and Feasibility Studies

3.1 Overview:

Aim: A Non-Invasive Wrist Scanner was developed as an alternative to invasive arterial sampling to measure the input function of radiotracer uptake in PET studies. It consists of 2 pairs of 4 x 8 LSO crystal arrays, in one to one configuration with 4 x 8 APD arrays. This prototype was used for preliminary experiments for basic characterization. This chapter covers the proof of concept and feasibility studies for non invasive estimation of an input function from the wrist arteries.

Method: Preliminary experiments included estimating sensitivity, spatial and image resolution, scatter and count rate performance for the 4 detector scanner. An anatomically correct wrist phantom was used for these studies. Focal plane imaging technique was used to reconstruct planar images. Finally, the scanner was used in a real clinical setting to quantify counts detected in the human wrist.

Result: The efficiency of the scanner was ~ 4 cps/nCi/cc. This sensitivity appeared to be low for the estimation of an input function, as the human studies demonstrated. However, the results show that the detector was able to discriminate the arterial and venous flows from each other using planar coincidence images in both phantom and human studies. Measurements of count rate made with a realistic source of radioactivity outside the field of view quantified the randoms that would be detected from the nearby radioactive arm and body. Lead shielding between the scanner and the body significantly reduced the number of randoms. A comparison with arterial blood samples and wrist scanner time activity curve showed that the shape of the two curves matched closely. Scans carried out in a realistic clinical setting demonstrated that the positioning of the detectors with respect to each other and the arteries can be a problem that will need to be taken into consideration for the next prototype.

Conclusion: The wrist scanner will enable noninvasive measurement of the input function, thereby eliminating invasive blood sampling. However, its design architecture will have to be reevaluated for its translation into a clinical setting.

3.2 Introduction

3.2.1 Problem Definition

The level of radioactivity in a particular tissue at any given time is dependent on amount of radioactivity in the blood being delivered to the tissue as a function of time (the input function) and on the change in the concentration of the radiotracer in the tissue as a function of time (the tissue response function) (Wahl, 2002). A kinetic model can be used to relate the changes in the radiotracer concentration to some physiological process. The parameters of this model can often be correlated with changes in the physiological process brought about by disease or drug action or behavioral intervention. An input function is typically measured by acquiring discrete arterial blood samples, usually from a radial artery. These samples are spun down to separate the plasma from the red blood cells. A measured aliquot of the plasma is used to estimate the concentration of radioactivity. This procedure, although considered as the ‘gold standard’ for determining the plasma input function, has limitations, which in turn limit full quantification of the PET study. These limitations include:

- The discomfort to the subject associated with the placement of the arterial catheter and withdrawal of blood.
- The potential radioactive contamination of medical personnel.
- The possible transmission of blood borne diseases.
- The apparent dispersion caused by drawing blood out with a peristaltic pump.

The placement of the arterial catheter is also very difficult in a clinical setting and is usually not performed. Therefore the clinical results are limited to just using the image as the diagnostic tool without trying to quantify the process.

This chapter illustrates the design, construction and characterization of a novel wrist scanner that is proposed for quantitative and non-invasive measurement of the arterial radioactivity concentration. Image derived techniques will be employed for extraction of the input function from planar wrist images obtained using the tomograph. As is shown in the following sections, this scanner has several advantages over direct invasive blood withdrawal techniques, some of which include the reduction of pain for the patient, the reduction of risks associated with blood borne pathogens and radiation exposure to medical personnel and the elimination of the distortion in the input function which results from blood removal by mechanical means.

3.2.2 Specific Aims

There are three specific aims for the project which are given below:

1. To measure the sensitivity, spatial and image resolution and characterize the count rate performance of the scanner.
2. To use a Lucite phantom representing the human wrist in order to evaluate the effects of other background sources of radiation (surrounding the wrist artery) that may obscure the input function from the wrist arteries, using figures of merit such as SNR and contrast ratios.
3. To validate the use of the wrist scanner for non-invasive and selective measurement of arterial radioactivity in a research setting for human subjects.

3.2.3 Literature Review

The ultimate solution to the problem of arterial sampling may be a small PET scanner which specifically images any artery in the body for appropriate blood radioactivity detection. There have been several attempts for building PET scanners to separately image the neck or the wrist, for extracting an input function, to complement the larger PET scanner that does a broader scan of the brain (Aykac, 2001). A wrist

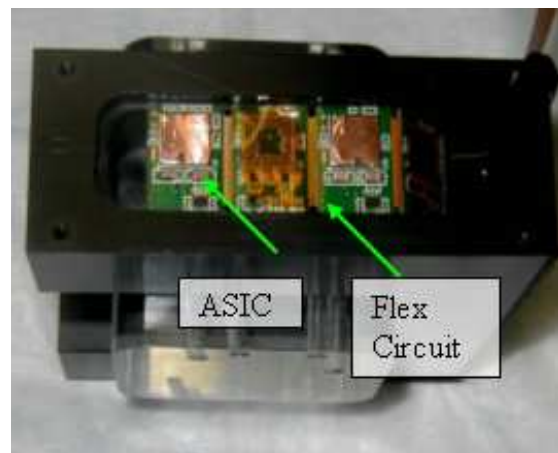
tomograph would be ideal since it is more portable and practical than a neck scanner and it can be placed further away from the total body radioactivity occurring during a clinical study which will reduce randoms. Eriksson et al (1991) tried the first measurement of the wrist with a regular PET tomograph to see if it can be feasible to measure an arterial input function. However, they got an underestimation of the input function as compared to the invasively sampled input function. This inaccuracy is due to the problems of partial volume effects and poor recovery coefficients. Thus better spatial resolution tomographs need to be designed so that they could have a field of view smaller than that of the regular PET scanner. Rajeswaran et al. (1992) used an array of bismuth germanate (BGO) crystals and photomultiplier tubes as their radial monitor, but they did not get a good measurement of the input function due to limited spatial resolution of the detector. For the wrist PET scanner being developed as a part of this thesis, better photon collection crystals (made of Lutetium Oxyorthosilicate, LSO) are being used along with a small Avalanche Photodiodes (APD) array that matches the size and pixels of the crystal block, as compared to Rajeshwaran's detector. These technical advancements (LSO+APD) dramatically reduce the size of the scanner. When compared to BGO, LSO scintillation crystals have desirable properties such as high light output and fast decay time, for an application such as a dedicated wrist scanner (see Chapter 2, Section 2.1). Instead of scanning the heart, neck, or brain with a large PET tomograph, the radial and ulnar artery of the wrist will be the area being scanned with a small dual detector pairs. The wrist scanner will have four unique properties in comparison to the PET tomograph.

- 1) Essentially, it will be an independent PET scanner in that it also collects gamma radiation from blood flowing through the wrist. (It may be shielded from outside radiation to reduce random coincidences occurring as a result of the radioactivity in the body.)
- 2) The device will be portable and easy to transfer to a clinical setting.
- 3) This tomograph will be placed on the same location of the wrist as the invasive technique to give a good agreement between blood sampling techniques and also since dispersion plays a factor in the temporal profile of the blood concentration.
- 4) Lastly, the wrist detector will face the least amount of tissue attenuation, since the wrist has reasonably sized arteries and less tissue for the photons to pass through as

compared to other body parts (such as the neck, chest or brain) thereby giving less photon scatter and a higher signal to noise ratio (SNR).

3.3 Prototype Scanner

The Wrist Scanner consists of 4 detector blocks. Each detector block consists of a 4 x 8 array of $2.22 \times 2.22 \times 15 \text{ mm}^3$ LSO crystals that are optically attached and read out with a matching array of APDs. The LSO crystal arrays for the Wrist Scanner were manufactured by Proteus [Proteus Inc., Chagrin Falls, OH] and APDs were Hamamatsu's S8550. The individual LSO crystals are separated by a 0.078 mm air gap from each other. There is a layer of 3M foil between every crystal. These are not glued to the surface of the crystal, but are placed in the air gap. The purpose of using the mask was to let photons that otherwise would escape the crystal reflect back into the crystal which would increase the light collection efficiency. The complete LSO matrix is placed within a glass frame that consists of 4 glass plates of 0.5 mm thickness. Figure 3.1 shows the details of the Wrist Scanner system



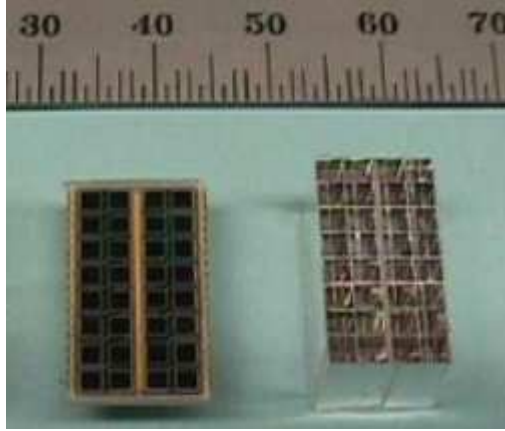


Figure 3.1 Top Left: Wrist Scanner prototype with LSO crystals Top Right: Prototype wrist scanner with flex circuit visible at the top. Bottom: 4 x8 LSO and APD arrays

3.3.1 Light collection efficiency

The light collection efficiency is determined in part by the intrinsic crystal properties as discussed in the introductory chapter. The best energy resolution occurs when there are a large number of photons collected for each event and this number has a low variability. Simulations and experiments were carried out for determining the light output from the LSO and APD arrays

Light Output Simulations

The experimental results were compared to the simulation studies of scintillation light collection. OptiCAD [OptiCAD, Optical Analysis Program User's guide version 6.0] has been used to simulate the process of the scintillation light collection in one pixel of a LSO+APD detector. It is a Monte Carlo simulation software and is structured in a computer-aided design (CAD) format. This enables the user to place objects of complex geometry and surface properties into a global or local coordinate system. For the emission of scintillation photons with random distribution and orientation within the LSO crystal, additional code that described volumetric sources had to be imported into the simulation package.

OptiCAD is a commercially available ray tracing program that can be used to study a variety of optical systems by modeling the propagation of light rays through volumes of material after taking into account their interaction at various surfaces in terms of reflectivity, transmission and scatter. OptiCAD was used to estimate the light collection efficiency in these LSO crystals by generating light rays inside the crystal and propagating these rays to the photodetector. The absorption coefficient of the 511 keV photons can be determined from the attenuation length of LSO. This gives an attenuation coefficient of $0.086 \text{ [mm}^{-1}\text{]}$.

The simulation code was carried out with the following components:

- 1- An object that represents the $2.22 \times 2.22 \times 15 \text{ mm}$ LSO scintillation crystal.
- 2- A volumetric light source.
- 3- An object that represents a layer of silicone cookie between the APD and the LSO crystal.
- 4- An object that represents the APD ($1.6 \text{ mm} \times 1.6 \text{ mm}$ active surface).
- 5- A film that is attached to the APD window. This film detects the number of photons that can reach the APD.

Light was generated isotropically within thin slabs in 1 mm steps along the length of the crystal to estimate the effect of the longitudinal light collection efficiency. Each ray is initially generated with unit energy and is propagated until it is either absorbed by the photodetector or the ray tracing is terminated. At each refractive surface, the ray is split into a primary and secondary descendant (or ghost) according to its energy. The energy split is based on the refractive indices of the materials at the interface and is a measure of the probability of how the light ray is further propagated. OptiCAD has several parameters that are used to terminate the propagation of the light ray, which include:

- a) exceeding a maximum number of ray–surface intersections, (maxdepth)
- b) exceeding a maximum number of ghosts, (maxghost)
- c) falling below a minimum ray energy for transmission (mintrans)

These parameters were tuned in the OptiCAD simulation to give the best agreement with the measured experimental data, and the resulting values were maxdepth = 20, maxghost = 2 and mintrans = .01 (Kriplani, 2005).

The light collection efficiency was determined by the ratio of the energy detected at photodetector to the total initial energy (or number of rays) generated. The number of photoelectrons detected is related to the number of scintillation photons produced by the following formula:

$$N_{pe}/MeV = N_{gamma}/MeV \times \text{efficiency} \times QE$$

An intrinsic light output of 25,000 scintillation photons per MeV was assumed for the LSO crystals, and the known quantum efficiency of 24% at the peak wavelength of the LSO (420 nm) emission for the phototube was used in these measurements. LSO-Surface properties such as reflectance and absorbance were the main parameters that need to be well modeled and modified in the simulation in order to mimic all the LSO configurations as discussed above.

The simulation results showed that the placement of a Silicone plate (cookie) to transmit the light from the crystal to the APD increased the light collection efficiency. Further improvement in the light collection efficiency (almost by a factor of 2) was achieved by the 3M Radiant Mirror Film (RMF) wrapping. Simulation results showed that ~4600 photoelectrons/MeV were obtained for a 15mm crystal.

Experimental Light output

The light output of the LSO arrays was measured by coupling these arrays to the APD array through a thin silicone layer or air gap. All measurements were made with the same APD. The gain of each channel of the APD was measured using a pulsed nitrogen laser (wavelength = 337 nm) to illuminate the individual pixels through an optical fiber. The light intensity of the laser was adjusted such that the charge output of the APD could be measured directly using an ADC, and it was therefore not necessary to

use a preamp on the APD output. The integrated charge output was then measured as a function of the applied bias voltage to the APD

A Ge-68 flood source was used to experimentally determine the light output. It was placed in front of the detectors and exposed them to a uniform illumination. For each photon interaction with the crystal arrays, the collected scintillation photons that reached the APD were converted into electric charge. The APD signals were amplified with charge sensitive preamplifiers, integrated over 90 ns time intervals and digitized with LeCroy 4300B FERA ADC's. The photoelectrons/MeV and the energy resolutions were measured and averaged over all the 32 channels of the detector block. The width of the photopeak measured across its points of half-maximum amplitude is the energy resolution. This is referred to as the full width half maximum (FWHM) and is usually expressed as a percentage of the photopeak. This measurement was repeated for the four crystal arrays used for the prototype and the photoelectrons/MeV and energy resolutions were averaged over their samples.

$$\text{pe/MeV} = [\text{photpk-ped (ch)}] / [0.511 \text{ (MeV } \gamma) * 0.815 \text{ (ch/pe)}]$$

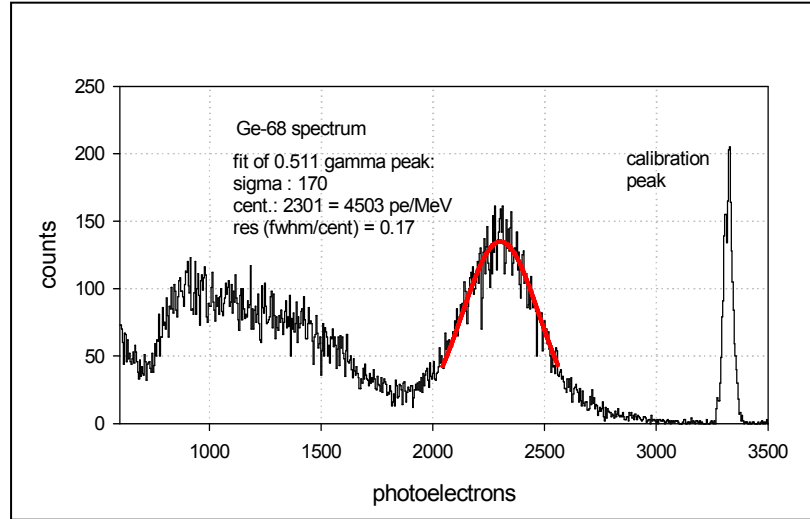


Figure 3.2 Typical Ge-68 spectrum for an LSO array / APD channel.

In general there was a good agreement between the simulation and experimental results (Kriplani, 2005). The experimental light output measured was 4800

photoelectrons/MeV. The standard deviation of light collection distribution from array to array was 11 %. Figure 3.2 shows a typical pulse height spectrum measured with a crystal array and the APD with the Ge-68 flood source. The 511 keV peak corresponds to ~ 2400 photoelectrons, or ~ 4800 p.e./MeV.

3.3.2 Electronics and readout system

Front End Electronics

The wrist scanner consists of 128 channel camera with a communication and power management module, an absolute time and address generator module, and a versa module eurocard (VME)-based acquisition system. The main design objectives for the front-end electronics as applicable to the wrist scanner, is that the electronics must be optimized on the LSO-APD characteristics, especially its timing properties (charge integration time), and that the amplifier needs to be matched with the scintillation detector timing properties. The detectors have a light output of 4800 photoelectrons/MeV. The prototype has 4 detector blocks and each has a front-end ASIC mounted on the back. The main purpose of the chip is to provide the position and the timing information of every detected event. On the back of each detector block, there is a 1.8V voltage regulator and circuitry for independent high voltage trimming of each APD array.

Figure 3.3 presents a block scheme of the ASIC used for this thesis. The prototype is composed of 32 channels of Charge Sensitive Preamplifier (CSP), bipolar semi-Gaussian shaping filter and Zero-Cross Discriminator used to find the timing information of every event. All zero-cross discriminators are interconnected to a 32 channel serial encoder used to multiplex the timing information and the 5-bit address of each channel into a single output in order to minimize the number of interconnection between the ASIC and the DAQ. When an annihilation photon is detected in the LSO/APD detector, the CSP integrates the charges delivered by the APD, to convert them into a useful voltage signal. This signal is then filtered through the shaper to limit the noise bandwidth. The output signal from the filter has a bipolar shape and is optimized to keep the electronic noise contribution to the degradation of the energy resolution negligible. The

zero-crossing of this bipolar signal is then found by the timing discriminator, triggering a logic timing edge which is asynchronous with the 100MHz ASIC clock. Finally, the encoder serializes this timing edge with the 5 bit channel address, decoded by the DAQ.

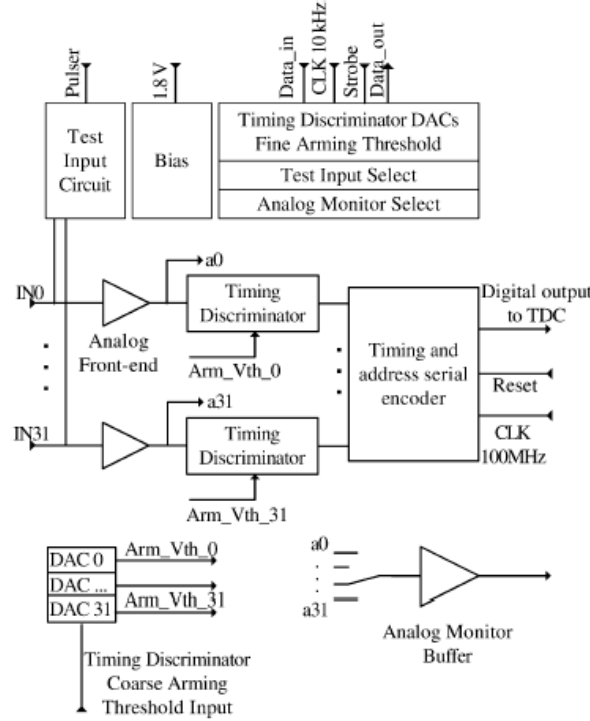


Figure 3.3: Diagram of the analog front end of the ASIC (courtesy of J.F. Pratte)

Data acquisition system

On the receiving side of the DAQ is a Field Programmable Gate Array (FPGA) based Time to Digital Converter (TDC). The timing signal edge is digitized by the TDC utilizing a high frequency clock (~ 1.3 ns timing resolution) which is achieved using the FPGA to split the TDC clock cycle into multiple branches with incremental delays between them (Junnarkar, 2005), thereby giving us the ability to assign a time stamp to each detected photon. For each event, the TDC output is a 64 bit word with: 43 bits for the time stamp, 5 bits for crystal identification (among 32 crystals from each block), 8 bits for block detector identification, 5 bits allocated as event counter (3 bits determine the event type among 8 different possibilities).

The principle of the data acquisition is illustrated in figure 3.4. The time and address information are attached to single events and coincidence processing is done offline. In order to find photons in coincidence, the time stamps of events are used to calculate the time interval between two detected single events. If this time interval lies within the coincidence time window, the two single events will result in a coincidence event. From the preliminary tests, the coincidence time window of the system is ~ 20 ns.

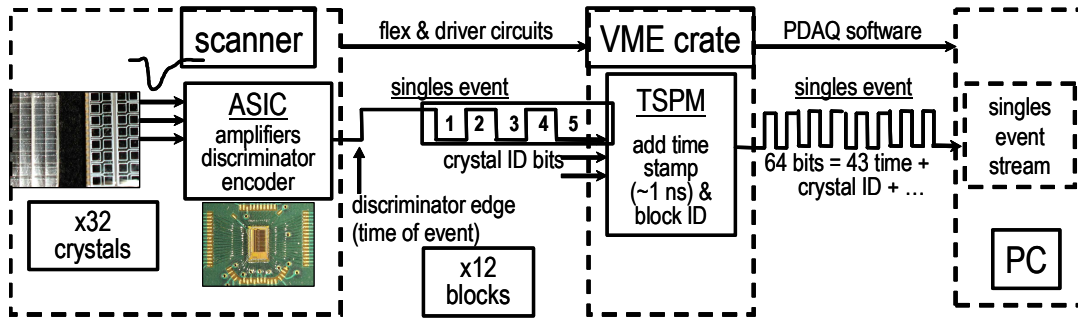


Figure 3.4a Detector Module Signals are carried on the Flex circuit to a data processing module.

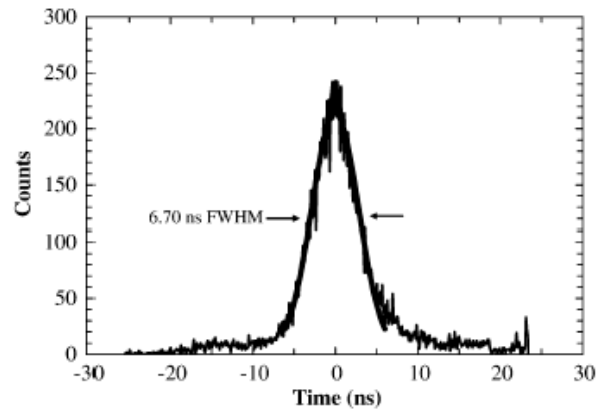


Fig. 3.4b. Coincidence timing resolution of the analog front-end using the CFD as a ZCD with APD/LSO detector. A timing resolution of 6.70 ns FWHM was measured.

The chip has been evaluated using input from the APD. It has a linear range between 50-600keV (at an APD gain of 50) with an impulse response gain of 20mV/fC. The maximum and minimum input charge expected from the LSO-APD modules for a true event are from 8fC to 25fC respectively. The response is linear over this entire range. Figure 3.4b shows the coincidence timing resolution of the ASIC connected to the

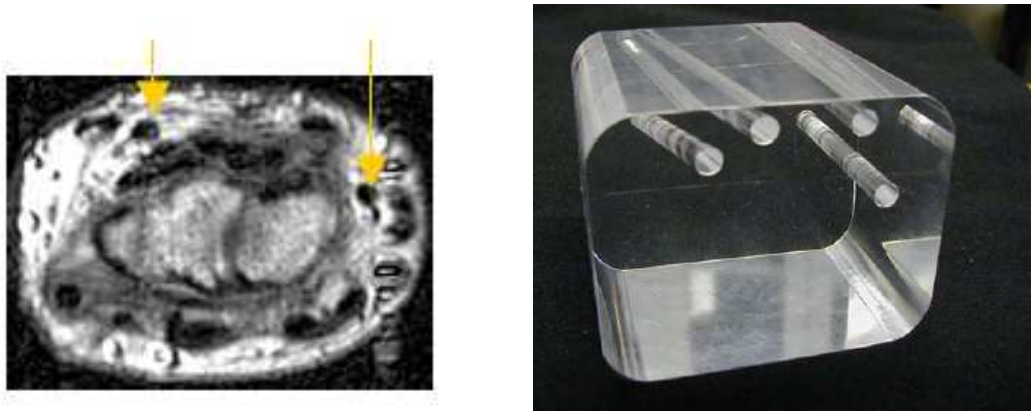
APD/LSO detector. A timing resolution of 6.76 ns FWHM was measured in coincidence with a PMT coupled to a BaF₂ scintillator. A coincidence timing resolution of 10 ns was measured for an energy threshold of 250 keV.

3.4 Preliminary experiments

Preliminary work for the Wrist Scanner involved basic characterization of the prototype in an effort to evaluate parameters that will play a crucial role in quantification of radioactivity detection from the wrist arteries. These include sensitivity, resolution and count rate performance. To perform feasibility measurements of image resolution and background effects, a wrist phantom was used. Image formation involved the development and optimization of the focal plane imaging technique for this dual detector scanner. A detailed report follows:

3.4.1 Wrist Phantom

MRI images of the wrist were acquired to estimate the location and size of the wrist arteries. A wrist phantom was constructed by estimating the radial, ulnar and two arbitrary vein paths as seen in figure 3.5. The veins were placed on top to simulate the venous return and its background noise effects on the arterial function. The wrist phantom design was fabricated using a Lucite block. The phantom's final construction can be seen in figure 3.5



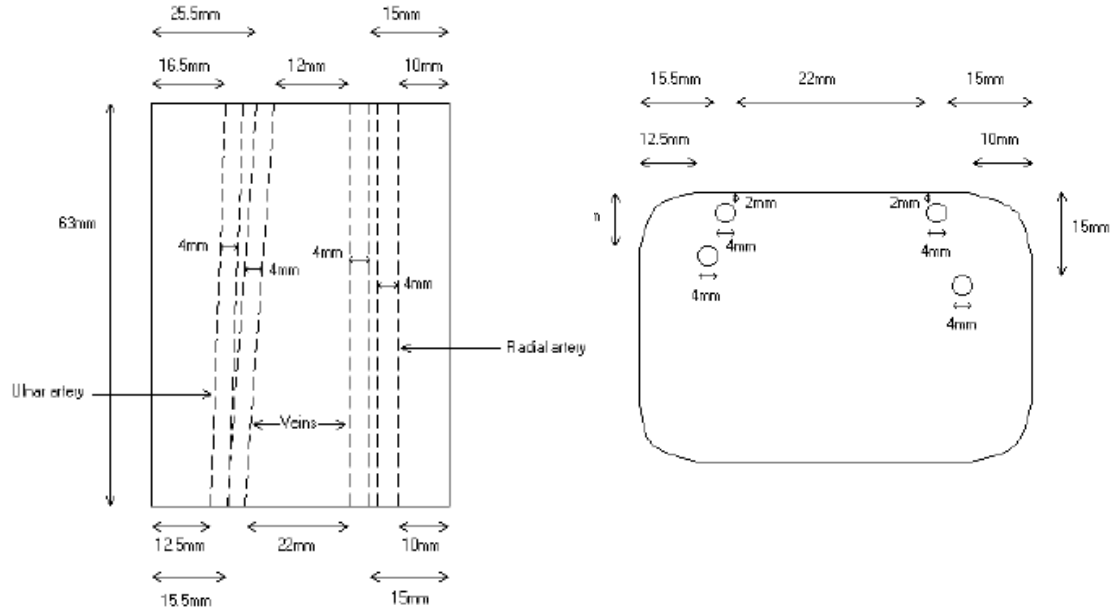


Figure 3.5: Top left: MRI scan of the wrist. Top Right: Finished design of the wrist phantom representing the left hand. Bottom: Dimensional illustration of the phantom

In figure 3.5, the ulnar is the bottom hole on the left and the radial is on the right. It also shows the artery holes leaning more towards the anterior side of the wrist or top edge of the phantom. Therefore, this phantom could give a more realistic approximation of the number of scattered events.

3.4.2 Detection Efficiency

The sensitivity of PET is determined primarily by the absorption efficiency of the detector system and its solid angle of coverage of the imaged object. The true coincidence rate, R_{true} for a positron emission source located in an absorbing medium between a pair of coincidence detectors is given by,

$$R_{\text{true}} = E \epsilon^2 g_{\text{ACDE}} e^{-\mu T} \quad (3.1)$$

Where E is the source emission rate, ϵ is the intrinsic efficiency of each detector; μ and T are linear attenuation coefficient and total thickness of the object respectively. g_{ACD} is the

geometric efficiency of the detector pair. Each component as applicable to the current wrist scanner is illustrated below.

3.4.2.1 Components of Detection Efficiency

A. Geometric efficiency

a. Solid angle

The distance between the two detector pairs is 5.2 cm. The wrist is assumed to be 4.8 cm and the total distance between the wrist and blocks is 2mm on each side. It was seen from the MRI scan of the wrist that the ulnar artery was at a depth of 1.9 cm from the top (3.3 cm from the bottom). This was chosen as the point that contains activity within the central axis (figure 3.6). All the events detected by a circle of radius 1.9 cm will be detected and hence the bigger circle of radius 3.3 cm was used by solid angle component measurement.

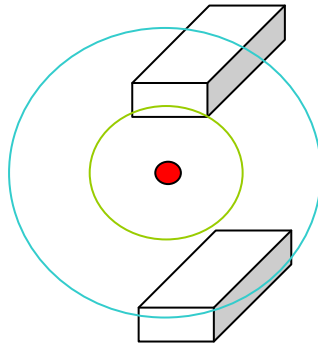


Figure: 3.6 Solid angle cover range of diameter 1.9 and 3.3 cm

A solid angle was drawn from this point and calculated as a ratio of the width of the detector over the circle's circumference

$$= 0.8 / [2 \times \pi \times 3.3]$$

$$= 0.0386$$

The total solid angle component for detection efficiency of both detectors is 0.0772

b. Vertical counting efficiency

For the case of planar detectors of the wrist scanner, the events seen in the field of view (FOV) of the detectors would be the only ones counted. Hence a vertical efficiency component is essential for determining the total efficiency of the scanner.

Figure 3.7 shows the estimated analysis for vertical efficiency in the case of the wrist. The object of interest is located at a depth of 1.9 cm from the detector placed on the top of the wrist. Hence, there will be two different FOVs for each height step as illustrated by the figure (created by a large (3.3 cm) and small (1.9cm) gap).

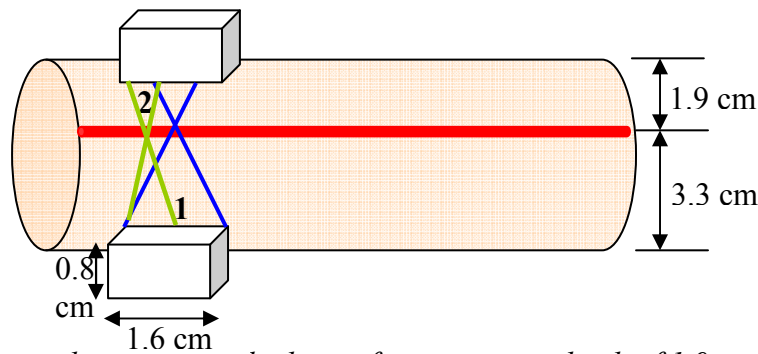


Figure 3.7: Vertical efficiency calculation for artery at a depth of 1.9 cm

When compared to an ideal case, where the activity is in the center plane, the proximity of activity to the top detector reduces the top FOV region. Thus it gives a loss in the counting efficiency on the top region. The larger FOV plot would be an overestimation of the bottom detector efficiency. Therefore, the smaller FOV plot takes precedence for estimating the vertical counting efficiency over the whole range. The area of the 'FOV 2' trapezoid is 1.14 cm^2 and the area of the ideal FOV for a central plane would be $1.6 \times 1.6 \text{ cm}^2$. Hence the ratio of the 'FOV 2' plot and the ideal FOV gives:

$$\text{Vertical counting efficiency} = (1.14 \text{ cm}^2) / (2.56 \text{ cm}^2) = 0.44$$

B. Intrinsic Efficiency of the detector

The sensitivity of a PET system depends critically on the detection efficiency of the detector, which enters as a squared term in equation.

The fraction of radiation striking the detector that interacts with it is called the intrinsic efficiency ε of the detector.

The factors that contribute towards ε are:

- a. Probability of an LSO interaction
- b. Electronic triggering probability loss due to low light collection efficiency

The first component of ε is the probability for a photon to have an LSO interaction (ε_{sc}). A gamma photon with enough energy could pass unhindered through the crystal if the length is small. As the area of the crystal increases, the fraction of gamma photons that interact and convert to light photons will also increase. The second component is the probability of a photon that would cause an electronic triggering, which is a combination of light collection (ε_{col}) being converted to an electronic signal (ε_{e-h}) and afterwards being counted within the timing coincidence window. If the energy were to be spread to several crystals as in the cross talk problem, then the light energy would be too low to be collected and converted to an electronic signal (Vaska, 2003). The biggest factor between the two in reducing efficiency is the light collection. The light can be spread, not reflected well enough or be absorbed by non-reflective material present at the gateway of the APD. The conversion of light and the rest of the electronics are efficient (~98%) in producing a count per keV photoelectron. The other factor that would lower the electronic efficiency would be the APD, amplifier and discriminator noise (δ noise), which may garble the signal in any of the three steps (accounts for the other 2%).

In addition, there is an efficiency of 0.6 for the probability for a 511 keV photon to interact in the 15 mm LSO crystals

$$\varepsilon = 1 - e^{-\mu_1 x} \quad (3.2)$$

μ_1 is the linear attenuation coefficient of LSO crystal (0.88 cm⁻¹ for 511 keV) and x is the detector thickness, which is 15mm gives an $\varepsilon = 0.73$

The electronic discrimination efficiency (determined by the hardware threshold) was calculated to be ~ 0.4 . This efficiency is based on the trigger threshold used in the readout electronics (150 keV) and the estimate of edge effects and the effect of inter-crystal scatter in the crystal arrays on the trigger efficiency. This gives a combined efficiency of 0.30.

C. Absorption and Scatter of Radiation

Absorption generally causes a decrease in the recorded counting rate, while scatter can lead to a decrease or an increase, depending on whether there is more scattering away from or toward the detector. Some of the photons can change direction out of the FOV due to Compton scatter and attenuation. The photons can interact with the atoms of the material medium and produce Compton scatter as described in chapter 2: PET Physics. For the calculation of the attenuation loss, the material properties are taken into consideration in calculating the percent photons being attenuated. The equation that approximates the attenuation loss in any medium is:

$$N = N_0 \exp(-\mu \delta x) \quad (3.3)$$

where N_0 is the total number of photons, N is the amount of photons left after attenuation, μ is the linear attenuation coefficient and δx is the distance traveled by the photons through the medium. The attenuation coefficient can then be used in equation 4.1 to calculate the percent attenuated. In this case, two distances were in question, which were 1.8 cm and 3.2 cm. The attenuation for the tissue, μ at 511keV is 0.095 cm^{-1} . Therefore, using the exponential piece of the equation; one would get attenuation coefficients of:

$$\exp(-0.095 * 3.3) = 0.73$$

$$\exp(-0.095 * 1.9) = 0.83$$

For the combined attenuation of both detectors, it would then be: $0.73 * 0.83 = 0.61$.

The total sensitivity of this detector would theoretically be:

$$37 \text{ dps/nCi} * (0.0772 * 0.44 * (0.73 * 0.4)^2) \text{ cps/dps} = 0.11 \text{ cps/nCi}$$

Hence, for a set of two detector pairs, the efficiency is 0.22 cps/nCi. The detector has a field of view of 0.05 cc, hence the sensitivity of the scanner is 4.4 cps/nCi/cc.

With attenuation, this sensitivity number would then be: $0.11 * 0.61 = 2.684 \text{ cps/nCi/cc}$

3.4.2.2 Experimental estimation of the detector system sensitivity

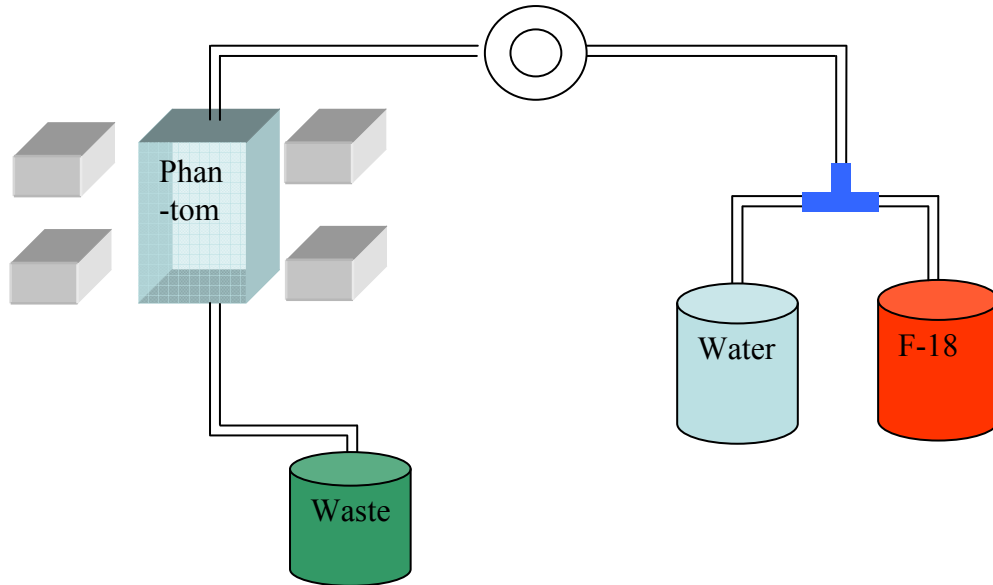


Figure 3.8: Experimental setup for efficiency measurement.

An experiment was conducted to measure sensitivity and to simulate the rapid rise and fall of the activity in a typical input function. This efficiency measurement was carried out by placing $2\mu\text{Ci/cc}$ of fluorine-18 in an aqueous solution in the tubing inside the phantom. The flow through the phantom was switched between plain water and the solution containing the radioactivity, 'F-18' solution. The experimental set up is shown in figure 3.8. The flow of fluid would start first from the reservoir of water, then switched to the F-18 solution and lastly switched back to reservoir of water all in a one-pulse form. The activity was left to decay to collect enough data for a proper exponential fit. The block labeled hot was the vial that contained radioactivity, and the block labeled cold was the vial containing water. The flow rate for all three experiments was $\sim 7.2 \text{ mL/min}$. The inner diameter of the tube was 2mm. The transit time between the switch valve and the detector was $\sim 24 \text{ sec}$. The efficiency, obtained as a ratio of dividing the

wrist monitor measured activity (in cps) over the well counter measured activity (in nCi), was the efficiency of the wrist scanner with one set of detectors in operation was 4.0 cps/(nCi/cc) for two detector pairs.

This value matches well with the theoretical calculation of 4.4 cps/nCi/cc. However, taking attenuation into consideration, the efficiency value was calculated as 2.7 cps/nCi/cc. This difference may be as a result of variability in the rejection of attenuated events.

3.4.3 Data Acquisition and Image Formation

3.4.3.1 Selection of acquisition parameters

Energy Window

The lower level discriminator sets a threshold energy (E) for counting. It must be set to its optimum value for maximum sensitivity to true photons while rejecting low energy scattered photons. If the system has high energy resolution (narrow photo peak), the LLD can be increased to filter out the scattered photons as shown in Figure 3.9

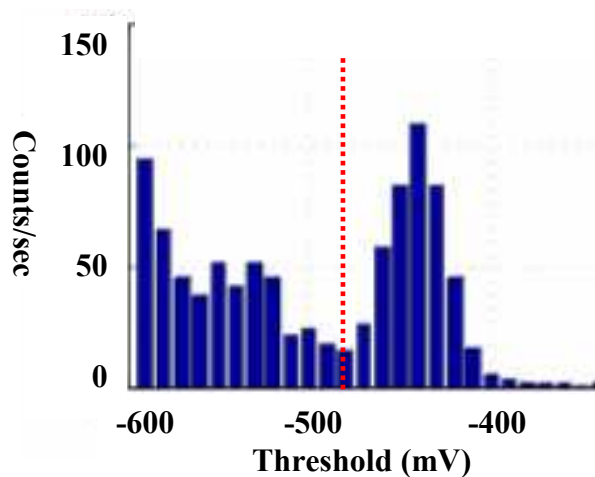


Figure 3.9 Determination of LLD threshold for detection of photo peak

The data acquisition system for the wrist scanner does not store energy information for each singles event, a “threshold scan” was carried out to collect the energy spectra. A

⁶⁸Ge point source was scanned in the center of the field of view while the LLD setting

was stepped in increments of 10mV over the range of 100-700mV. At each setting, the singles rate at each crystal was obtained. The resulting rate vs. threshold spectra were differentiated to give the energy spectra for each of the 128 $((8*4)*4)$ channels. The threshold at which the lowest gain channel could be detected was selected as the operating threshold, and is averaged at 150 keV.

The fact that the low threshold will cause channels with higher gain to detect a number of scattered photons makes this method far from ideal, especially since an error in the assembly caused the ratio of the maximum and minimum photo peaks to be extremely large. The average energy resolution at 511 keV was 23% FWHM.

3.4.3.2 Focal Plane Imaging

Each detector pair operates in coincidence, and data is collected in list mode. Figure 3.10 illustrates the sequence of events leading to the formation of images. On the detection of a coincidence event, the electronics decode the raw x and y coordinates of the coincidence on opposing detector faces.

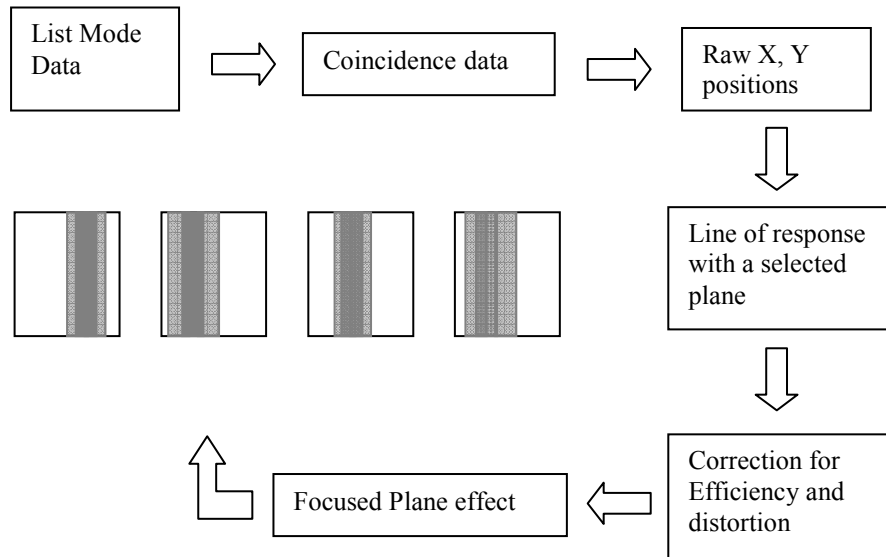


Figure3.10: Basic flow of data acquisition and limited-angle projection used in formation of wrist images.

Most of the events take place in the artery at a relatively well known depth within the wrist based on the anatomical position of the arteries. In order to use all the counts in a 3D mode, a mapped image can be formed at that known depth, or z-depth as seen in figure 3.11. This reconstructed map is also known as focal plane imaging. This method of image formation is similar to that used in the early tomographic systems of the 1970s, before switching to annular rings and is frequently used in dual detector Positron Emission Mammography (PEM) units (Doshi, 1999; Thompson, 1994). However, since only two detector pairs are used (because of economic reasons) focal plane imaging will be the method currently used for the detection of the input function.

Once x and y has been calculated, the z -depth can be used to determine the position of the focal plane image. With the use of exact coordinates of the event on the focal plane image is extracted using a look up table. An image using focal plane imaging will be extracted through using an adjusted z -depth or position of the artery (usually it may be estimated based on the girth of an individual's wrist). In this case, the phantom had a z -depth of 1.9 cm. The only drawback to this concept is that events which occur at another focal spot will add its events to the focal spot of interest. This type of noise may have to be subtracted, but it was not applied here since the noise was seen to be minimal. Also, it is because of this drawback that annular reconstruction is preferred since it separates each of the events into a proper projection in the sinogram (chapter 1). However, for simplicity and economic cost, dual detectors and its complimentary focal plane imaging will be the current method of choice

A 3D line equation was used for tracing rays between randomized end point locations on opposite detector heads. Counts are allocated to the pixel through which the LOR passes. Given two points (x_1, y_1, z_1) , and (x_2, y_2, z_2) , for a certain depth z , x and y can be calculated.

$$\frac{x - x_1}{x_2 - x_1} = \frac{y - y_1}{y_2 - y_1} = \frac{z - z_1}{z_2 - z_1} \quad (3.4)$$

Figure 3.11 shows an illustration of using a 3D line equation to find the exact x and y co-ordinates of the plane of interest, i.e. at the arterial depth of the wrist (assumed to be 1.9)

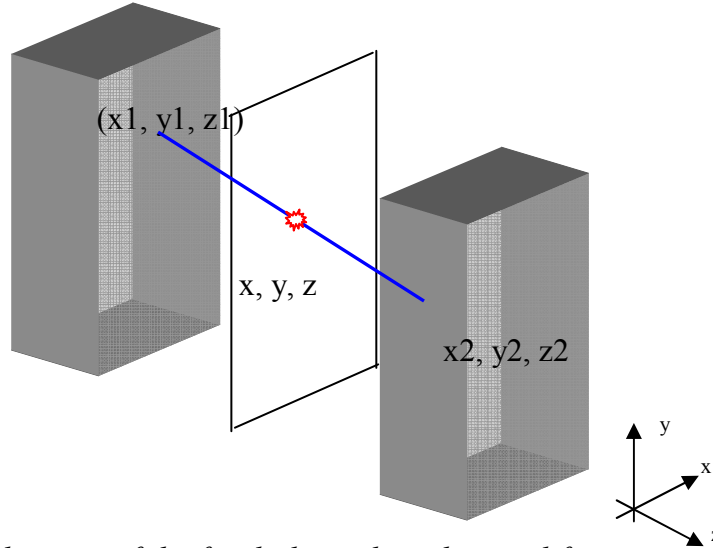


Figure3.11: Schematic of the focal plane algorithm used for reconstruction of the blood vessels.

Coincidence data was then sampled in the ‘1 or 3- nearest neighbors (NN)’. Each combination combines a different number of LORs, e.g. ‘1-NN’ accepts coincidences between directly opposite crystals and their immediate neighbors. Figure 3.12 illustrates this configuration. This mode produces a 2-D, 15x7 matrix of the activity distribution between the two detectors. A MATLAB code was written to produce this matrix of 105 pixels. Each pixel is 1.1 mm x 1.1 mm.

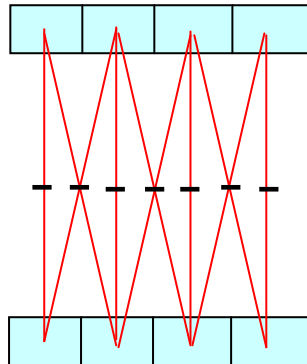


Figure 3.12 : Lines of response between detector pixels of 2 detectors. The ray path spacing in the plane midway between the detectors is half the detector spacing. An image plane is represented by the dotted line

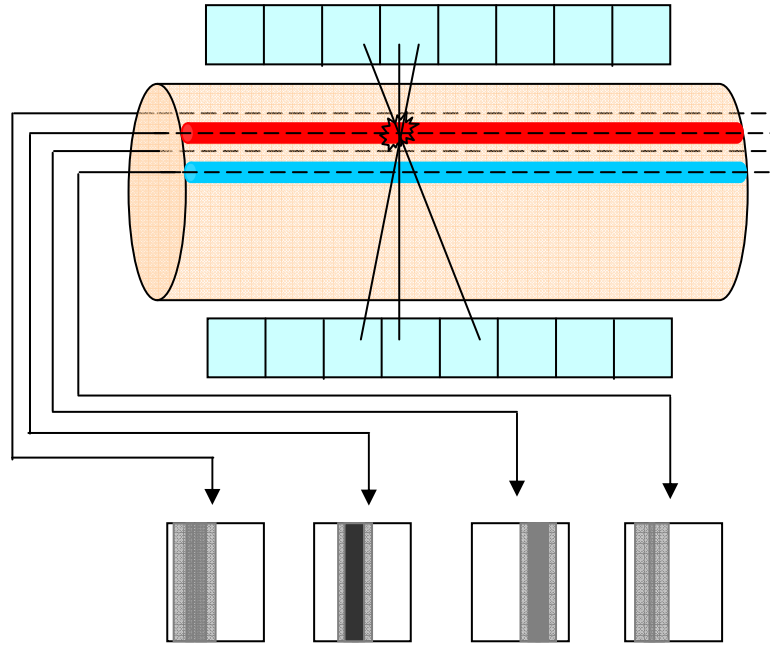


Figure 3.13: Formation of planar images: Volume of the wrist between detectors is divided into equal slices. Point of interaction of LOR with the planes is used to localize event in that plane. Final image set consists of 7 frames, each of which corresponds to 1 slice

The wrist volume between the detectors was divided by equidistant planes. The point of interaction of the LOR with the desired planes is determined. A number (whose value is inversely proportional to the product of the probability of detection of an annihilation in that plane and the crystals' efficiencies) corresponding to the crystal element identified, is added to the image matrix. The method has the advantage of producing the focal plane effect, as a result of which the image frame closest to the site of preferential radiotracer uptake has the most focused image (figure 3.13). With prior knowledge of the thickness of the wrist, the distance of the blood vessel from the upper detector can be estimated.

3.4.4 Normalization

Images require corrections for nonlinearity and nonuniformity of the detector elements; hence normalization data was acquired for the scanner. Normalization coefficients for each line of response of the scanner were obtained by acquiring a scan of a uniform cylinder that almost filled the FOV filled with F-18 in the chemical form of FDG. The size of the phantom was 3.5 x 2 x 1.5 inches. The projection of relative detector efficiencies ϵ is the ratio of this randoms-subtracted projection to the average value of the image. The efficiencies planar image is used as a normalization correction factor. This correction was applied to the counts recorded for each detector pair in a scan by dividing the data from that scan by the normalization image.

The image containing the detector efficiencies is shown in figure 31.4 along with the planar images of measured data from a rod source, before and after normalization in figure 3.15, which shows the improvement in image quality before and after efficiency correction. ROIs on these images demonstrated up to a 19% drop in pixel standard deviation after correction.

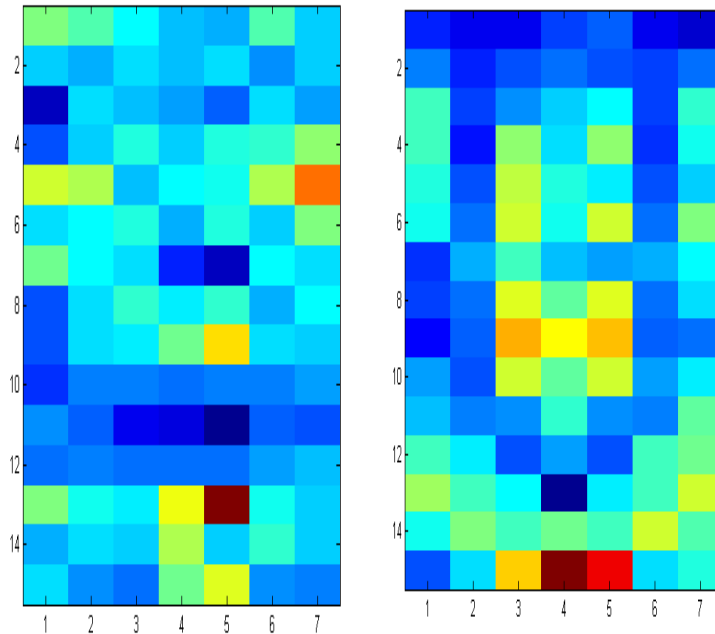


Figure 3.14 Normalization: Planar image of detector efficiencies for the 2 detector pairs

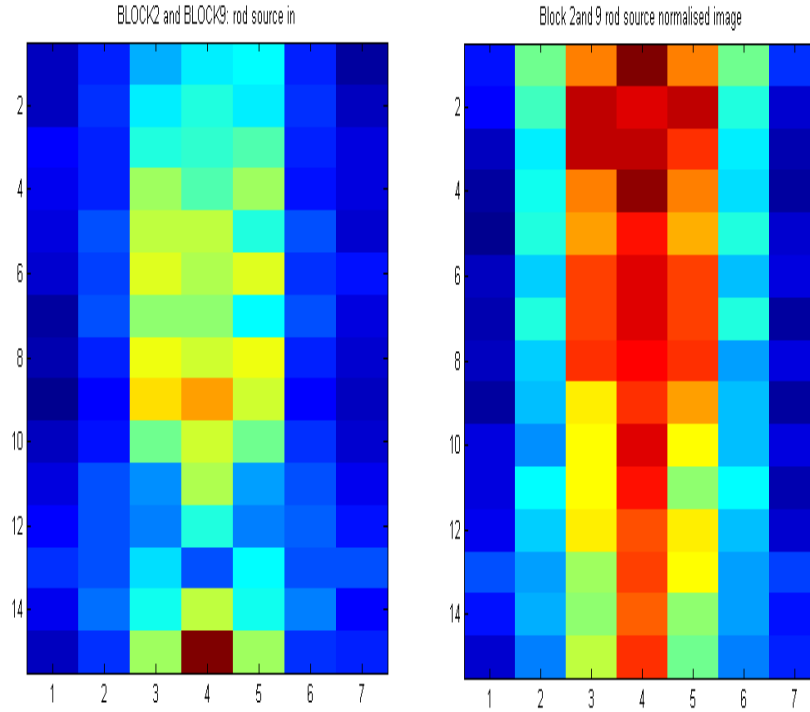


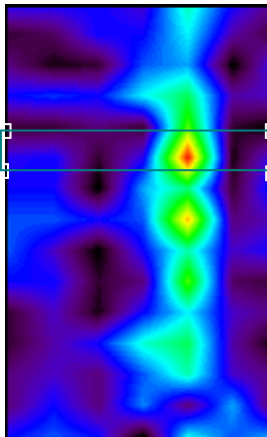
Figure 3.15 Validation of Normalization: Rod source placed between one set of detectors. Left: Before normalization Right: After normalization

3.4.5 Resolution

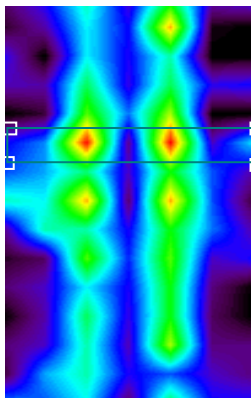
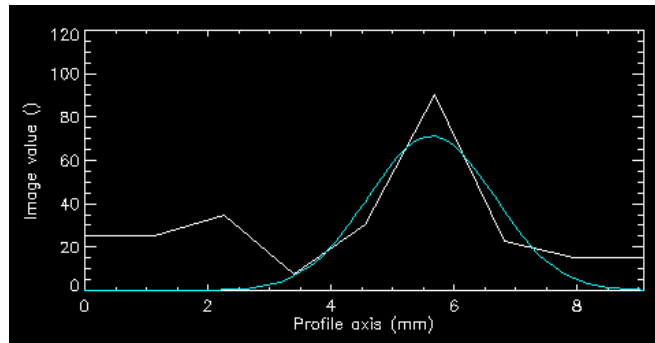
3.4.5.1 Spatial Resolution

System resolution was measured by placing rod sources in the arterial position in the wrist phantom. The uniformity in the system resolution as a function of transaxial distance from the center of the imager in axial distance from the center was also measured. Profiles perpendicular to the axes of the tubes were drawn to produce line spread functions (LSF). The LSFs were fit to a Gaussian function; Full-width-at-half maximums (FWHM) were calculated from the fits and used as measures of system resolution. The results were plotted as a function of distance from the center of the imager. (Figure 3.16)

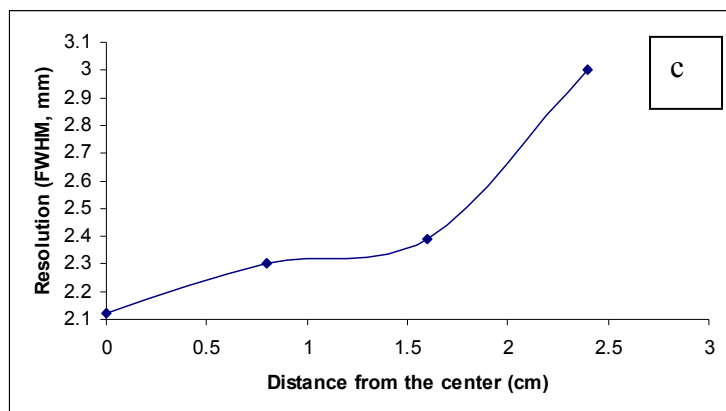
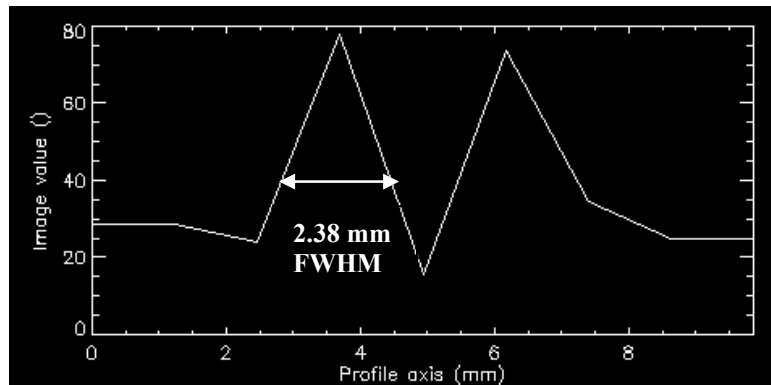
This procedure is a slight deviation from the recommended National Electronics Manufacturer's Association (NEMA) protocol. The technique used was considered more appropriate to assess the resolution uniformity of a planar imaging system that utilizes focal plane images, instead of the NEMA resolution protocol which is intended for systems utilizing tomographic reconstruction algorithms.



a



b



c

Figure 3.16(a) shows the resolution in the center of the FOV is 2.12 mm. (b) is a spatial resolution measure with two ^{68}Ge rod sources in the field of view whose centers are 4 mm apart. Its projection profile along the horizontal axis is also shown (c) shows a plot of system resolution as a function of axial distance from the center of the imager. Note that the resolution measured with the focal plane equal to source position increased slightly as distance from the center increased. The FWHM of the LSFs at the arterial position was 2.39 mm. It degraded from the center of the imager towards the end by 12%. This effect is expected, and is due to changes in the solid angle subtended by the detectors.

Image Resolution

An experiment was done to determine if the image resolution of the scanner was sufficient to clearly distinguish the arterial and venous blood vessels which are in close proximity to each other. The centers of arterial and venous lines are 4mm apart. To estimate the spatial resolution, a series of experiments were done with 1 mm diameter Ge-68 rod sources placed in the artery and/or vein channels in the wrist phantom. Counts were collected for approximately 150 seconds and a high resolution planar image was generated to determine if the artery can be visually separated from the vein.

Figure 3.17 is a planar image of a Ge-68 rod source inserted into 2 channels of the wrist phantom. The planar image can be used to estimate the sensitivity and the uniformity of the block-detector system. In the image, the radial artery and vein are clearly separated. The image will be used to place regions of interest over the arteries in the wrist that can then be used to generate the time activity curve for the input function.

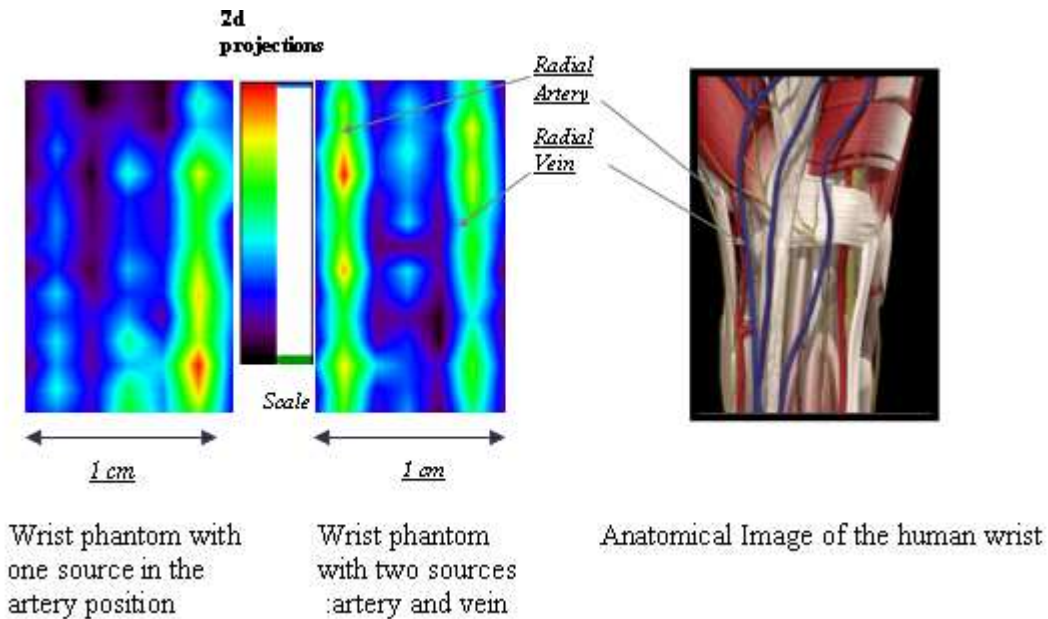


Fig 3.17. Left: A planar image of the wrist phantom taken with 1 mm diameter Ge-68 rod source placed in the artery and vein channels in the wrist phantom. Right: The anatomical view of these vessels. (Wrist figure source: <http://www.human-anatomy.net/anatomy-wrist-pictures.html>)

3.4.6 Scatter fraction

NEMA performance measurement for scatter is done using line sources placed at several locations within a cylindrical, water-filled phantom specified by NEMA (NEMA performance measurement of PET). The procedure used for the scanner was a departure from the NEMA protocol. Specifically, the use of a plane phantom was different. This deviation from the NEMA protocol was dictated in order to estimate the scatter fraction expected in tissue as opposed to a generic measurement of scatter. In the measurement of an input function from the wrist arteries, scatter will cause errors in the reconstructed radioactivity concentrations.

The Compton scatter fraction of the scanner was measured by imaging a uniform phantom of 3.5' x 2' x 1.5' (figure 3.18). The phantom was filled with water containing an FDG concentration of ~0.120 mCi/cc. The phantom was positioned on the detectors and imaged for 600 s. The scatter fraction was determined by placing ROIs on the planar image, assuming the mid plane of the scanner for the z depth.

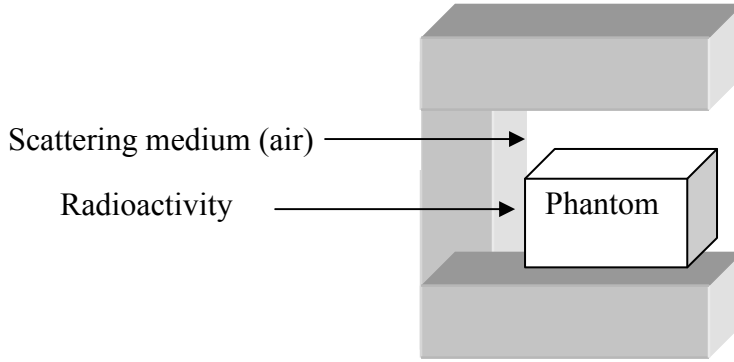


Figure3.18 Experimental setup for scatter estimate

A ROI was also placed on a plane which was outside of the phantom. The maximum pixel value from the ROI drawn on the planar image of the non phantom area was divided by the average of the maximum pixel values measured from the compartment containing FDG. The Compton scatter fraction was determined to be 18% (+/- 2%) detector separation of 5.2 cm and energy threshold of 150 keV. This should improve with the higher threshold that we are able to use now.

3.4.7 Contrast

Contrast resolution of the detector was quantified using the tubing set up similar to the efficiency measurement set up shown in figure 3.8. The true contrast was measured by calculating the activity in the arterial tubing to that in the venous return line. The contrast ratios were calculated as follows

$$C_{true} = \frac{A_{art_tube}}{A_{vein_tube}} \quad (3.5)$$

$$C_{av} = \frac{A_{art}}{A_{vein}} \quad (3.6)$$

Where A is the average signal as obtained using a ROI on the region. With the same ROI, signal-to-noise (SNR) was calculated as

$$SNR = \frac{A_{art}}{\sigma_v} \quad (3.7)$$

Table 3.1 shows the contrast for and SNR values for the venous return experiment.

Ctrue	Cav	SNRav
22	6.69	8.23
12	5.49	7.51
19	6.17	7.14

3.4.8 Count Rate Performance

Noise equivalent counts (NEC) analysis condenses the behavior of a PET system into a single metric and is widely used to assess PET imaging performance. It is used in quantifying the effect of random and scatter coincidences on the statistical quality of the acquired data (Strother, 1990).

$$NEC = \frac{T^2}{T + S + f_{fov}(1+k)R} \quad (\text{Eq. 3.8})$$

where T,S and R are the true, scatter and random coincidence rates respectively, f_{fov} is the fraction of the FOV occupied by the object and k reflects the variance contributed by the random coincidence estimation method.

A NEC measurement was performed to assess count rate capability of the Wrist Scanner system. A 21 cc uniform phantom, which partially filled the FOV ($f_{fov} = 0.60$) with activity was filled with ~ 1 mCi of ^{18}F and scanned during its decay. Prompt and delayed coincidences were extracted from the singles data, and the rates of trues, randoms, and NEC are plotted in Figure 3-19.

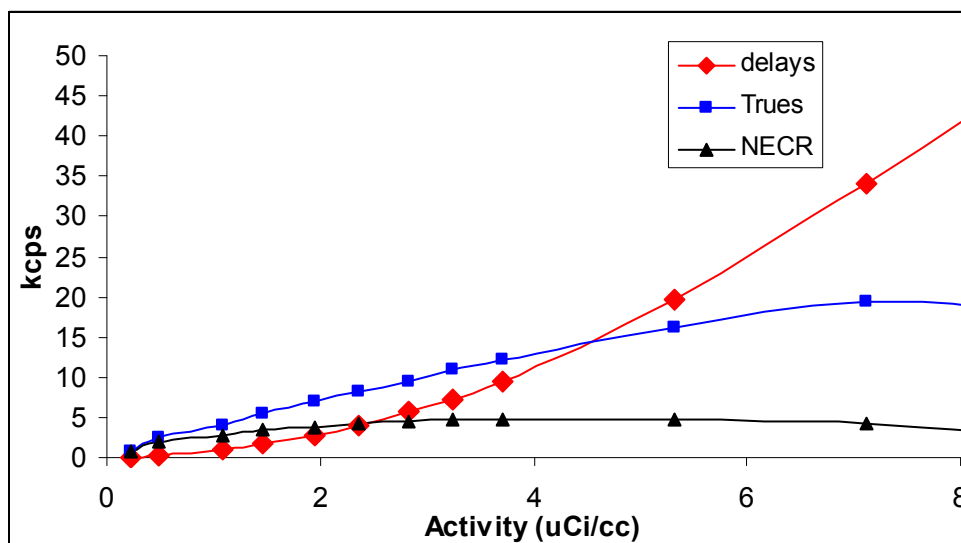


Figure 3-19 Rates of true coincidences, random coincidences and noise equivalent counts as a function of activity concentration

Scatter fraction of 18%, as seen in 3.4.6, was used for these calculations. A reduction in the amount of scattered and random coincidences would improve the NECR rate. This can be accomplished with improved correction methods.

3.5 Human Studies

The four-detector prototype was used in six routine human PET studies. The subjects were injected with 5-6 mCi of [^{11}C]raclopride or 4-5 mCi of 2- ^{18}F fluoro-2-deoxy-D-glucose (FDG). The radial and ulnar arteries were marked on the subject's wrist by the physician. This aided placement of the two arteries between the detector blocks. To provide maximum resolution of the artery from surrounding tissue, the scanner was positioned with its long axes parallel to the artery. Every subject had two catheters inserted for each scan; a standard arterial catheter in the radial artery for the sampling of arterial blood and a second catheter in the antecubital vein for radiotracer injection. During the PET scan, the arterial blood was sampled by using an automated blood-sampling device (Ole Dich, Denmark), which draws a 0.4 ml samples of blood every 2.5 seconds for the first 2 minutes. Blood samples were then drawn manually every

minute from 2–6 min, then at 8, 10, 15, 20, 30, 45, and 60 min. Each arterial blood sample was centrifuged and a sample of plasma assayed in a well counter. In case of [^{18}F]FDG the hand with the arterial catheter was heated to 50°C to draw arterialized venous blood. After [^{18}F]FDG was injected, arterialized venous blood was sampled by using the automated blood-sampling device. The Wrist Scanner was placed in the arm which was also the radiotracer injection site. The invasive arterial samples were used for a gold standard comparison.



Figure 3.20 Human Wrist Scan

Only three out of the seven studies performed with the wrist scanner had useable data for analysis:

1. One subject was scanned without lead shields for making an estimate of the random coincidences with and without shielding.
2. The small wrist sizes of two subjects did not allow the correct placement of the wrist.

Focal plane reconstruction procedure as described in section 3.4.3.2 was used to generate planar images. Dynamic sequences of the wrist (figure 3.21) emphasized the mis-positioning of the scanner. The streak on the left is the radial artery and the streak in the center may be the radial vein. Figure 3.22 shows a time vs. activity plot derived from drawing regions of interest on the planar images. Decay corrected TACs were drawn for arterial and background tissue ROI's. An arterial ROI was drawn on the ulnar artery. To

estimate the spillover, a tissue ROI was also drawn. The ROIs consisted of summed columns of activity for the two ROIs.

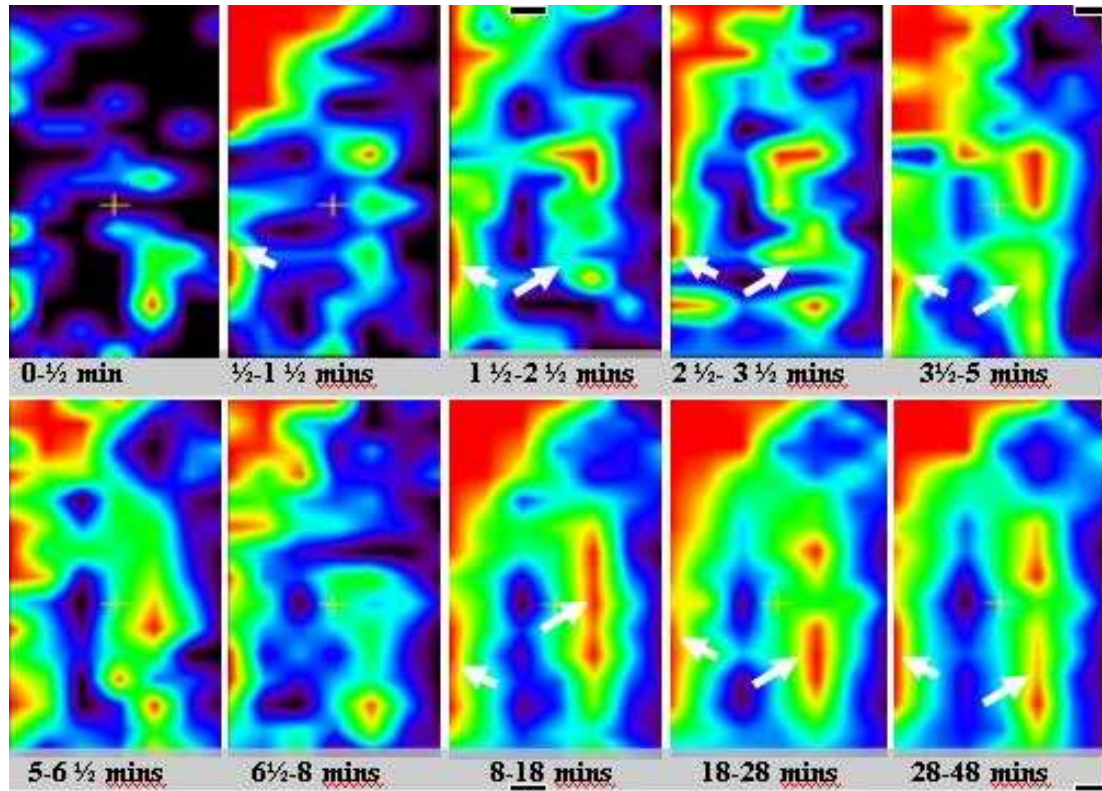


Figure3.21: Planar images for a $[^{18}\text{F}]\text{FDG}$ study.

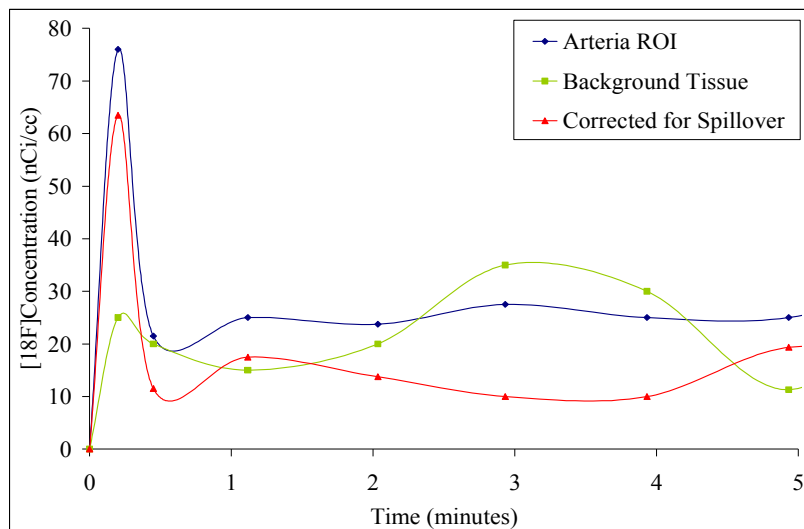


Figure3.22: Time activity curves for arterial ROI, background ROI and subtracted curve.

A recovery coefficient was used to correct for partial volume effects, caused due to the limited resolution of the scanner and the size of the blood vessels. These corrections are discussed in detail in chapter 4 (Tomographic images of the wrist using a small animal scanner). Figure 3.23 shows the TAC from the wrist scanner and from invasive blood samples. The two curves are very similar in shape. The Wrist Scanner TAC shows a characteristic peak and exponential decay of activity with time.

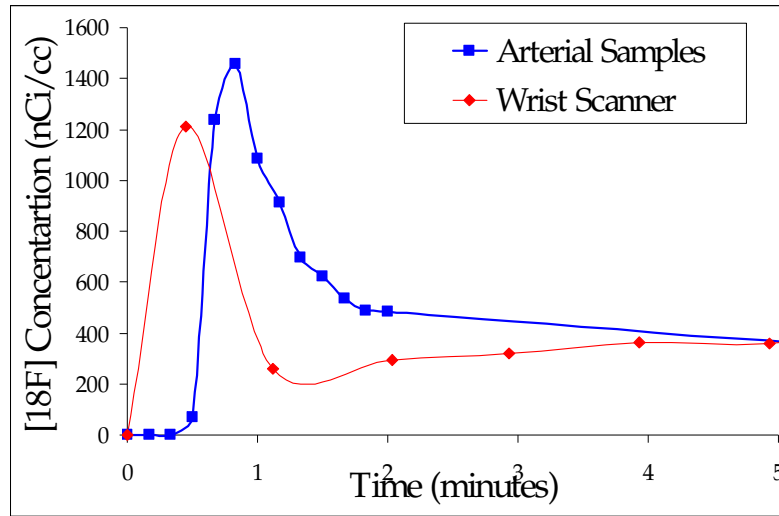


Figure: 3.23 Comparison of the TACs from the Wrist Scanner and Arterial samples

3.6 Effects of Nearby Sources

The amount of radioactivity in the wrist arteries is very small relative to the total amount of radioactivity in the body. Background radioactivity from the nearby body and surrounding wrist tissue presents a major challenge. Since the injection was done in the arm with the wrist scanner, the number of delays would increase considerably without shielding.

To assess the effect of threshold and timing coincidence window length on the random rate, a flood source was used in the field of view of a two detector array with an oval source of about 10 times the strength extending from just outside the field of view to 10 cm away. The singles, coincidence, and random coincidence rates for different

threshold and coincidence timing window settings. The delay for the delayed coincidences was 56 ns. The signal integration time (gate length) was 390 ns. The rates were measured using a visual scaler which was not affected by DAQ dead time, and also with a CAMAC scaler that would reflect the DAQ dead time. These results are shown in Table 3.2

Table 3.2 Data from a measurement of count rate with sources inside and outside the field of view

Duration	Coincidence timing window	Energy Threshold	Prompt Events	Delayed Events	Ratio Prompt/Delayed
8:00	40 nsec	400 keV	26014	7838	3.32
8:00	40 nsec	250 keV	88625	27504	3.22
8:00	20 nsec	400 keV	14033	2077	6.76
8:00	20 nsec	250 keV	61405	11181	5.49

This table shows that for this particular configuration, using a 20 ns coincidence timing window and a threshold of 400 keV results in a ratio of prompt to delayed coincidence events of 6.76. This can be compared to a 40 ns coincidence timing window with a 400 keV threshold where the coincidence ratio is about 3.32. The clear conclusion is that by making the coincidence timing window as narrow as possible, we can greatly reduce the number of random coincidence events in this detector arrangement.

To more accurately assess the effect of shielding the wrist scanner from the body, a 1.2 cm (0.5 inch) lead shield was placed on the body side of the prototype 4 detector wrist scanner. Two separate studies were done where the subject was injected with 5-6 mCi of FDG, one with the shielded scanner in place and one with the unshielded scanner. Using a 20 nsec timing window and a 150 keV threshold, our average ratio of prompt to delayed events went from 2.7 for the unshielded case to 6.1 for the shielded case. The energy threshold was set this low as a result of not being able to adjust the gain on each channel.

3.7 Discussion

Based on the experiments described in the above sections of this chapter, important conclusions were made, paving way for future work. There are a number of effects that confound accurate measurement.

Sensitivity of 4 cps/nCi/cc is low for detecting of activities typical seen in the wrist. There are many factors that can contribute to this loss in sensitivity for instance, the field of view, gamma or light photon detection and the electronic system itself. Aside from the problems of sensitivity; imaging and derivation of an input function can also be improved through, for example, arterial co-registration with MRI, or scatter background corrections. For improving the scanner's sensitivity, there may be several considerations on how the detector and its accompanying components will be constructed and placed in a real clinical experiment. The geometrical effects had two factors that determined the sensitivity, one being the solid angle efficiency and the other the vertical counting efficiency. Both of these factors are dependent on the wrist size of the patient. Since human patients vary in wrist sizes; subjects with a smaller wrist diameter will have a better sensitivity than a larger diameter (mostly because for the larger diameter the solid angle on the detector is decreased). The vertical efficiency remains the same when assuming the artery is scaled to a fixed position in the wrist. Therefore, to improve the detection on the larger diameter subjects more detector pairs may be used. Although the sensitivity will be higher with a smaller wrist, the errors in the measurement will be greater due to the smaller volume and the higher partial volume effect.

The response function of the system varies with position, so the efficiency for detecting activity in the artery depends strongly on position. The horizontal position may be estimated from the image, but the vertical position cannot be measured accurately. The dynamic focal plane imaging program requires prior knowledge of the position of the arterial blood vessel to ascertain the region of activity in the image. Since the program uses the depth of the blood vessel, two different depths give different count totals. If the wrong depth position was to be given, an inaccurate count total may be produced. Also,

partial volume effect is a major one, which will be affected by patient to- patient variation in the artery diameter. A MRI co-registration step for the determination of the blood vessel position would ascertain and validate the z depth and partial volume effect corrections. This would require taking an MRI image of the patient's wrist to get a clearer picture of where the arterial blood vessel is positioned along the length of the wrist and provide a depth parameter for the FPI program. The high resolution detector arrays produce an accurate two dimensional image separating venous activity, since the radial and ulnar veins are separated laterally from the arteries. Planar images have almost no resolution in the third dimension, so the artery will overlap with a significant amount of other tissue in the wrist and activity in the surrounding tissue may interfere with the arterial activity measurement. To evaluate this interference and explore an annular ring wrist tomograph, the MicroPET scanner was used to collect images of a human wrist during a routine PET study.

A major hurdle in quantifying wrist data with certainty was the threshold voltage at ~150 keV. Raising the threshold to 450 keV would also decrease the scatter. Therefore, optimization of the threshold level could increase contrast ratios, reducing scatter and improving NEC curves.

The rigid geometry of the scanner did not allow for both the arteries to be in the field of view, hence the scanner could be placed only on one of the arteries. The planar image (figure 3.21) shows a hot streak, which is the ulnar artery. The incorrect positioning of the scanner with respect to the arteries will change the signal to noise ratio and hence the absolute quantification of the data. Therefore, flexibility of adjusting the detectors should be conceived in the next prototype to take care of various wrist sizes.

Placement of the scanner will be a critical issue, since the detector is only 4 pixels wide and it must be positioned such the artery is in the field of view. The next prototype will be conceptualized so that at least the adjacent detectors can be adjusted to sit precisely for radioactivity measurement from the arteries.

3.8 Conclusion

By improving the hardware sensitivity and image quality, applications such as kinetic analysis would also be improved in calculating metabolic rate constants and quantities of indicator radiotracer concentrations. The human experiments emphasized that the placement of the scanner is a major concern and should be dealt with in the next prototype design. Nonetheless, the characteristics of the input function, peak height, time to peak and area under the curve are comparable to the invasive arterial samples. Precise calibration and knowledge of individual subject artery location, wrist thickness, and precise positioning are main concerns at this point.

Chapter 4

Tomographic Images of the Human Wrist using a Full Ring Tomograph

4.1 Overview

Aim: Images of the ulnar and radial arteries obtained with the wrist scanner will have partial volume effects which complicate the estimation of an input function. This chapter provides a proof of principle for extraction of an input function from tomographic wrist images and the methods for correction for the partial volume and spillover effects present in the wrist scanner images.

Method: A small animal scanner, the MicroPET R4, was used to acquire radioactivity concentration in the human wrist during the uptake period of 2-[^{18}F] flouro-2-deoxy-D-glucose (FDG). To recover the radioactivity counts lost due to the small size of the arteries (~2-3mm) and limited spatial resolution of a scanner (MicroPET~ 2.6 mm), a recovery coefficient (RC) was used. The image derived input function (IDIF) was corrected using this RC value for 5 subjects. Invasive arterial samples were also taken for gold standard comparison. Finally, metabolic rate of glucose (MRglu) was calculated using the Sokoloff model.

Results: The characteristics of the curve (area under the curve, peak height, time to peak) and the MCRglu for the IDIF and invasively sampled arterial input function (AIF) did not differ significantly ($p < 0.05$). The shape of the two curves also matched well. The RCs for five subjects were adjusted such that the MRglu for the IDIF match the arterial plasma input function (AIF) and finally an average of these ratios will be used for partial volume correction in absence of the knowledge of blood vessel caliber.

Conclusion: The results have demonstrated the feasibility of using a tomographic wrist scanner and the ability to compensate for the small size of the wrist arteries and resolution of the scanner.

4.2 Specific Aims

Tomographic images of the wrist help to evaluate the potential of extracting an input function using a ring detector. The main reasons for acquiring tomographic images are:

1. The 4 detector prototype has a sensitivity of 4cps/nCi/cc (discussed in previous chapter). An increase in sensitivity will be desirable to quantify radioactivity in the arteries.
2. Focal plane imaging works effectively in two dimensions. The artery and the vein are laterally separated from each other and hence can be separated using a planar projection. However, there will be no discrimination in the third dimension and so the artery will overlap with a significant amount of tissue. This chapter estimates the tissue activity in the wrist that may interfere with the arterial radioactivity measurement.
3. Due to the small size of an object of interest and limited resolution of a scanner (Hoffman, 1982), partial volume effects result in loss of quantification of data. Tomographic images of the wrist will help to evaluate and compensate for these effects.

A small animal scanner was used to collect images of a human wrist during routine [^{18}F] FDG studies. In these experiments, the MicroPET R4 small animal scanner (Concorde Microsystems Inc.) was positioned next to the Siemens HR+ PET scanner bed. Five subjects were injected with 4.5-5.5 mCi of [^{18}F] FDG (Hamacher, 1986). Every subject had two catheters inserted for each scan; a standard arterial catheter in the radial artery for the sampling of arterial blood and a second catheter in the antecubital vein for radiotracer injection. The hand with the arterial catheter was heated to 50°C to draw arterialized venous blood. After [^{18}F]FDG was injected, arterialized venous blood was sampled by using an automated blood-sampling device (Ole Dich, Denmark), which draws a 0.4 ml samples of blood every 2.5 seconds for the first 2 minutes. Blood samples were then drawn manually every minute from 2–6 min, then at 8, 10, 15, 20, 30, 45, and 60 min. Each blood sample was centrifuged and a sample of plasma assayed in a well counter. These were used for gold standard comparison of the IDIF from the wrist image.

The hand with the injection site was placed in the field of view (FOV) of the MicroPET scanner. At the injection of the tracer, sequential PET scans of the wrist were collected for the radiotracer uptake period of 30 minutes. The data was binned to match the sampling of arterial blood. Images were reconstructed using filtered back projection with a ramp filter cutoff at the Nyquist spatial sampling frequency (0.444 mm)

4.3 Correction for Partial Volume and Spillover on ROIs

The location of a radioactive point source in the field of view (FOV) can only be determined with a resolution quantified by the full width at half maximum (FWHM) of the point spread function (PSF) of the tomograph. Under the assumption that the tomograph is a linear system, the PET image of an extended radioactive source can simply be obtained by convolving the true radioactivity distribution with the PSF. The correction for finite detector dimension thus consists in deconvolving the PET image with the PSF, operation which is commonly referred to as partial volume correction.

When the size of an object is more than twice the FWHM of the PSF, the PET image contains voxel values which are linearly related to the radioactivity concentration in the object. This relation no longer holds for smaller objects. Accurate inference of the true object size and radioactivity concentration from the PET image then requires knowledge of the response of the tomograph as a function of object size and shape (Hoffman, 1979). The recovery coefficient is defined as the ratio of the apparent radioactivity concentration in the image to the true radioactivity concentration in the object, and is determined specifically for the tomograph and reconstruction parameters used. When the object size and shape as well as the tomograph PSF are known, pre-determined RC values can be used to correct the radioactivity concentration measured in the image. A fraction of the object radioactivity spills out to the background, and the object is contaminated by radioactivity that spills in from the background. Equation 4.1 is used to correct for these effects.

$$A(t) = RC \times C_p(t) + SF \times B(t) \dots\dots\dots 4.1$$

$A(t)$ is the concentration of radioactivity as measured by the scanner and is assumed to be a linear combination of two components: the true radioactivity from the blood vessel ($C_p(t)$) and the radioactivity from the surrounding tissues ($B(t)$). RC and SF are partial volume and spillover fraction from the surrounding tissue.

The simple geometry of the radial and ulnar arteries in the wrist allow the approach of Kessler (Kessler et al 1984) to be used for the correction of the non-negligible effects of partial volume and spillover. Counts that spilled out of the blood vessel into surrounding tissue need to be recovered, especially soon after the bolus injection (Figures 4.1a-c)). At later times, after the radiotracer has perfused in the surrounding, counts that spilled into the blood vessel from surrounding tissue need to be subtracted (Figures 4.1d-f)).

The RC values can be derived analytically from a simple simulation. The blood vessel is modeled as a cylinder with a circular cross-section and the surrounding tissues are assumed to have a uniform radiotracer uptake. A grid of 0.1 mm x 0.1 mm pixels is first created. Pixels located within a given radius from the center of the grid are assigned a value of unity whereas those outside this area are set to zero. This binarized disk is then convolved with a two-dimensional Gaussian function having the measured transaxial FWHM of the tomograph and an area normalized to unity. Circular ROIs of increasing diameter are centered on the grid and the average pixel value within each ROI is computed on both the binarized and blurred disks. The recovery coefficients are finally calculated for a set of ROIs and a blood vessel of a given caliber as $RC = ROI \text{ (blurred disk)} / ROI \text{ (binarized disk)}$.

To estimate the spillover, pixels located within a given radius from the center of the grid are assigned a value of zero whereas those outside this area are set to one. This inverse grid was similarly convolved with a two-dimensional Gaussian function and ROIs were drawn. The spillover fraction (SF) was calculated as $SF = ROI \text{ (inverse blurred disk)} / ROI \text{ (inversed binarized disk)}$.

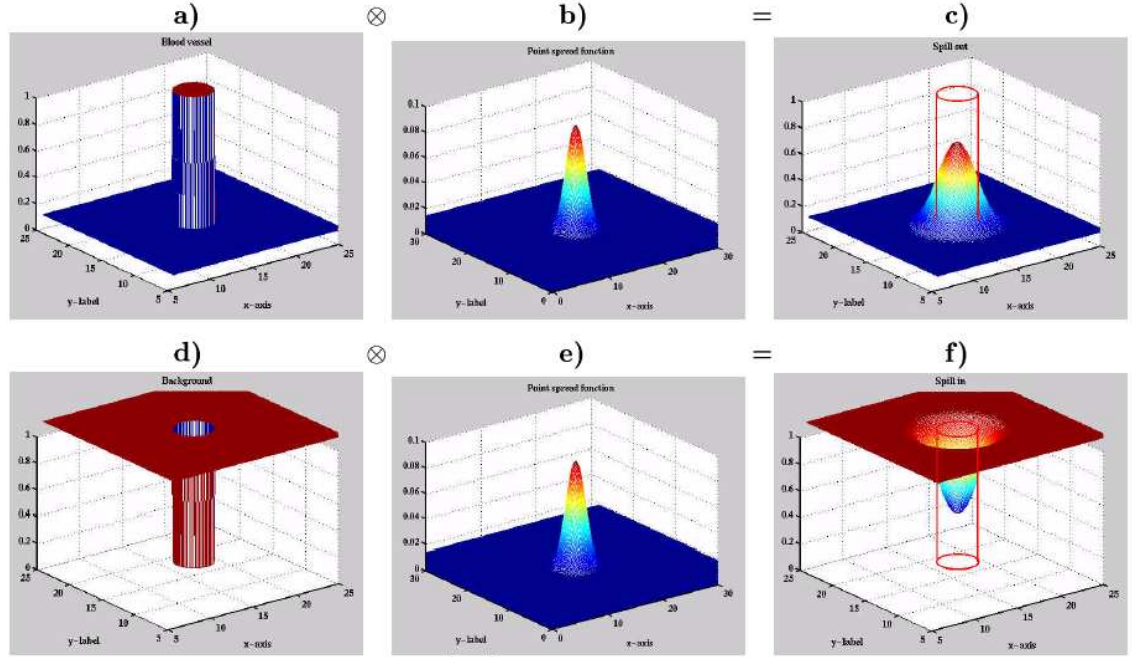


Figure 4.1 a)-c) Counts that spill out of the blood vessel in to the surrounding tissue need to be recovered; d)-f) Counts that spill into the blood vessel from the surrounding tissue need to be removed.

The accuracy of the RC estimates was assessed by imaging a mini Derenzo Phantom (Data Spectrum, Chappel Hill, North Carolina) in the MicroPET scanner. The phantom consists in six sectors with tubes of diameter 4.8, 4.0, 3.2, 2.4, 1.6 and 1.2 mm. The tubes were filled with an F-18 solution of approximately 1uCi/cc at the start of the first scan. It was scanned for 20 minutes and the images were reconstructed using the same 3D filtered back projection algorithm as used to reconstruct the human wrist images. Referring to the original definition of Hoffmann *et al*(1979), the RC values were calculated for each tube as the ratio of the radioactivity concentration measured in ROIs of diameter ranging from 0.6 to 3 mm over the decayed radioactivity concentration of the F-18 solution. RC was defined as:

$$RC_{roi} = C_{tube} / C_{injected}$$

An anti-Derenzo phantom was used to estimate the spillover fraction, where the tubes were solid and the rest of the phantom was hollow. The SF correction fraction was

calculated by drawing the ROIs for the tubes to estimate the amount of radioactivity in the phantom (background) that spilled into the tubes. The measured RC and SF values were compared with those predicted by the simulation described above which was performed for each tube and each ROI with FWHM=2.6 mm corresponding to the measured spatial resolution of the Concorde MicroPET R4.

4.4 Region of Interest Analysis

Dynamic wrist frames over the period of first 2 minutes were summed. This will optimize drawing ROIs due to better visualization of the blood vessels. The summed image was then examined visually for the arteries. On this summed image, circular ROIs (diameter=1.5 mm) were drawn manually around the voxels having the highest radioactivity concentration at the expected location of the radial and ulnar arteries. In order to correct for the spillover effects relating to the blood vessel, a background ROI was delimited as an annulus (outer ellipse area= 2 cm^2 , inner circle diameter= 4 mm) around the arteries. The diameter of the inner circle of the annulus defining the background region was set to the sum of the blood vessel caliber (assumed to be 0.4 cm) and twice the FWHM of the tomograph in order to avoid spillover from the blood vessel into the background region. All ROIs were overlaid on the dynamic PET images to generate the time course of the radioactivity concentration in blood and tissue.

4.5 Compartmental Analysis: Sokoloff Model

The MRGLc was calculated using a built in program called MetabTool in the ECAT/HR+. In this program, the lumped constant (LC) is a given number in the calculation. The glucose plasma concentration, C_p , is entered as the measured input function and the k^* variables in the formula of 4.7 are entered as given k^* values. The values are: LC: 0.520, k_1 0.095, k_2 0.125, k_3 0.069 k_4 0.0055. The program will be estimating local MRGLc values and it will vary by each individual's input function and imaged data. Therefore, this is a useful method to evaluate if the corrected input function results in good estimations of the kinetic metabolic rates (Takikawa, 1993).

4.6 Results

4.6.1 MicroPET acquisitions of the wrist

The reconstructed wrist images using the FBP reconstruction technique are shown in the figure 4.2. The image shows that you can clearly, visually delineate the artery from the background tissue. Hence drawing the ROIs on these images would be a direct and simple way of extracting the radioactivity. The TACs from drawing ROIs on these arteries and the surrounding tissue is shown in figure 4.3

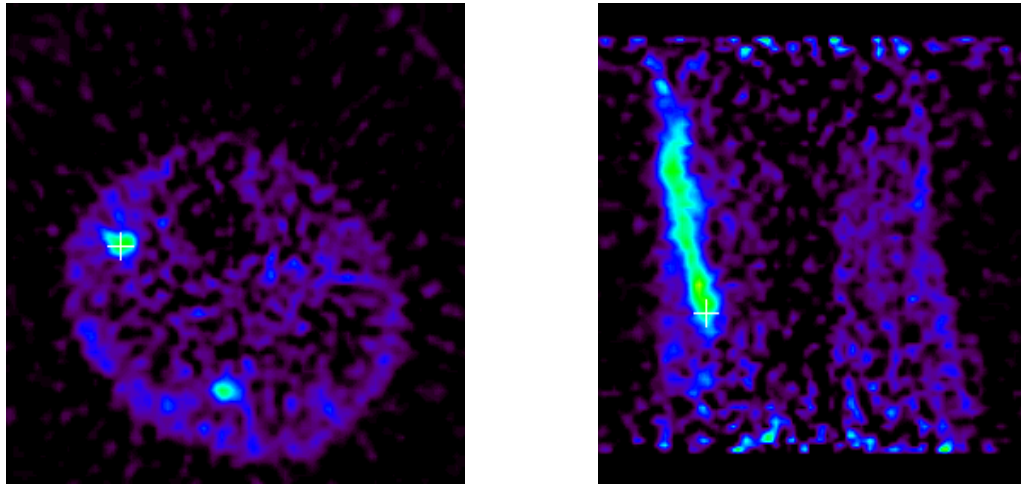


Figure 4.2 Sagittal and transaxial view of the wrist in the MicroPET

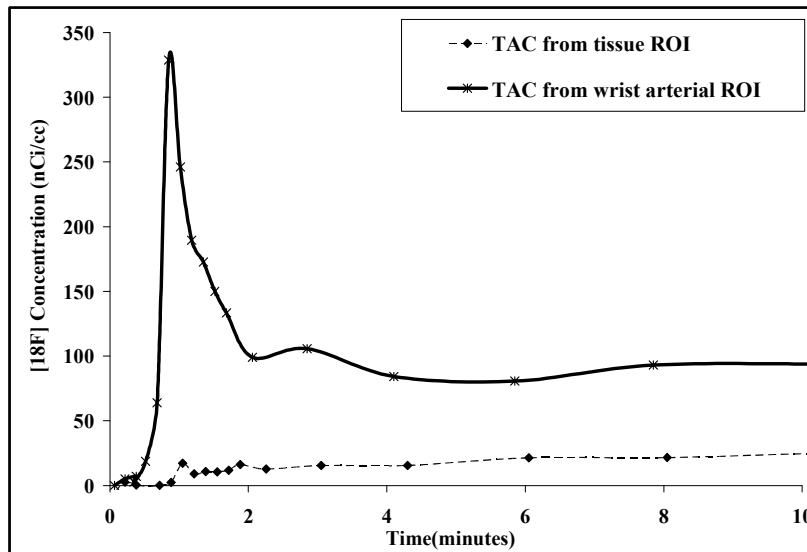


Figure 4.3 Time activity curves from the MicroPET images for the arterial and surrounding tissue

An ROI of the size of the wrist was drawn and radioactivity through the projection of the wrist was calculated as 12% of the arterial radioactivity. Furthermore, the spillover fraction of tissue radioactivity (shown below table 4.1) is approximately 9%.

4.6.2 Correction for Partial Volume and Spillover

The Derenzo and anti-Derenzo phantom pictures are shown in figure 4.4

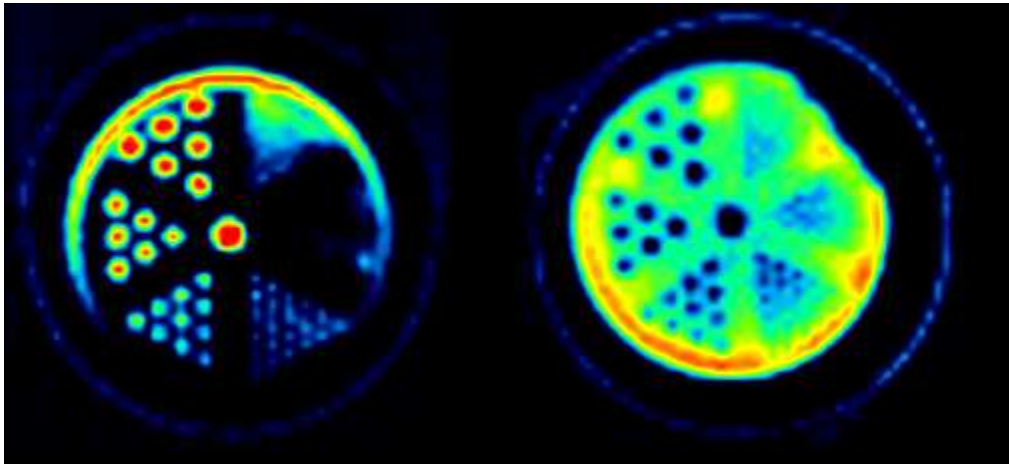


Figure 4.4 Derenzo and anti-Derenzo phantom used for RC calculation in the MicroPET

The recovery coefficients measured experimentally are compared in figure 4.5 with those derived analytically for the tubes of the Derenzo Phantom. The phantom had a 4.8 mm diameter tube, two times the FWHM and hence the radioactivity concentration could be almost fully recovered (85%) in the ROIs. Shape differences between the experimental points and the analytical curves may result from the approximation of the tomograph PSF by a Gaussian function in the simulation. Highest RC values are obtained for the smallest ROIs. Furthermore, the underestimation of the true radioactivity concentration worsened severely with decreasing tube size. For ROIs of diameter half of the tube, the analytical RC values were estimated to be 0.82, 0.76 and 0.70 for the 4.0, 3.2 and 3.0 tubes, respectively.

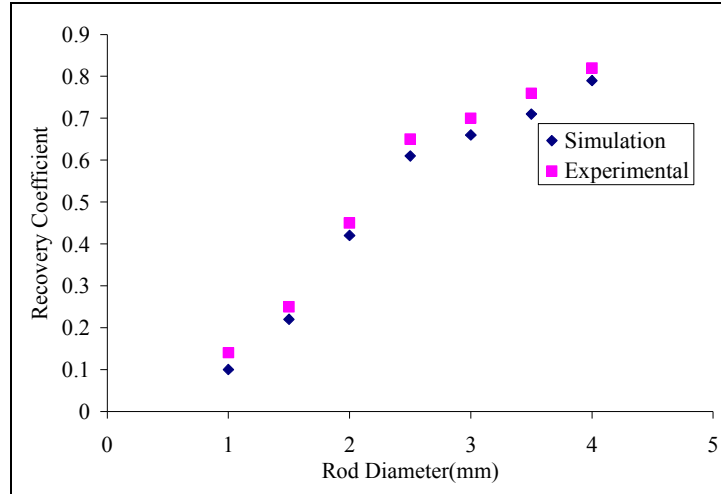


Figure 4.5. The recovery coefficients measured experimentally are compared with those derived analytically for the tubes of the Derenzo Phantom.

Table 4.1 Recover Coefficient and Spill over from the phantoms

	2	2.5	3	3.5	4
PV	0.458	0.654	0.702	0.7632	0.82
STD DEV	0.055	0.056	0.06	0.066	0.07
SF	0.1209	0.102	0.0922	0.09	0.0845
STD DEV	0.019	0.025	0.01	0.016	0.02

The ROI diameter is a user-defined variable; the blood vessel caliber and spatial resolution of the tomograph are fixed. For these studies, the diameter of the wrist arteries was assumed to be 3.0 mm. The spatial resolution of the tomograph is spatially variant; hence the value for the FWHM was estimated at the position of the blood vessel from the measurements of a line source. The smaller ROIs produce larger RC values, but at the expense of a greater sensitivity to small variations in the tube diameter and increase in noise. Figure 4.6 further illustrates that the choice of the ROI diameter becomes more critical with the PET cameras offering a better spatial resolution, at least for tubes smaller than twice the FWHM of the scanner. It was also observed that for a given ROI diameter and blood vessel caliber, the magnitude of the partial volume correction is reduced as the spatial resolution of the tomograph improves.

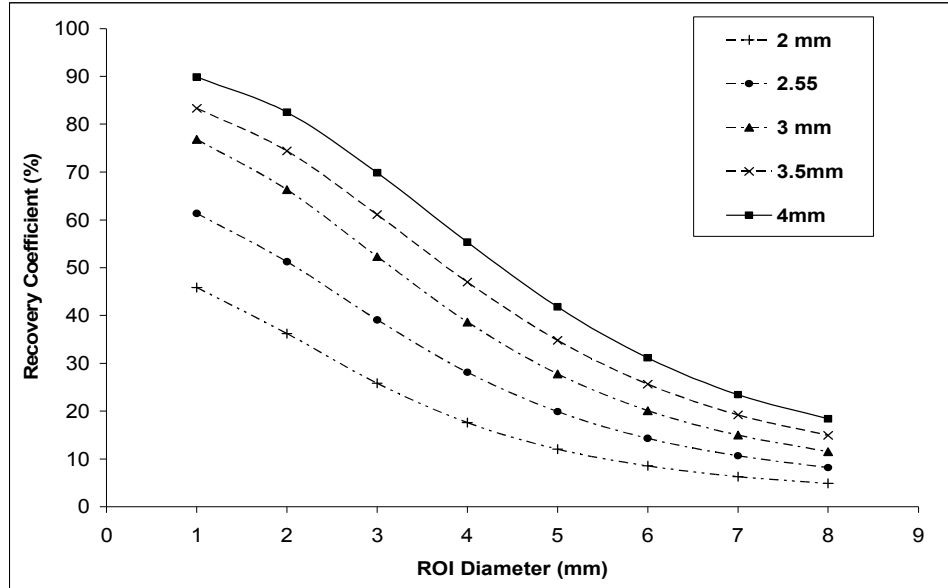
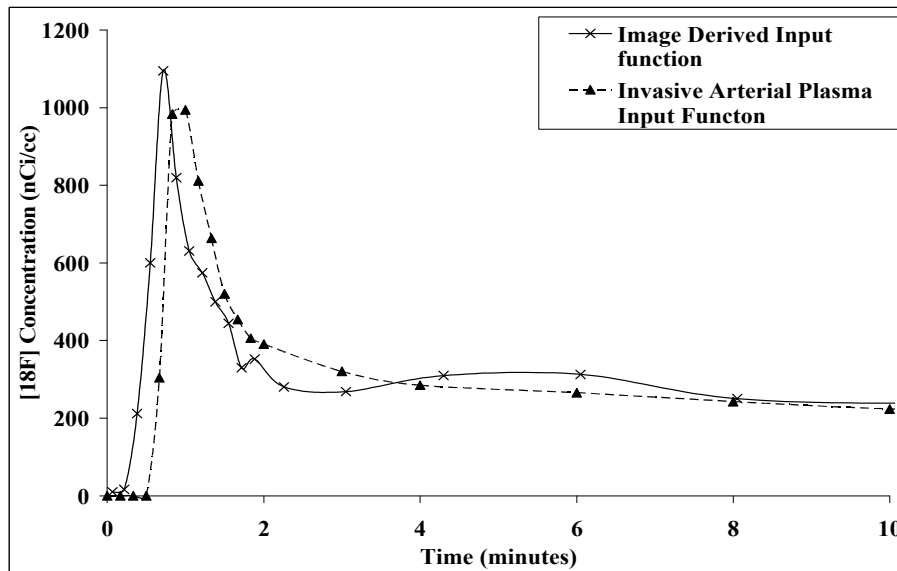
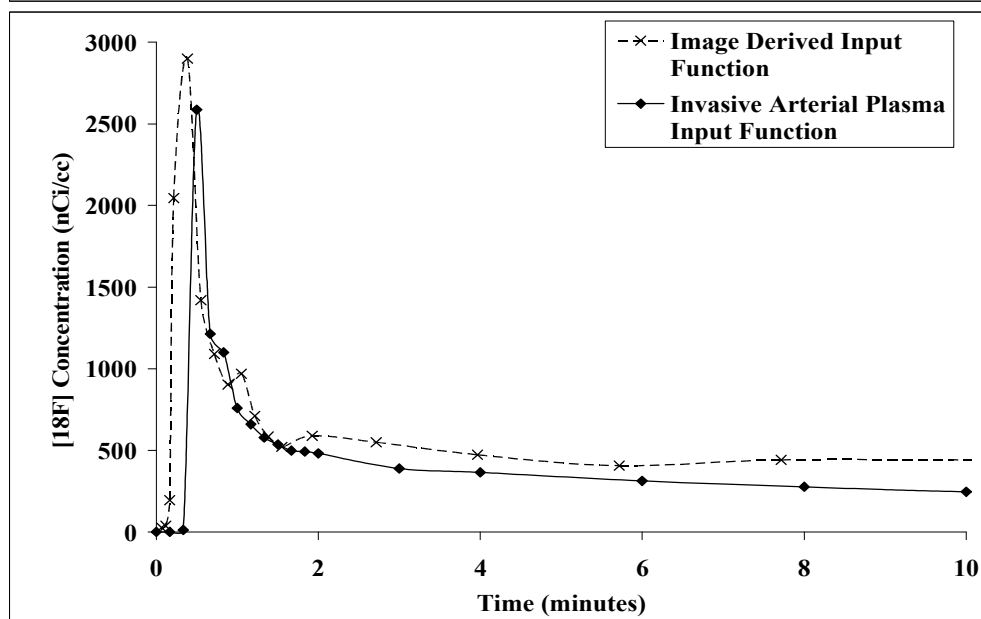
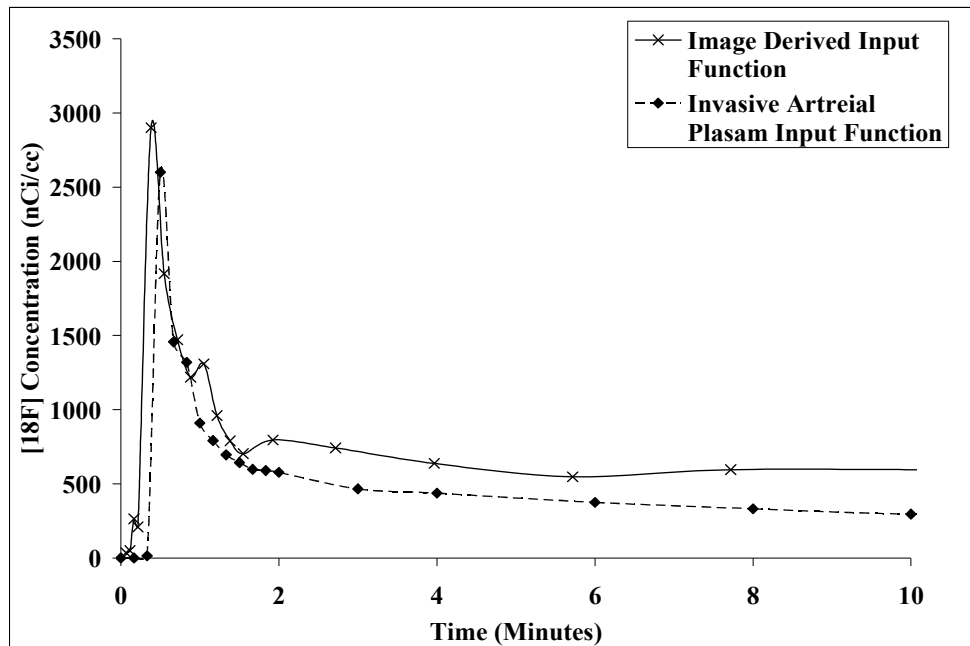


Figure 4.6 Variation in the recovery coefficient with the choice of the ROI diameter for a tube of a particular diameter.

4.6.3 Input functions direct comparisons

The corrected ROI-based input functions are compared with the directly sampled arterial plasma input functions in figure 4.7. As shown in table 4.2, all ROI-based blood curves peaked earlier than the directly sampled curve for both the tracers.





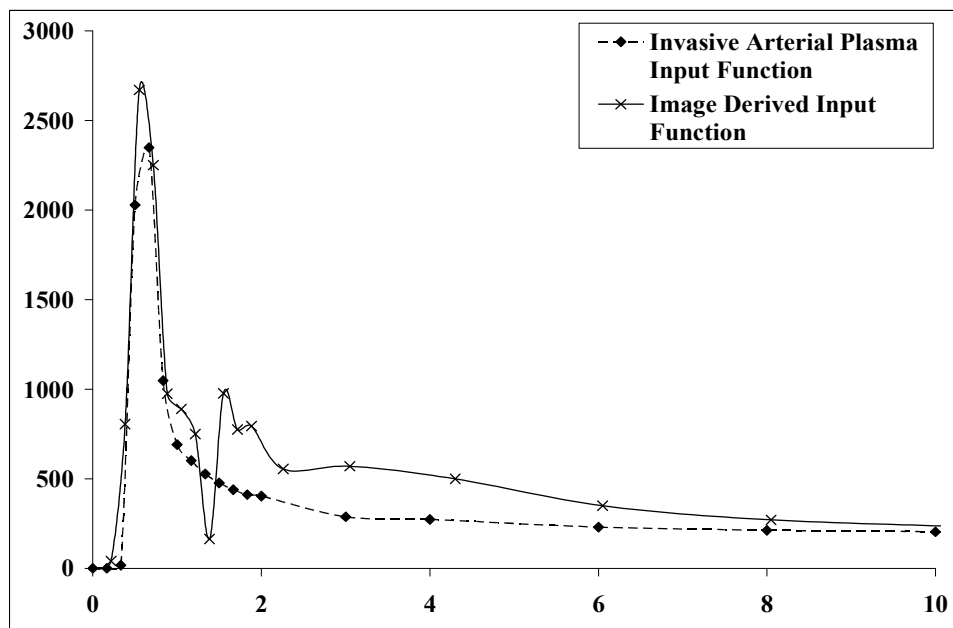
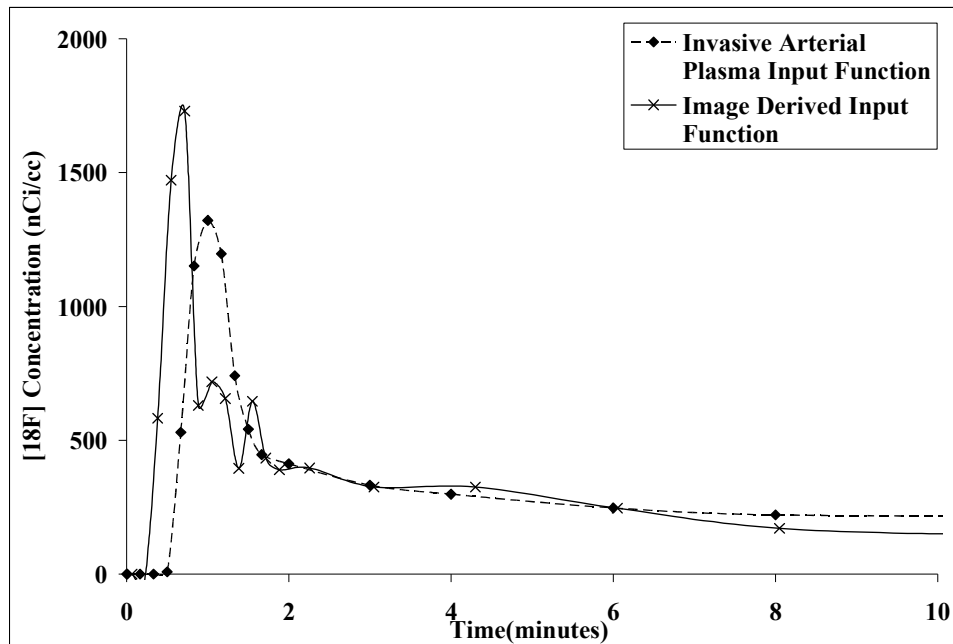


Figure 4.7 Image Derived input functions derived from wrist images are compared to the invasive arterial plasma input functions for five subjects.

Table 4.2: Comparison of the input functions: Peak position, height and AUC

	Time to peak	Peak Height	AUC (0-2 minutes)
	(seconds)	(nCi/cc)	(μ Ci/cc)
AIF	60	994	3134
IDIF	42.6	1094	3984
AIF	30	2600	6357
IDIF	22.8	2900	10107
AIF	30	2586	6418
IDIF	22.8	2899	5156
AIF	60	1321	4060
IDIF	42.6	1729	5822
AIF	40.02	2349	7823
IDIF	33	2670	10180

A two tailed t-test with 5% significance level showed that the peak heights were significantly different for the IDIF and AIF. However, the total integral under the curves and time to peak did not differ at $p < 0.05$

4.6.4 Metabolic rate of Glucose

The IDIF and arterial blood sampled input function (AIF) was used as an input to Sokoloff model. The ROIs were drawn on the thalamus for each subject in each case. The graph in figure 4.8 below compares the MRGLc.

The error bar on the ‘invasive arterial samples’ data is the standard 8% deviation due to the counting statistics and scanner characteristics. The RC value (0.70) used for the correction of image derived TACs was based on an average size of the wrist arteries. This value was varied from 0.50 to 0.75 and the values of CMRglu was calculated. This variation is reflected in the error bars shown in figure 4.8.

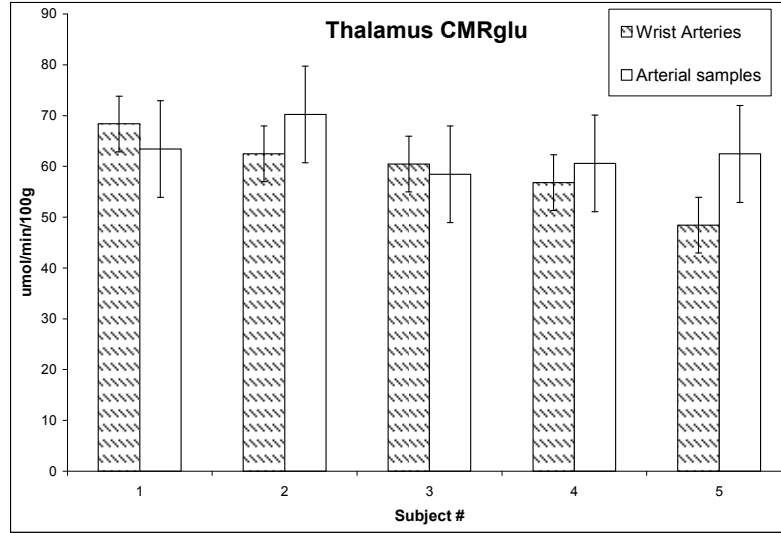


Figure 4.8 MRGLc calculated for the 5 subjects compared for IDIF and arterial blood samples.

4.7 Discussion

The results of Sokoloff model using the image derived input function were similar to those obtained using the directly sampled input function, despite the peak differences of the two input functions. The variation in the MCRglu due to the error in an input function is 8% (Huang, 1980). Partial volume correction reduces bias in the blood TAC extracted from images at the expense of introducing variance. Averaging over several planes and curve fitting was shown to be sufficient for data extracted from the wrist arteries. The proposed method requires that ROIs of a given diameter be drawn manually on the blood volume image. Small ROIs correspond to high RC values, thereby limiting the magnitude of partial volume correction; large ROIs are more robust to statistical noise and variations in the blood vessel caliber. The choice of the ROI diameter is thus a compromise between these factors. The difference in the shape of the ROI-based blood TAC compared to the directly sampled blood TAC probably reflects in the large part errors in the correction for partial volume and spillover. To be more accurate, the correction should employ the actual size of the blood vessel for each individual (Strul and Bendriem, 1999). This approach has been explored in the next chapter, for internal carotid arteries visible in the brain PET scans and the size of which was obtained from

the MRI scan of the same subject. It was also seen that the directly sampled blood is confounded by the delay and dispersion occurring at the peripheral blood sampling site. The accuracy of the directly sampled blood TAC is also dependent upon the cross calibration between the PET camera and the radiation detector used to count the radioactive blood. These problems are circumvented by the extracting the time course of radioactivity in the blood from the PET images, hence insuring compatibility between blood and tissue data.

For ^{18}F -FDG the difference between the plasma F-18 concentration and the one in whole blood can be ignored for human subjects. This assumption was validated in a previous study (Gambhir, 1989) for the 120-minute time period. Because the total scan duration is only 30 minutes, this assumption can be honored safely. However, because this is a significant consideration for the use of blood data in kinetic analyses, it is considered in the next chapter for two C-11 tracers.

4.8 Conclusion

The method presented in this chapter provides non-invasive blood input function for PET brain studies using a full ring wrist scanner. Since the blood input function is extracted from the PET images, this method removes the need for the correction for delay and dispersion associated with blood sampling and cross calibration. The method however depends on user input to delineate the wrist arteries, and is subjective. One drawback is that this method requires prior knowledge of the blood vessel caliber. Nonetheless, the characteristics of the curve and the CMRglu match closely for the IDIF and the AIF. The results have thus demonstrated the use of a tomographic wrist scanner and compensation for the small size of the wrist arteries with respect to the resolution of the scanner.

Chapter 5

Derivation of a Blood Time-Activity Curve from Brain Images

5.1 Overview

Aim: The purpose of the work presented in this chapter was to evaluate the feasibility of a non-invasive approach for obtaining a blood input function from dynamic PET brain studies without arterial cannulation.

Method: The method is based on regions of interest (ROIs) drawn on the internal carotid arteries visible in the human PET brain images. The use of a recovery coefficient for compensation of lost counts (discussed in the previous Chapter 4: Tomographic Images of the Human Wrist using a small animal scanner) was extended to the carotid arteries and the human ECAT EXACT HR+ scanner, for the extraction of a non-invasive image derived input function (IDIF). The ROI-based method used for partial volume and spillover correction was verified to be accurate when applied to glass tubes filled with a radioactive solution. Five subjects injected with [^{11}C]raclopride and four subjects injected with [^{11}C]clorgyline were studied in the high resolution, high sensitivity ECAT EXACT HR+ tomograph after the intravenous injection of the tracers. The time course of radioactivity in cerebral blood, corrected for partial volume, spillover and metabolites of the tracer (using venous samples), was compared to that in the arterial blood sampled on-line. The tissue curves were first fitted with compartmental models. This tissue data were also analyzed using two-tissue compartmental model for irreversible tracers and multiple time graphical analyses with the blood data. The results of the compartmental and graphical analyses on PET data using the IDIF were compared with those obtained using the directly sampled arterial plasma input function (AIF) in order to evaluate the accuracy of the newly proposed method.

Results: The shape of the two input functions matches closely, but the IDIF peaked earlier and higher than the AIF. The integral over the curve as well as the kinetic parameters calculated for both tracers are not significantly different ($p < 0.05$)

Conclusion: This method of non-invasively obtaining a blood input function for quantitative analysis of PET brain data provides a compromise between simplicity and accuracy adequate for use with the clinical population.

5.2 Introduction

There were two main reasons for applying the technique of IDIF to dynamic human brain images

1. Theoretically, the use of a recovery coefficient should suffice for partial volume correction, if the three dimensional orientation of the object and system characteristics are defined. This chapter investigates the use of a recovery coefficient, as described in the previous chapter, for obtaining the radioactivity concentration in the cerebral blood from ROIs drawn on the internal carotid arteries in humans. The size of these arteries was exclusively obtained for each subject from their respective MRI scan. This will help in validation of simple ROI analysis using a major blood vessel in the field of view.
2. To make complete use of an image derived TAC, metabolites of the parent radiotracer have to be corrected for, since a PET image cannot differentiate between a tracer and its metabolites. For the MicroPET studies, a wrist could only be scanned during the uptake period of [^{18}F]FDG, because of the placement restrictions in using the HR+ scanner and MicroPET simultaneously. Hence no other tracer could be tested for the wrist scans. Also, for the duration of the wrist scan, this glucose analog does not metabolize and hence does not require additional corrections (Chen, 1998). It would be reasonable for the scope of this thesis to explore and evaluate the behavior of IDIF technique for different tracers, in an effort to relate the correction technique with the tracer's behavior. Hence, two ^{11}C radiotracers, [^{11}C]raclopride and [^{11}C]clorgyline were utilized to investigate the use of venous samples to correct for the presence of metabolites of the authentic tracer in the blood. Venous samples were obtained at 1, 5, 10 and 30 minutes. These samples were used to estimate % unchanged radiotracer for the IDIF and past 5 minutes they were used to calibrate the tail of the IDIF.

5.3 Materials and Methods

5.3.1 Correction for Partial Volume and Spillover on ROIs

The carotid measure 4 to 5 mm in diameter and the measured spatial resolution of the ECAT EXACT HR+ in the center of the field of view is 6.8mm. The equation used to correct for the effects of partial volume and spillover, as discussed in chapter 4, will be used to recover the lost counts.

$$A(t) = RC \times C_p(t) + SF \times B(t) \quad (5.1)$$

$A(t)$ is the concentration of radioactivity in the carotid artery as measured by the scanner and is assumed to be a linear combination of two components: the true radioactivity from the blood vessel ($C_p(t)$) and the radioactivity from the surrounding tissues ($B(t)$). RC and SF are correction factors for partial volume and spillover fraction from the surrounding tissue respectively.

5.3.2 Data Acquisition

5.3.2.1 Phantom data

The accuracy of the RC estimates was assessed by imaging a phantom with three glass tubes of inner diameters 3, 4.2, and 6 mm in the ECAT EXACT HR+ camera (CTI/Siemens, Knoxville, TN, USA) (figure 5.1). The tubes were filled with an F-18 solution of approximately 1 mCi/cc at the start of the first scan. It was scanned for 20 minutes and the images were reconstructed using the 3D filtered back projection algorithm with ramp filters set at Nyquist cut-off frequency. The images were corrected for attenuation and scatter. Referring to the original definition of Hoffmann *et al* (1979), the RC values were calculated for each tube as the ratio of the radioactivity concentration measured in ROIs of diameter ranging from 1 to 4 mm over the decayed radioactivity concentration of the F-18 solution. The measured RC values were compared with those

predicted by the simulation described in Chapter 4, which was performed for each tube and each ROI with FWHM = 6.8 mm corresponding to the spatial resolution of the ECAT/HR+ tomograph.

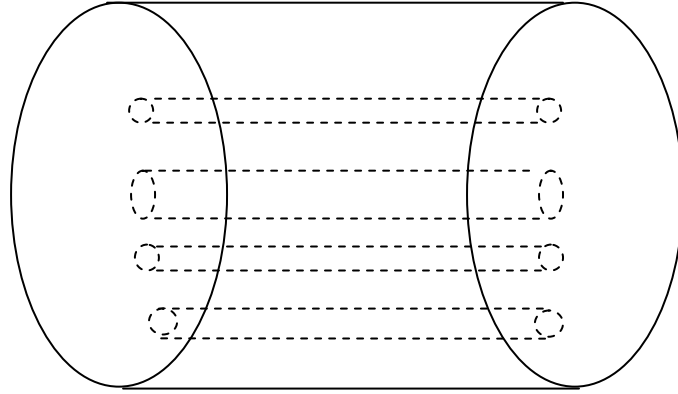


Figure 5.1: Schematic diagram of the phantom used for estimating RC for the ECAT HR+. The phantom consists of a 6mm, a 4.2 mm and two 3 mm tubes.

5.3.2.2 Human data

PET Scans

Nine subjects underwent a sixty minute PET study (ECAT EXACT HR+, CTI/Siemens, Knoxville, TN, USA) after the intravenous injection of 5-7 mCi of [^{11}C]raclopride or [^{11}C]clorgyline. Sequential PET scans were obtained immediately after injection for a total of 60 min with the following frames: 1 x 10 seconds, 12 x 5 seconds, 1 x 20 seconds, 1 x 30 seconds, 4 x 60 seconds, 2 x 120 seconds and 10 x 300 seconds. The images were reconstructed using filtered back projection with a Hanning filter giving a measured image resolution of 6.8 mm in the center of the field of view. Every subject had two catheters inserted for each scan; a standard arterial catheter in the radial artery for the sampling of arterial blood and a second catheter in the antecubital vein for radiotracer injection. During the PET scan, the arterial blood was sampled by using an automated blood-sampling device (Ole Dich, Denmark), which draws a 0.4 ml samples of blood every 2.5 seconds for the first 2 minutes. Blood samples were then drawn manually every minute from 2–6 min, then at 8, 10, 15, 20, 30, 45, and 60 min. Each arterial blood sample was centrifuged and a sample of plasma assayed in a well

counter. Plasma samples at 1, 5, 10, 20, 30, 45, and 60 min were analyzed for [^{11}C]clorgyline and [^{11}C]raclopride (Alexoff, 1995)

Assay of parent radiotracer in arterial and venous blood

For all the subjects a second venous catheter was inserted to draw blood at 1, 5, 10 and 30 minutes. For both the arterial and venous samples, plasma was analyzed for the percentage of unchanged radiotracer using a Sep-pak separation of the labeled fractions in the plasma (Alexoff, 1995; Appendix C). A comparison was made of the percentage unchanged radiotracer obtained with plasma samples obtained through the arterial line with those obtained from the venous line.

Plasma to whole blood ratio

The radioactivity concentration obtained from arterial blood sampling corresponds to the plasma input function, whereas IDIF is a whole blood radioactivity profile. If a radiotracer does not bind to the erythrocytes, then the concentration of the tracer in plasma can be obtained as a ratio of plasma to whole blood ($R_{p/wb}$) of the whole blood concentration. To correct for the fraction of radioactivity in whole blood that is from plasma, we calculated the ratio of the radioactivity concentration at one minute in plasma to that in whole blood, assuming that radiotracer equilibrium is achieved rapidly between the whole blood and plasma. Thus the plasma radioactivity is equal to $R_{p/wb}$ times the true radioactivity in the blood pool (after partial volume corrections).

$$C'_p(t) = R_{p/wb} \times C_p(t) \quad (5.2)$$

MRI acquisitions:

MR images of the nine subjects were obtained with a Sigma 1.5-T system (GE Medical Systems, Milwaukee, Wis). For rapid orientation, a sagittal section (spin echo [SE] 600/20 [repetition time msec/echo time msec] was obtained to localize a fiducial marker 2 cm above and parallel to the canthomeatal line. T1-weighted axial sections (SE 600/20) were acquired with a 5-mm thickness and a 2-mm intersection skip in an oblique plane, parallel to the marker. Axial proton-density (2,500/30) and T2-weighted (2,500/90)

sections were acquired through the brain without an intersection skip in the same plane T1-weighted axial sections. The data were displayed on a 256 x 256 matrix and used to measure the size of the internal carotid arteries for each subject.

5.3.3 Data Analysis

5.3.3.1 Definition of the regions of interest

The PET and MR images were manually co-registered (figure 5.2) using PMOD (PMOD Technologies Ltd). For the PET images, frames were summed over the period of 10s to 50s and examined visually for carotid arteries. On this summed image, circular ROIs were drawn manually around the voxels having the highest radioactivity concentration at the expected location for the carotid arteries. In order to correct for the partial volume and spillover effects relating to the blood vessel, a background ROI was delimited as an annulus (outer ellipse area=13.2 cm², inner circle diameter=1.5 cm) around the carotid arteries. The diameter of the inner circle of the annulus defining the background region was set to the sum of the blood vessel caliber (assumed to be 0.5 cm) and twice the FWHM of the tomograph in order to avoid spillover from the blood vessel into the background region (figure 5.3). Elliptical ROIs were also drawn around the cerebellum (area = 12.7 cm², one on each side per plane) and the putamen, caudate, thalamus and anterior cingulate (area = 1.2 cm², two on each side per plane) on four to six consecutive planes. These ROIs served as target regions for the compartmental and graphical analyses. All ROIs were overlaid on the dynamic PET images to generate the time course of the radioactivity concentration in blood and tissue. The time course of radioactivity concentration measured from the blood vessel was corrected for partial volume and spillover using equation (5.1) with the time course of radioactivity concentration in the background.

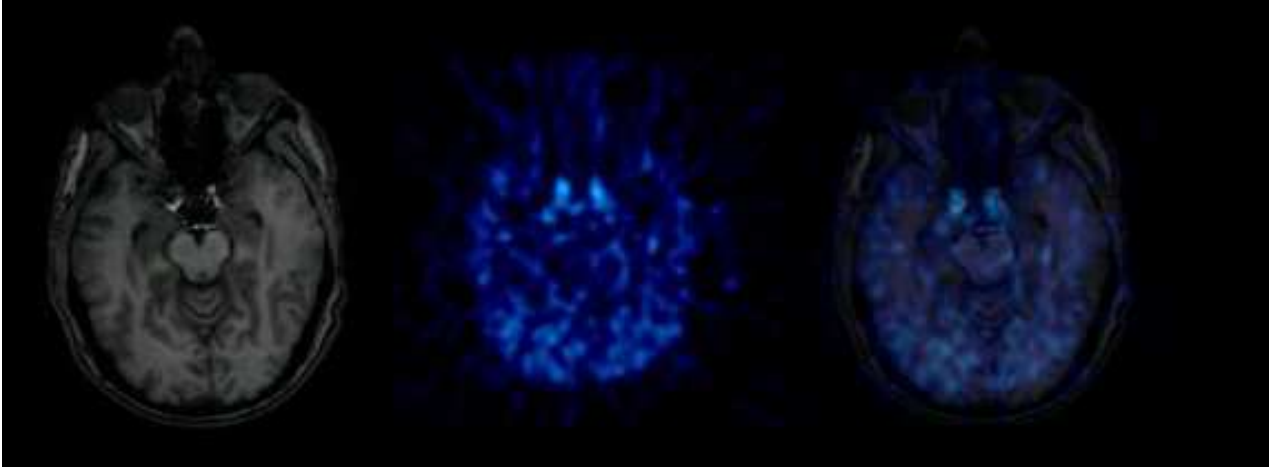


Figure 5.2 a. Left: MRI scan showing the carotid arteries Center: PET image summed for first 40 seconds. Right: Coregistered PET-MR image

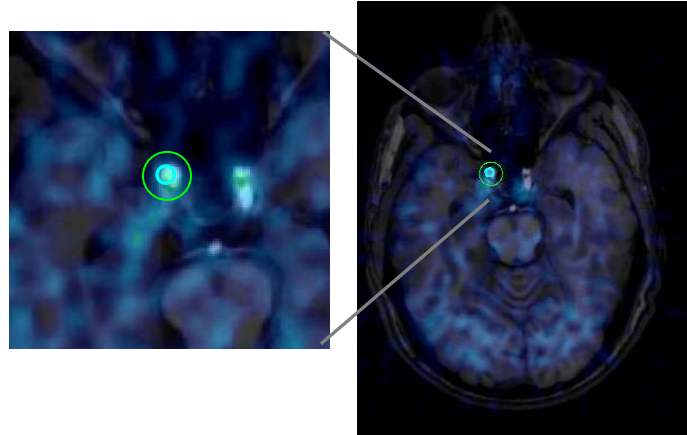


Figure 5.3: Region of interest on the co-registered PET-MRI image. The smaller ROI is used to estimate the arterial activity, and the bigger ROI is for tissue spillover estimation.

5.3.3.2 Noise reduction

Noise in the plasma input function propagates to the fitted tissue TACs through the convolution operation, therefore increasing the uncertainty on the parameter estimates. Two methods of reducing the noise level in the ROI-based blood TAC were investigated:

1. Average ROIs over several planes: The caliber of the carotid arteries was measured to be relatively constant over 5-6cm, thereby allowing ROIs drawn on several consecutive planes (up to 10 on the ECAT/EXACT HR+) to be averaged.

2. Fit the blood TAC with a mathematical function: Sum of exponentials:

$$y(t) = A_1(t) \exp(+\lambda_1 t) + A_2(t) \exp(-\lambda_2 t) + A_3(t) \exp(-\lambda_3 t) \dots \dots \dots 5.2$$

The blood TAC was manually shifted to the origin such that the delay parameter T can be set to zero. This function with six parameters (three A's and three λ 's) mathematically describes a four-compartment model having a pair of repeated eigen values. This model approximates the behavior of a radiotracer in the blood circulation, having been injected in a venous space and being sampled in an arterial space after having transited through tissue vascular and interstitial spaces (Feng *et al*, 1993).

5.3.3.3 Comparisons of input functions

Direct Comparisons:

The ROI-based TACs were then corrected for blood partition and radiolabeled metabolites using venous samples, in order to be used as plasma input functions to the cerebellum, striatum and thalamus. After these corrections, the peak height, time to peak and total integral of the ROI-based blood IDIF were compared with those of the directly sampled arterial plasma input function.

Comparisons of kinetic terms

The effects of using the input functions derived from either arterial plasma sampling or the PET images on the results of both compartmental and graphical analyses were also evaluated. A three compartment irreversible model was used for [^{11}C]clorgyline, to estimate K_1 , the plasma to organ transfer constant, which is related to blood flow, k_2 , which is related to transfer of tracer from organ to plasma, and k_3 and the combination model parameter λk_3 , which is proportional to MAO A. λ is defined as K_1/k_2 , and is independent of blood flow. The graphical analyses technique, Logan plot, was generated for determining the distribution volume (DV) for [^{11}C]raclopride.

5.4 Results

5.4.1 Comparison of the arterial and venous radioactivity concentration

A comparison of total carbon-11 in venous and arterial plasma samples vs. time showed that at 5 minutes the venous and arterial values becomes nearly identical (figure 5.4). Thus venous blood samples may be used to obtain the input function beyond 5 minutes. Because of technical difficulties, there were no samples obtained between 1 and 5 minutes.

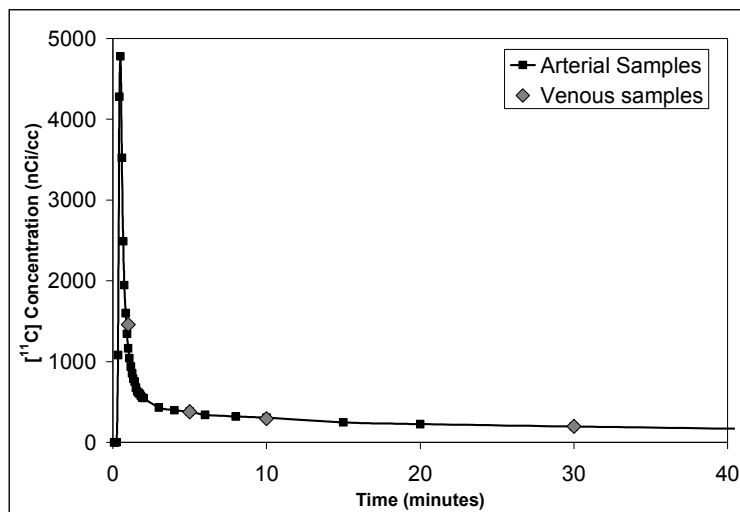


Figure 5.4: Comparison of an arterial TAC with venous radioactivity concentration for $[^{11}\text{C}]\text{raclopride}$ at 1, 5, 10 and 30 minutes.

5.4.2 Comparison of % unchanged radiotracer in arterial and venous plasma samples:

Table 5.1 shows the average percentage difference between arterial and venous metabolite samples for both the radiotracers at various times. The values of percentage difference in the table represent the average of four subjects for $[^{11}\text{C}]\text{clorgyline}$ and five for $[^{11}\text{C}]\text{raclopride}$. The difference in the values between arterial and venous is not significantly different ($p < 0.01$) in this small sample. It seems likely from these preliminary results that it will be possible to substitute venous samples for arterial

samples when doing the kinetic analysis. The graph in figure 5.5 shows arterial and venous % unchanged values for a study using for [^{11}C]raclopride and [^{11}C]clorgyline.

Table 5.1: Average % difference between arterial and venous metabolite samples

	[^{11}C] Clorgyline (n=4)	[^{11}C] Raclopride (n=5)
Time (min)	% Diff Avg	% Diff Avg
1	-0.5	-1.8
5	0.5	-0.5
10	-4.25	-2.6
30	3.75	-0.75

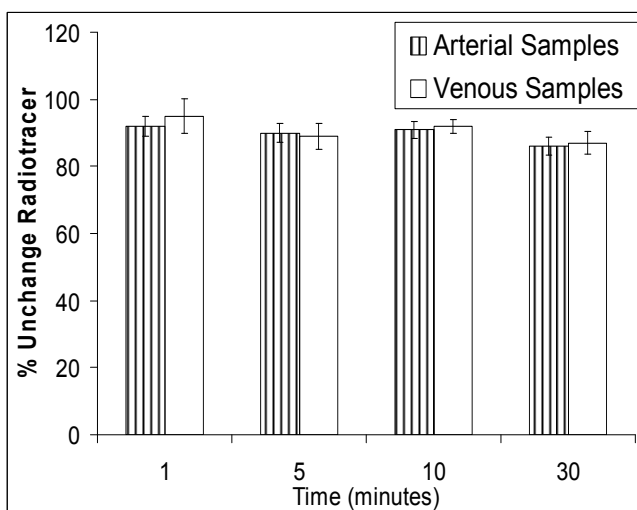
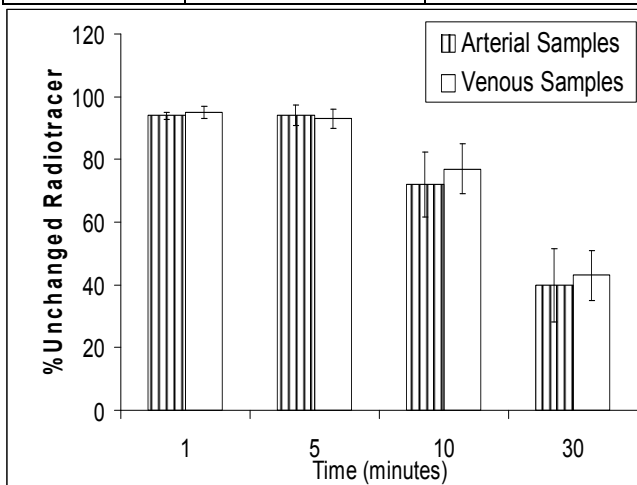


Figure 5.5: The % unchanged radiotracer values of arterial and venous plasma samples for [^{11}C] Clorgyline (top) and [^{11}C] Raclopride (bottom). The observed differences between the two samples are not statistically different ($p=0.01$)

5.4.3 Correction for Partial Volume and Spillover

The recovery coefficients measured experimentally are compared in figure 5.6 with those derived analytically for a set of 3 glass tubes of varying diameters. None of the tubes had a diameter two times the FWHM and hence the radioactivity concentration could not be fully recovered in the ROIs. Shape differences between the experimental points and the analytical curves may result from the approximation of the tomograph PSF by a Gaussian function in the simulation. Highest RC values are obtained for the smallest ROIs. Furthermore, the underestimation of the true radioactivity concentration worsened severely with decreasing tube size. For ROIs of diameter equal to that of the tube, the analytical RC values were estimated to be 0.34, 0.19 and 0.16 for the 6.0, 4.2 and 3.0 tubes, respectively.

The ROI diameter is a user-defined variable; the blood vessel caliber and spatial resolution of the tomograph are fixed. For these human studies, the diameter of the carotid arteries was obtained from the MR images of these subjects. The carotid measured 4 to 5 mm in diameter. The spatial resolution of the tomograph is spatially variant; hence the value for the FWHM was estimated at the position of the blood vessel from the measurements of a line source. As shown in figure 5.7 a, the smaller ROIs produce larger RC values, but at the expense of a greater sensitivity to small variations in the tube diameter. Figure 5.7 b, further illustrates that the choice of the ROI diameter becomes more critical with the PET cameras offering a better spatial resolution, at least for tubes smaller than twice the FWHM of the scanner. The figure also underlines the fact for a given ROI diameter and blood vessel caliber, the magnitude of the partial volume correction is reduced as the spatial resolution of the tomograph improves.

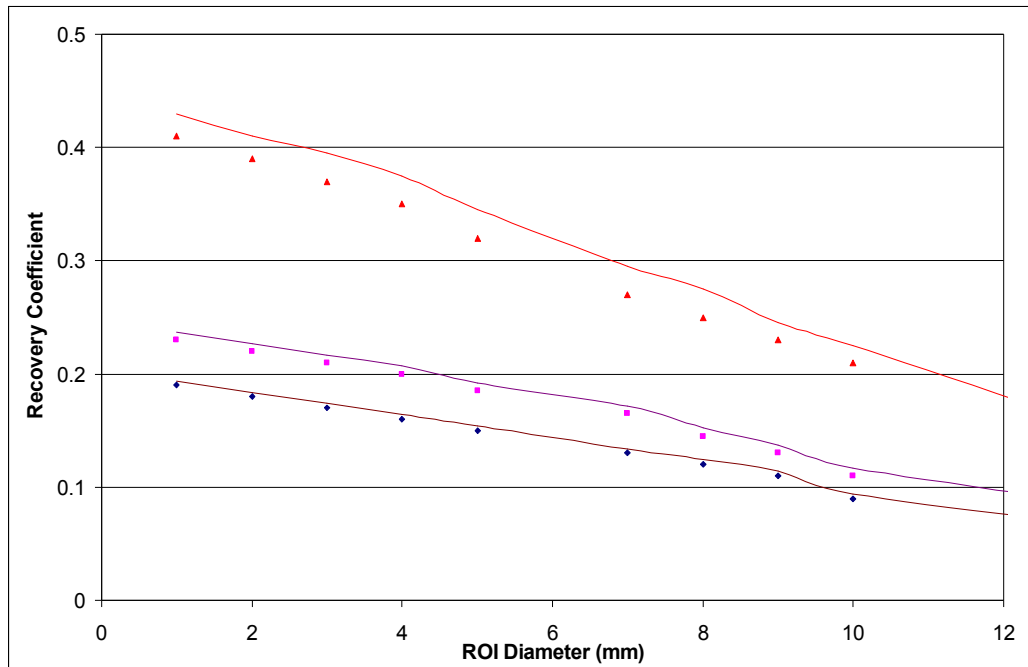
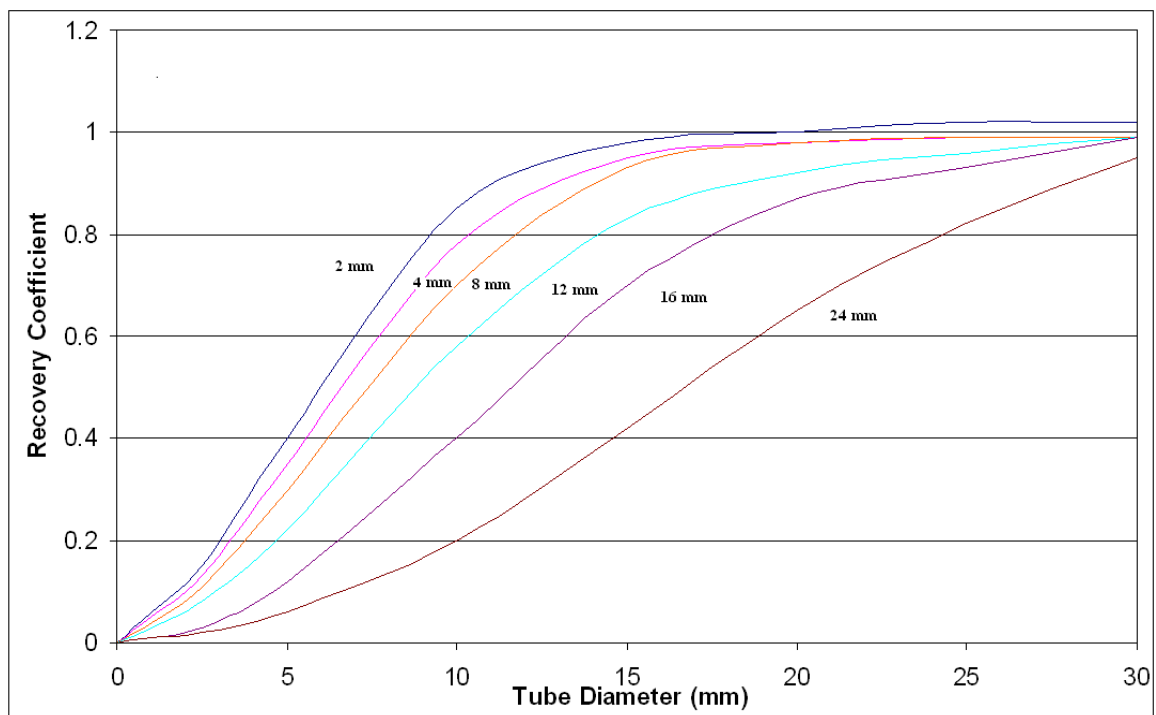


Figure 5.6 Comparison between experimentally measured (symbols) and analytically derived (lines) recovery coefficients for tubes of varying diameters



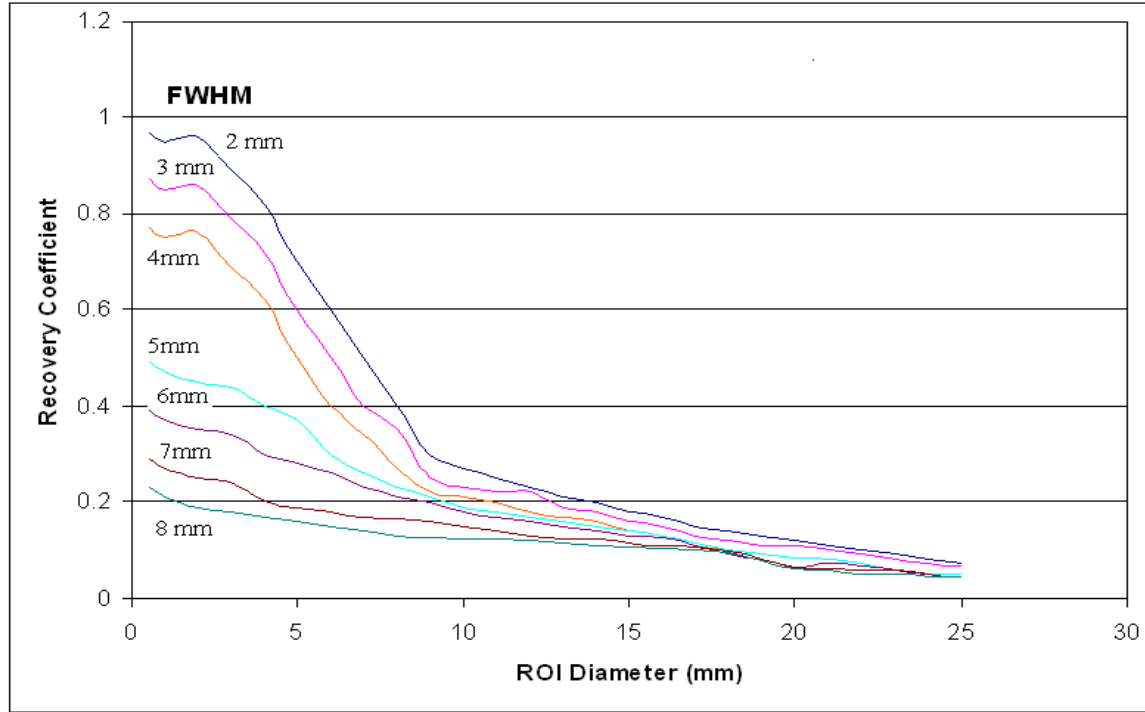


Figure 5.7 a) TOP: Variation in the recovery coefficient with a) the uncertainty in the diameter for the ECAT/HR+ (FWHM 6.8mm), and b) BOTTOM: the choice of the ROI diameter for a tube of 5mm in diameter.

Using MR images of each subject, the size of the artery was estimated and the recovery coefficient was calculated using the Gaussian convolution model. The diameter of the artery ranged from approximately 4.5 mm to 5.6 mm and hence the RC varied from 0.28 to 0.34. The value of $R_{p/wb}$ at one minute was approximately 0.75 for $[^{11}\text{C}]\text{clorgyline}$ and 0.65 for $[^{11}\text{C}]\text{raclopride}$. Table 5.2 shows the value of recovery coefficients of various sizes of the tubes for an ROI of half the diameter of the tube.

Table 5.2. Recovery coefficients of different size tubes for a ROI of half the diameter of the tube.

Vessel Diameter (mm)	3	4.2	6
Simulation	0.22	0.26	0.37
Experimental (tube)	0.21	0.255	0.36

5.4.4 Image derived input function

The TAC for ^{11}C in whole blood consisted of a part containing the peak values of the radioactivity concentration which was extracted from IDIF up to 5 minutes, and the tail which was the concentration as sampled from the venous blood from 5 minutes to the end of the scan. Figure 5.8 shows the carotid artery TAC derived from dynamic brain images and the spillover curve extracted from drawing ROIs around the carotid arteries. The TAC from arterial samples is also shown.

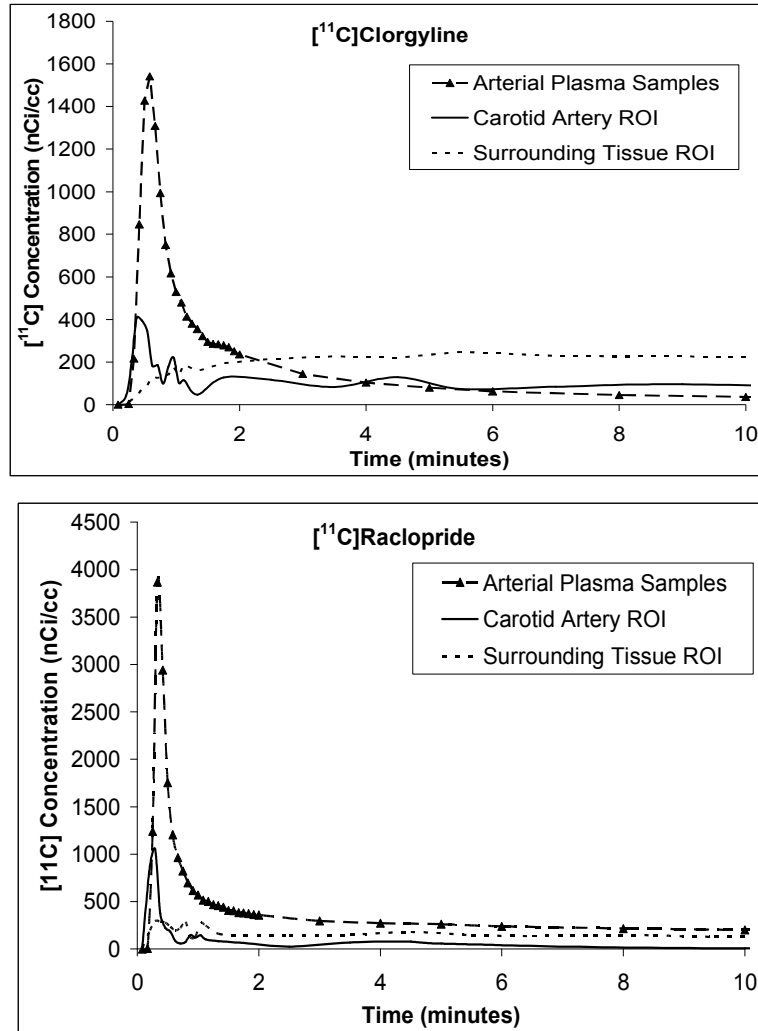
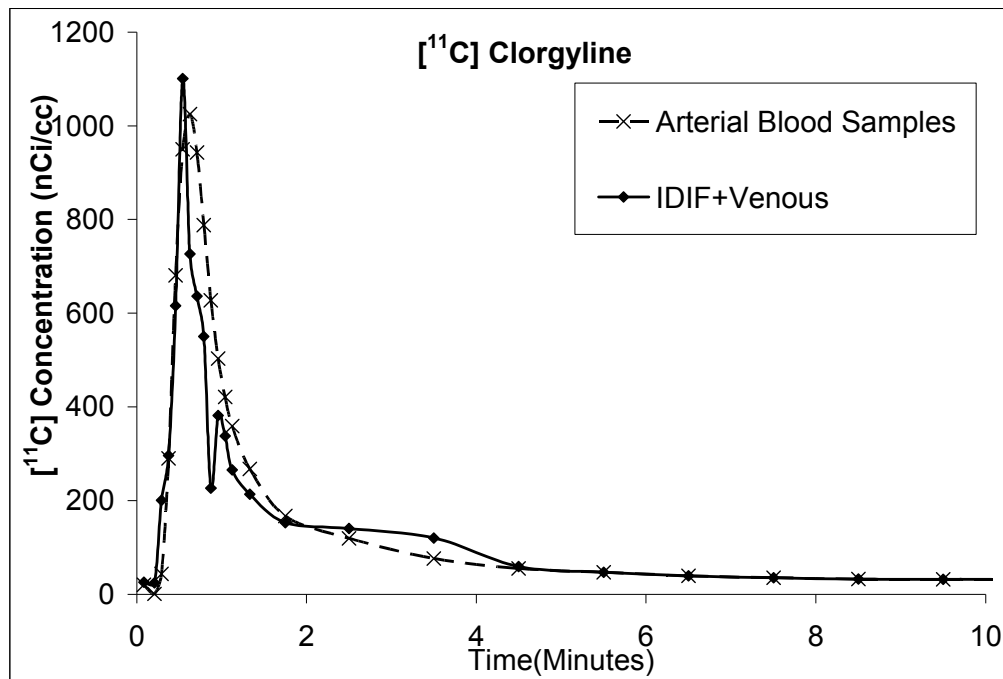


Figure 5.8: Plot shows the TAC obtained from arterial plasma sample(- - -), image derived TAC from the carotid artery ROI without corrections for partial volume spillover and plasma to whole blood ratio(—)and the spillover obtained from drawing ROIs around the carotid artery(. . .) for [^{11}C]clorgyline (top) and [^{11}C]raclopride (bottom)

5.4.5 Direct Comparison of Input functions

TAC corrected using RC values:

Using MR images of each subject the size of the artery was estimated and the recovery coefficient was calculated using the Gaussian convolution model. The diameter of the artery ranged from approximately 4.5 mm to 5.6 mm and hence the RC varied from 0.28 to 0.34. The plasma to whole blood ratio was approximately 0.75 for [^{11}C]clorgyline and 0.65 for [^{11}C]raclopride. The image derived TAC was then corrected for the fraction of parent radiotracer as measured in venous blood samples. Figure 5.9a compares the arterial plasma input function (AIF) to IDIF after accounting for partial volume effects, plasma to whole blood ratio, spillover effects and % unchanged radiotracer. The major correction factor was the partial volume correction. The spillover effect at peak time is very small ([^{11}C]raclopride: $8\% \pm 2\%$ of the total value, [^{11}C]clorgyline: $12.5\% \pm 4\%$ of the total value) and could be ignored.



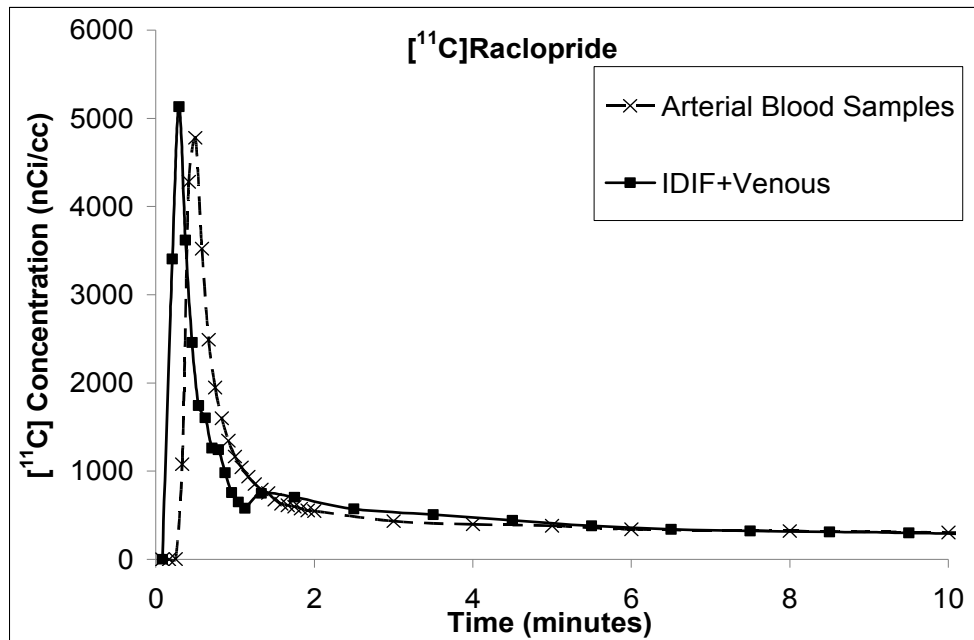


Figure 5.9a Plot compares the image derived TAC after corrections (partial volume effects, plasma to whole blood ratio and % unchanged radiotracer) with the invasive arterial samples for [¹¹C]clorgyline (top) and [¹¹C]raclopride (bottom)

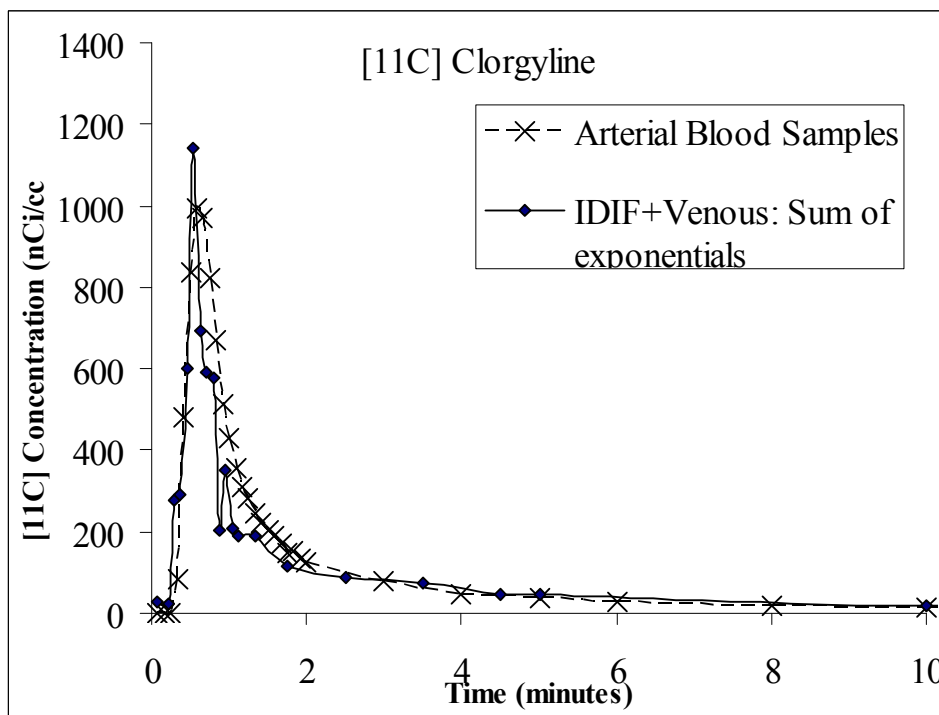


Figure 5.9b: Comparison between the fitted curves (sum of exponential) to the corrected ROI-based blood time-activity curve

The plot shows that the IDIF peaks sooner than the invasive AIF. The IDIF for [^{11}C]clorgyline peaked approximately 15 (+/- 3.5) seconds earlier and [^{11}C]raclopride peaked approximately 12 (+/- 2.5) seconds earlier. Plots in figure 5.10 show the peak heights for both tracers. The peak heights and time to peak for the IDIF and the AIF were significantly different at the 5% significance level. The peak of the AIF is dispersed due to the mechanical sampling of the arterial blood. Thus the AIF, which is assumed to be the gold standard does not accurately capture the time of the peak. The total integral under AIF and IDIF curves was computed. There was no difference between the integral under the AIF and IDIF curves ($p < 0.05$). Figure 5.11 shows a regression plot for the integral under the curve of a [^{11}C]raclopride study.

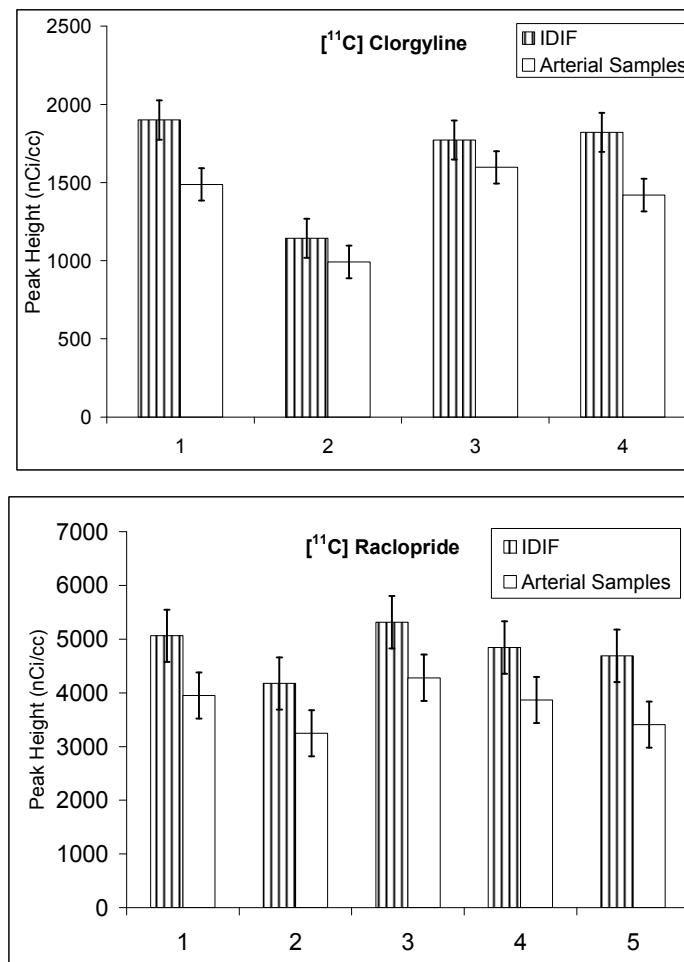


Figure 5.10: Peak differences between IDIF and AIF

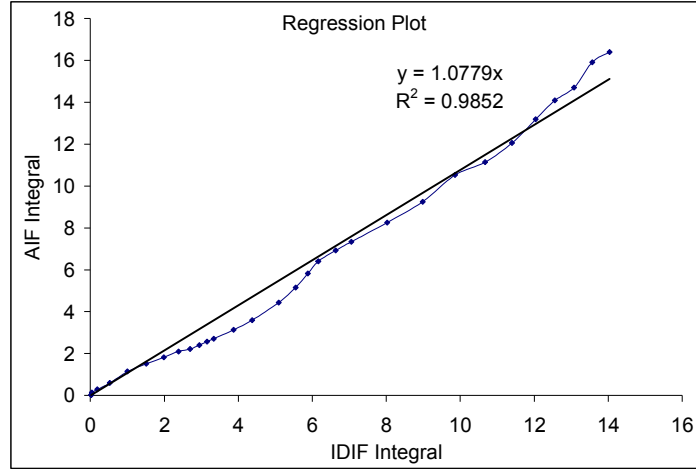


Figure 5.11: Regression Plot for a $[^{11}\text{C}]$ raclopride study comparing the integral under the curve for AIF and IDIF.

Table 5.3: Comparison between the shape of the directly sampled and the corrected ROI-based blood time activity curves for a) $[^{11}\text{C}]$ clorgyline b) $[^{11}\text{C}]$ raclopride

Peak Position ^a (s)	Peak Height ^b (nCi/cc)	Total Area ^b (mCi.s/cc)
a. Clorgyline		
Directly Sampled blood TAC		
34.98	1032	2.1 (± 0.322)
ROI-based blood TAC: Average over several planes		
32.5(-2.48)	1190(+15)	2.9 (± 0.704)
ROI-based blood TAC: Fitted to sum of exponentials		
30.5(-2.)	1150 (+17.2)	2.7(± 0.602)
b. Raclopride		
Directly Sampled blood TAC		
30	4779	7.23 (± 1.01)
ROI-based blood TAC: Average over several planes		
17.5 (-12.5)	4928 (+3)	7.81(± 1.3)
ROI-based blood TAC: Fitted to sum of exponentials		
16.25 (13.75)	5000 (+5)	7.91(± 1.5)

^a Delay (in s) = ROI-based – Directly sampled

^b Difference (in %) = 100 * (ROI-based – Directly sampled)/ Directly sampled

5.4.6 Compartmental models and Graphical Analyses

5.4.6.1 [¹¹C] Clorgyline

For validation of the noninvasive approach, the AIF and IDIF+venous were used for kinetic analysis. The model parameters of thalamus and anterior cingulate for [¹¹C]clorgyline are given in the table 5.4 below.

Table 5.4: Kinetic terms for [¹¹C]clorgyline using the arterial plasma input function and the image derived input function (n=4)

Thalamus		K ₁	λk ₃
IDIF+venous	Arterial Samples (+/- SD)	0.5 (0.07)	0.52 (0.045)
	Average over planes (+/- SD)	0.46 (0.058)	0.47 (0.031)
	Sum of Exponential (+/- SD)	0.42 (0.021)	0.48 (0.014)

Cingulate		K ₁	λk ₃
IDIF+venous	Arterial Samples (+/- SD)	0.43 (0.05)	0.42 (0.042)
	Average over planes (+/- SD)	0.37 (0.045)	0.39 (0.030)
	Sum of Exponentials (+/- SD)	0.38 (0.045)	0.37 (0.030)

K_1 is lower when IDIF is used, because the integral under the curve is higher for the IDIF. The model term k_3 for the AIF and IDIF agree well. λk_3 for IDIF is 7 % lower than the invasive AIF for thalamus and cingulate gyrus. The standard error on k_3 is on the order of 8%.

5.4.6.2 [^{11}C] Raclopride

Logan plots were used to calculate DVs for the caudate, putamen and thalamus regions and these values are shown in table 5.5.

Table 5.5: The Distribution Volumes (DV) for [^{11}C]raclopride using the invasive arterial plasma input function and the image derived input function. ($n=5$)

		IDIF+venous	IDIF+venous
	Arterial Samples	Average over planes	Sum of Exponentials
Thalamus (+/- SD)	0.47 (0.048)	0.50 (0.0378)	0.52 (0.0378)
Caudate (+/- SD)	1.19 (0.0341)	1.23 (0.021)	1.13 (0.021)
Putamen (+/- SD)	1.25 (0.061)	1.30 (0.035)	1.32 (0.035)

A two-tailed paired t-test, for kinetic terms of [^{11}C]clorgyline and [^{11}C]raclopride showed no significant differences ($p=0.05$)

5.5 Discussion

In spite of the need for corrections, the IDIF shows remarkable similarity to the AIF. To summarize, the correction to the image derived TAC involved:

1. Correcting the carotid artery input function using a recovery coefficient for the scanner resolution and size of the artery

2. Subtracting the tissue background activity concentration, obtained from drawing a larger ROI around, from the carotid artery concentration.
3. Scaling this curve to the plasma to whole blood ratio. This is a correction factor for the fraction of radioactivity in whole blood that is from plasma.
4. Correcting the TAC for the % unchanged radiotracer to obtain an input function.

The use of recovery coefficients allows the estimation of the counts lost due to the small size of the internal carotid arteries. However, at longer times, this correction seems to over-estimate the radioactivity concentration and hence use of venous samples from 5 minutes onwards was employed. The kinetic parameters for the combined IDIF were compared to the AIF in the tables 5.4 and 5.5. The parameters compare well except the K_1 values. This difference is attributed to the dispersion of the peak of the AIF; since K_1 depends on peak of the input function. Simulation studies have shown that underestimation of an area under the curve (as is the case with the invasive method compared to the IDIF approach) for the first 20 minutes by 20% to 50% results in 8% to 22% overestimation of K^* values when the graphical analysis (Patlak et al., 1983) in the α - ^{11}C]methyl-tryptophan (α -MTrp) method (Nishizawa et al, 1998) is used.

Another consideration for accurate estimation of an IDIF is to compensate for the underestimation of the peak of the input function from dynamic images, due to the small size of the carotid arteries with respect to the scanner's resolution. Recovery coefficients have been used successfully to correct for partial volume effects. However, an MRI scan was used to estimate the approximate diameter of the internal carotid artery for each subject. The RCs ranged from 0.28 to 0.34 for the 9 subjects studied. In the absence of an MRI scan, an approximate estimate for RC would lead to an error of 13% in the value K_1 .

The approach used here was to measure the peak of the TAC by drawing ROIs on the internal carotid arteries from dynamic PET brain images and to use venous samples to provide a good fit to the input function beyond 5 minutes as well as to analyze for the fraction of parent radiotracer. There were a few important observations from the image

derived input functions. In all subjects, the TAC from the arterial plasma samples lagged behind the TAC from the carotid artery images (figure 5.12). A temporary increase in radioactivity in the image derived TAC at about 1.5 minutes was observed which can be attributed to recirculation. This feature was missing in the AIF as the dispersion in the on line sampling of arterial blood samples is so great that it causes a delay of the peak and masks the recirculation of the radiotracer. An overestimation of the tail of the IDIF was also observed. This observation is due to the spillover from the surrounding tissue which accumulates ^{11}C with time. This may be due to the overestimation of the scaling factors and localization of the radiotracer. Since venous samples will be used past 5 minutes for the two tracers, this is not a concern. There were no samples obtained between 1 and 5 minutes and hence a time point before 5 minutes cannot be used. Also as illustrated in figure 5.9b, the sum of exponentials approximated the peak, shoulder and tail closely; however the fitted curves were dependent on the initial values.

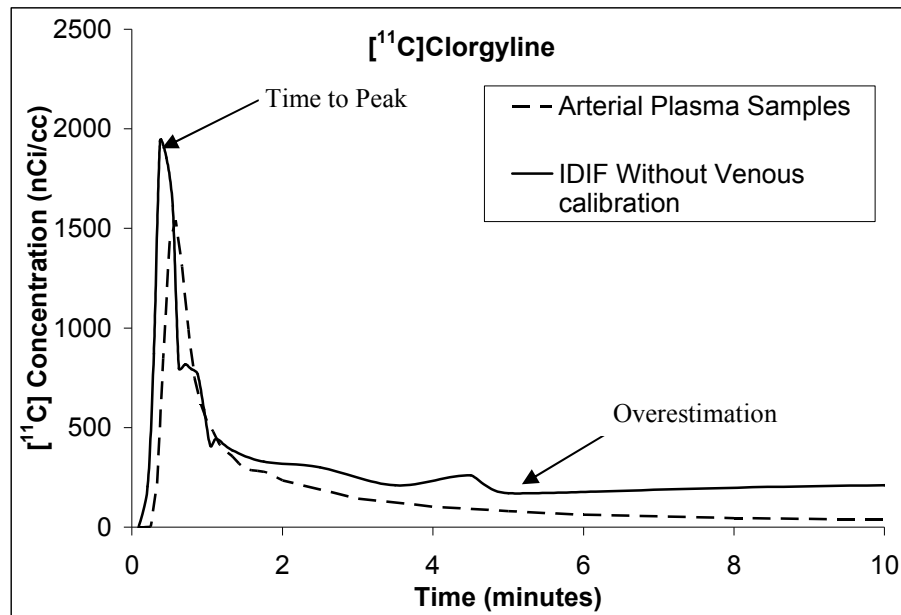


Figure 5.12: Plot shows the early peak time and overestimation for $[^{11}\text{C}]$ clorgyline, indicating the danger of using carotid artery ROI past 5 minutes.

It was also shown that in the absence of arterial blood samples, venous samples can be used for determination of the fraction of the parent radiotracer for $[^{11}\text{C}]$ clorgyline and $[^{11}\text{C}]$ raclopride. This makes intuitive sense since the metabolism is relatively slow in

comparison to circulation times. A direct comparison between the percent unchanged tracer for these two radiotracers showed there was no significant difference between the fraction of unchanged radiotracer in arterial and venous blood. Note that these preliminary data represent only two radiotracers, [^{11}C]clorgyline and [^{11}C]raclopride. Because all tracers behave differently in a biologic environment, this has to be ensured for any other tracer.

5.6 Conclusion

This chapter demonstrated that less invasive estimation of the input function (obtained using IDIF for the first five minutes + venous samples past five minutes) is possible using an equation that corrects for partial volume equation for IDIF derived from carotid artery for [^{11}C]clorgyline and [^{11}C]raclopride and venous samples for % unchanged radiotracer. For these radiotracers arterial and venous are the same after 5 min, making it appropriate to substitute invasive arterial samples with the less invasive venous samples. Venous samples also allow metabolite correction which is needed for quantification of most radiotracers. Even though IDIF peaks earlier and is larger, no statistically significant differences were observed for integral under the curve and kinetic parameters. However, the IDIF gives a different; perhaps more accurate estimate of K_1 , as it is free from dispersion and delay errors. Anatomical images of the subjects made a simple Gaussian simulation feasible to individually correct for partial volume effects. The spillover from surrounding tissue was small over the first 5 minutes and thus the IDIF could be used for the first 5 minutes after which venous samples will be used for the remainder of the study.

Chapter 6

Comparison of Methods Studies

It has been the aim of this thesis to use dynamic brain images for the estimation of a whole blood time TAC. This curve is then corrected for the presence of metabolites of authentic radiotracer to obtain an input function. Figure 6.1 is an illustration of this process. This chapter relates the three methods studied for determining the input function, in terms of their similarities, differences and constraints

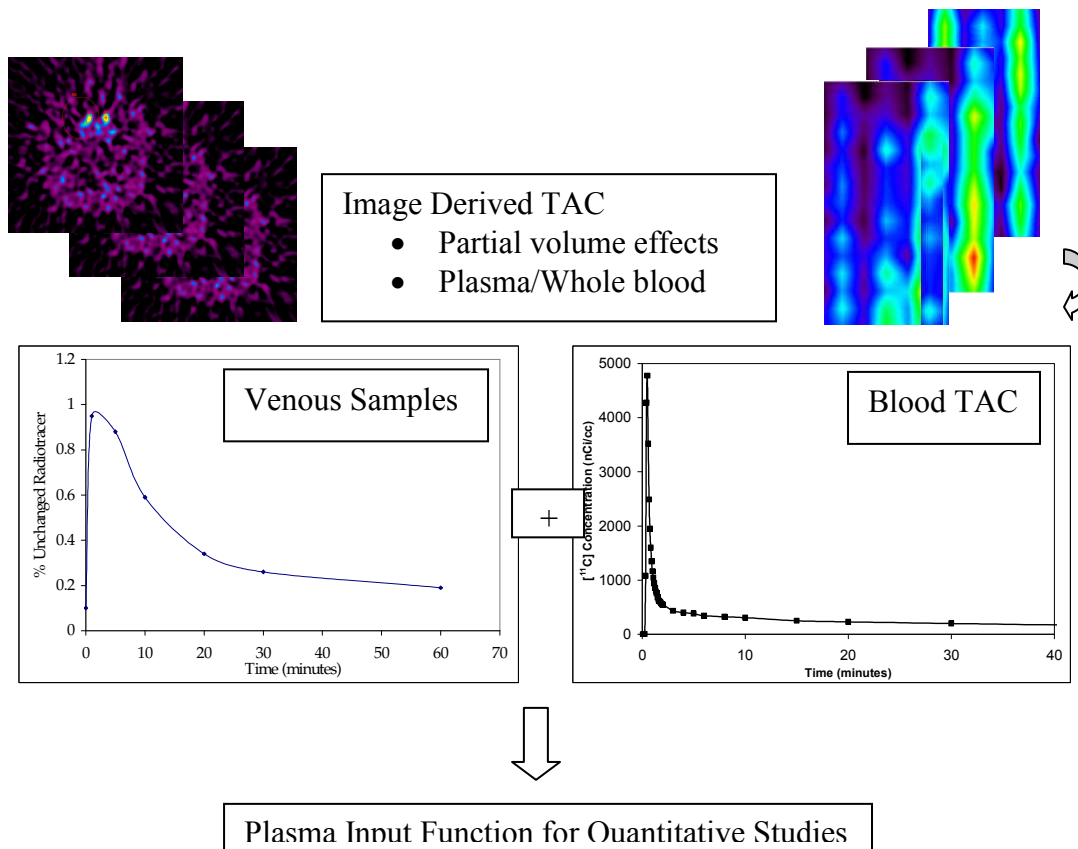


Figure 6.1: Process of obtaining an input function

6.1 Data Acquisition Consideration for Compartmental Modeling

Compartmental modeling and tracer kinetic analysis require the acquisition of two sets of data, the radioactivity time courses in blood and tissue, to yield estimates of

physiologic parameters. It is very obvious that the quality of the PET data directly affects the reliability of the estimated model parameters. The radioactivity concentration extracted from blood pools in dynamic PET images corresponds to the time course of total radioactivity in whole blood. This TAC can be used as an input function for kinetic analyses only for tracers that are exchanged rapidly and distributed equally in plasma and erythrocytes, as is approximately the case for 1-[¹⁸F] fluoro-2-deoxy-D-glucose (FDG) (Chen, 1998). However, radiotracers that either equilibrate slowly between blood components and/or are actively concentrated by or excluded from erythrocytes require that the radioactivity concentration measured in whole blood be transformed into the radioactivity concentration in plasma. The PET study must then be supplemented by blood samples that are drawn at discrete times and centrifuged in order to measure the radioactivity in plasma. If, in addition, the radiotracer is metabolized in peripheral tissue, blood sampling cannot be avoided regardless of the kinetics of equilibration of the radiotracer in whole blood. More blood samples are drawn and assayed biochemically in order to determine the contribution of the various radiolabeled compounds to the measured radioactivity in plasma. As seen in the preceding chapters, the processing of these blood samples typically involves multiple steps, thereby making the procedure time consuming and the measurements prone to noise. Only a few blood samples can thus be analyzed for each PET study and one typically has recourse to exponential and/or polynomial functions in order to interpolate between and extrapolate from these data points.

The total radioactivity concentration in whole blood is usually corrected in two independent steps, first to yield the total radioactivity concentration in plasma, and second to obtain the parent radiotracer concentration in plasma. For both these corrections, the use of venous plasma samples has been proposed for extrapolation of the incomplete blood data over the duration of the PET study. The possibility of reducing the number of samples taken from a subject is tested. These samples are invasive, less in comparison to arterial samples. Chapter 5 has shown validation of the use of these samples, hence making the use of IDIF complete. However, it should be noted that this is shown only for the use of ¹¹C tracers, [¹¹C]raclopride and [¹¹C]clorgyline

The **peak** of the input function was estimated from dynamic images. Three PET imaging systems were used for this purpose. The result of each is compared in terms of feasibility, errors and constraints are compared.

Table 6.1 Comparison of advantages and disadvantages of methods related to this thesis

	Advantages	Limitations
Invasive Arterial sampling	Good timing resolution Does not require corrections based on scanner characteristics	Invasive Delay and dispersion Technical difficulties
Wrist Scanner (+Venous samples)	Non-invasive Independent timing resolution. Venous catheter placement is easy Portable and stand alone scanner Less tissue attenuation	Partial volume effects Calibration needed Requires good enough sensitivity Whole blood TACs only Requires shielding
Dynamic Brain Images (+Venous samples)	Good timing resolution Non-invasive. Venous catheter placement is easy No extra hardware required, hence most economically feasible	Partial volume effects Whole blood TACs only (need an MRI scan for each subject to estimate the artery size) Needs a major blood vessel in the field of view

6.2 Comparing the MicroPET scanner and Wrist Scanner

6.2.1 Considerations for a full ring tomograph

Transitioning from planar detector to a full ring system will introduce factors that affect image quality and radioactivity quantification. One factor is the parallax error, which is often the **dominant error** for such high-resolution systems. It degrades the image resolution caused by the penetration of the photons into crystals. In detectors that lack depth of interaction measurements, the depth at which the photon was stopped cannot be easily established, leading to the association of the event with an incorrect LOR when the photons enter the crystal at an oblique angle. Resolution gets worse as the source is moved closer to the edges of the FOV. Hence, the parallax error becomes significant if the object fills the FOV of the scanner, as is the case with the wrist scanner. It is also observed that the tangential resolution increases with radius faster than radial resolution,

in contrast to what is expected from parallax. This could be related to the trapezoidal shape of the coincidence aperture function between opposite detectors when away from the center.

6.2.2 Full Ring Wrist Tomograph: Monte Carlo Simulations

A full ring tomograph, with a 2.6 mm resolution was able to distinguish between the wrist arteries and veins. A simple recovery coefficient enabled the correction for partial volume effects, the main concern for extracting a blood TAC from dynamic images. This section reports on the Monte Carlo simulation studies for a 16 detectors, 7.5 cm diameter full ring tomograph. Simulation of a PET system was first validated by comparing system sensitivity, between simulated and real results for the 4 detector prototype.

The Monte Carlo toolkit GATE (Jan, 2003) based on GEANT4 is dedicated to nuclear medicine emission tomography simulations and has been successfully used to model different emission tomographs, in particular PET systems (Rey 2003, Rannou 2004, Jan 2005). GATE includes the possibility of precisely describing the detector geometry, explicitly modeling radioactive emissions and dead-time effects and handling of output data as signal pulses in the same versatile way as data processing in detectors.

GATE simulates generation, tracking and annihilation of positrons. The range of the positron is simulated as well as the γ – γ non-collinearity. In GATE simulations, two types of sources were considered: an '¹⁸F source' simulating all the physical processes involved during emission and interaction of positrons and a 'back-to-back source' with two 511 keV gammas directly emitted at 180° from one another. Photoelectric effect, Compton and Rayleigh interactions of the photons in the phantom, air, inner cap, shielding and detectors are modeled with a realistic description of geometry and materials of the system. The position of each event is calculated using an energy-weighted centroid calculation of the positions of the successive energy deposits by interactions of photons in crystals. Figure 6.2 illustrates the different steps of the simulation of the Wrist Scanner system using GATE. A 20 ns coincidence window was used to collect

coincidence events. A non-paralysable dead time for both prompt and delayed events was used to simulate events lost by the data processing unit. Each LOR was recorded as a pair of photons with associated crystal position and energy in a list-mode format. Coincidence pairs were re-arranged in list-mode format or sinograms as needed.

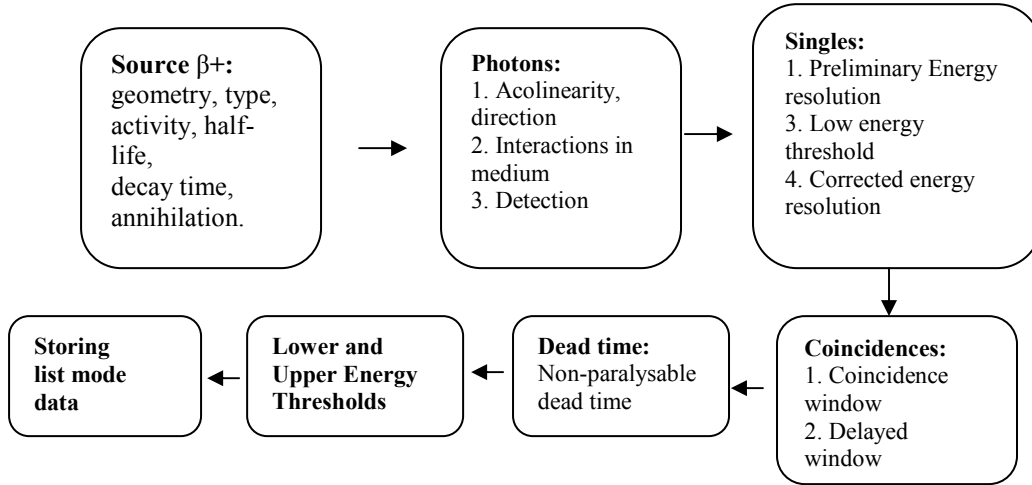


Figure 6.2: Simulation Design

System sensitivity

Measurements and simulations of absolute system sensitivity were performed for the 4 detector using a ^{68}Ge point source (2 mm inner diameter and 1 mm wall thickness) of 0.5 mCi. It was positioned in the centre of the field of view of the scanner. Sensitivity was defined as the ratio of the number of detected true coincidence events over the number of positron emitting decays from the source during the acquisition time. Acquisition was performed for lower energy thresholds set to 250 and a fixed upper energy threshold of 650 keV. The measured sensitivity for the 4 ring detector was 0.2% and that for the simulated four detector prototype was 0.12%. This difference may be because the threshold on each channel could not be adjusted. The fact that the low threshold will cause channels with higher gain to detect a number of scattered photons gives a higher sensitivity for the Wrist Scanner. Table 6.2 shows simulated sensitivities of the 16 ring tomograph system for a point source located at the centre of the FOV as a function of the lower energy threshold.

Table 6.2 Simulated estimates of the Wrist Tomograph Sensitivity

Energy Window (keV)	Simulated Sensitivity (%)
150-650	0.32
250-650	0.27
350-650	0.26

Spatial resolution

For the wrist tomograph, the spatial resolution was compared in the axial, radial and tangential directions for simulated data at different positions in the FOV. This was then compared to the MicroPET R4 resolution. All measurements were carried out with an energy window set to 250–650 keV. For transverse resolution measurements, the point source was placed in different radial distances in the horizontal as well as in the vertical directions.

Table 6.3: Simulated resolution of the Wrist Tomograph compared with measured simulations of the MicroPET

Spatial Resolution FWHM(mm)	MicroPET (measured)	Wrist Tomograph (simulated)
Radial	1.8	1.79
Tangential	1.9	1.78
Axial	1.85	2.1

A comparison between MicroPET and the 16 detector Wrist Tomograph is shown in the table 6.4

Table 6.4: Comparison between important parameters of the MicroPET and Wrist Scanner

	MicroPET R4	Wrist Scanner
Ring Diameter	172 mm	75 mm
FOV Transaxial	112 mm	70 mm
FOV Axial	78 mm	20 mm
Sensitivity (250 keV)	2.25	1.89
Spatial Resolution	1.9 mm	1.7 mm

6.3 Error estimates in Kinetic Parameters

The reason for acquiring tomographic dynamic images of the wrist was multifold: to assess the expected problems of partial volume effects and sensitivity. This was necessary as it will be a concern for the wrist scanner; 4 or 16 detectors. The technique of IDIF adds another loss of signal which is due to partial volume effects and it was necessary to evaluate this effect as it would cause additional noise due to low count rate and thus increase the noise level and decrease signal strength. If the interval is to be lengthened, then the noise would be reduced, however then there is a possibility that the peak of the curve might get distorted.

The TAC from MicroPET acquisitions was used to estimate the error caused due to the sensitivity of the wrist scanner. The wrist scanner sensitivity of 4cps/nCi/cc was multiplied to its time interval to convert it to counts. With knowing the number of counts, noise error statistics can be done onto the count number using the following equation:

$$\%Error = \frac{1}{\sqrt{Counts}} \quad (6.1)$$

This error is next applied to the activity level (nCi/cc) to predict the possible standard deviation seen by the detector. The detector will give counts to calculate activity (in cps), while in this case, the activity (in cps) is used to calculate the number of counts and its error all based on the sensitivity levels and partial volume enhancements

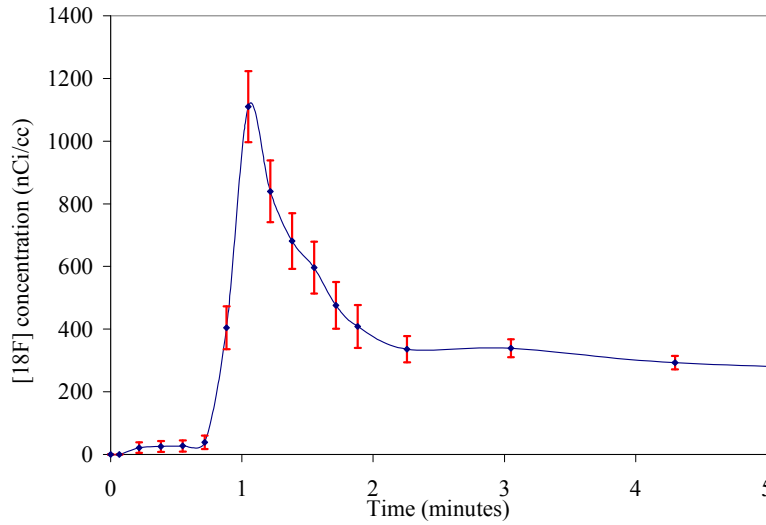


Figure 6.3: Estimated error bars for the sensitivity and partial volume effects for the 4 detector prototype.

Similarly, for a full ring scanner, the simulated sensitivity of 1.89 % was used to estimate the error bars and is shown in figure 6.4

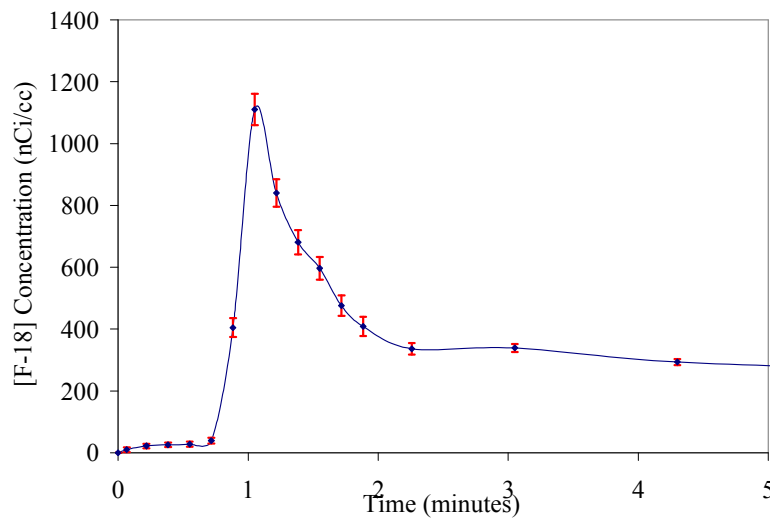


Figure 6.4: Estimated error bars for the sensitivity and partial volume effects for the 16 detector full ring tomograph.

The TAC from a MicroPET study and the error from the wrist scanner **was** used to calculate 4 simulated input functions were calculated. This was used for the calculation of the CMRglu. Table 6.5 shows these values for the 4 detector prototype, full ring wrist tomograph, the MicroPET scanner with the ‘gold standard’ value.

Table 6.5: Comparison CMRglu values for Arterial samples, MicroPET and simulated input functions for the Wrist Scanner.

	Arterial Samples	MicroPET	Wrist Tomograph (16 detectors)	4 Detector Wrist Scanner
CMRglu	63.16	59.28	60.16	71.37
STD DEV	4.46	7.369	7.05	10.64

It shows that when having a higher noise value like that of the 4 detector blood curves gives the CMRglu a higher variation in error; the error was significantly increased and CMRglu was overestimated. Hence, less ambiguity of the input function resulted in more precise calculations of the kinetic errors. Essentially, longer time intervals of count rates produced less noise but at the same time there is a threat of losing important peak features.

Therefore, shorter time intervals are required, but these would also include statistical uncertainties. This uncertainty could be reduced with a higher count rate since higher count rates give a better signal to noise ratio. This comes back to underlining the fact that the sensitivity be high enough to detect low levels of activity.

6.4 Internal and External Dispersion

The errors discussed above are solely due to the sensitivity and partial volume effects as dispersion, internal or external, has not been considered so far. The wrist

scanner has an inherent independent nature from external dispersion or from a PET scanner. It is possible to see this dispersion using the IDIF data from internal carotid arteries.

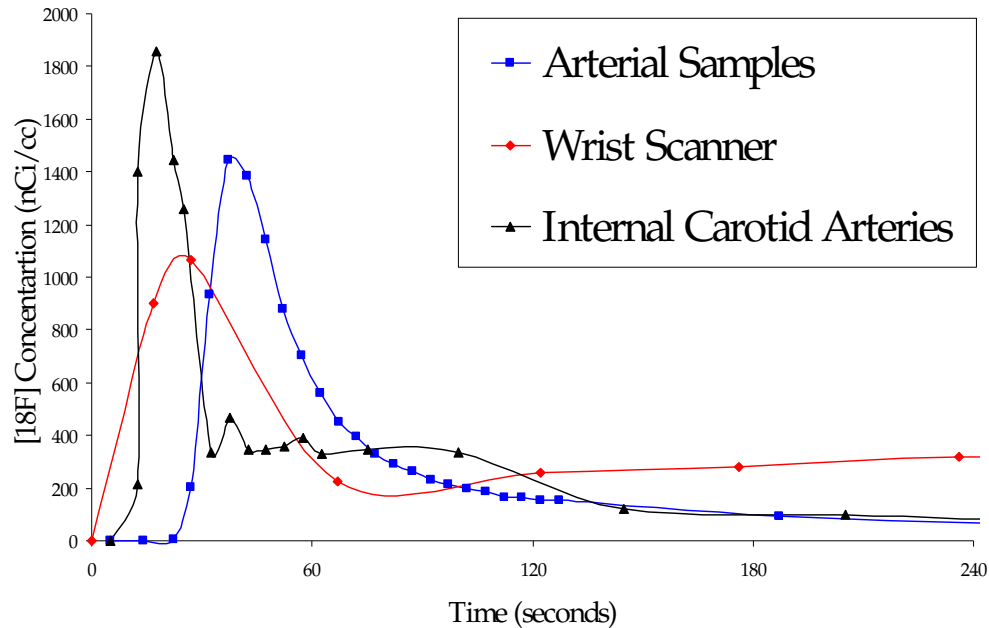


Figure 6.5: Temporal differences in the peak of the input functions

There will be some internal dispersion occurring between the neck (carotid artery) and the wrist arteries. In contrast, for an invasive method, external dispersion also factors in on the calculation and for the MicroPET, portability and adjustments become an issue. The wrist scanner's independence from a PET scanner gives it its own timing resolution. Therefore, the wrist scanner can be used to sample the blood non-invasively and derive an accurate input function, after correction for internal dispersion between the carotids and wrist arteries. An ad hoc model for the two arteries transfer function could be derived, following appropriate corrections for delay and dispersion of the measured arterial blood.

6. 5 Methods of extracting the peak of an input function

The essential step in the generation of the image-derived input function is the localization of the blood vessel component(s) from dynamics of the tracer in the vascular

space. Manual drawing of a blood vessel region of interest (ROI) around the wrist arteries and a vascular ROI was defined on the co-registered high resolution MRI data for the internal carotid arteries was used for this thesis. A number of statistical procedures have also been proposed to identify blood vessel ROI data over the space of the PET image using temporal tracer kinetic information, including cluster analysis (Liptrot, 2004), dynamic factor analysis (Wu 1996, Wu 1995) and independent component analysis (Lee 2001, Naganawa 2005).

6.5.1 Independent Component Analysis

Independent component analysis (ICA) was first introduced to the neuroimaging field for the study of brain function using functional MRI (fMRI) data (McKeown, 1998) and a number of successful fMRI-ICA studies have appeared. In the study by Lee *et al*, ICA was applied to Oxygen-15 water cardiac PET data. The ICA generated input function has a tail with reduced noise as compared to that obtained by arterial blood sampling, while the estimates of myocardial blood flow are comparable. Because the left ventricle is relatively large and clearly separated from the myocardial wall it was not necessary in that study to consider effects due to partial volume and spillover. Incorporating specific properties of the PET data, a special version of ICA, Extraction of plasma TAC using ICA (EPICA), was introduced by Naganawa *et al*, (2003, 2005). As the sizes of the blood vessels in the brain are small relative to the image resolution, effects of partial volume can not be safely ignored. Hence EPICA used a single arterial blood sample to scale the ICA generated image-derived input function, and effects of spillover are implicitly accounted for through the source signal mixing process. Chen *et al* used FMRLAB and proposed the use of the Infomax ICA algorithm as a way to automate the localization of both the blood vessel ROI and the surrounding tissue ROI. The equation used by them is of the form explained in Chapter 4, where partial volume and spillover effects are defined by recovery coefficients. For the human wrist and brain images EPICA was implemented and the correction was done using a recovery coefficient

The basic idea of Independent Component Analysis is to take a set of observations and to attempt to find a set of independent components that explain the data. The origins of this method are in the so-called “cocktail party problem” (Appendix B shows details of the motivation and basic principle of ICA)

As presented in Hyvärinen and Oja (1999), Independent Component Analysis starts with a vector of observations,

$$\mathbf{x} = (x_1, \dots, x_n) \quad (6.2)$$

The basic assumption here is that each of these observations can be derived from a set of n independent components:

$$x_i = a_{i1}s_1 + \dots + a_{in}s_n$$

or, using a matrix notation,

$$\mathbf{x} = \mathbf{A}\mathbf{s}. \quad (6.3)$$

Generally, bold lower case letters indicate vectors and bold upper-case letters denote matrices. Here $\mathbf{s} = (s_1, \dots, s_n)$ is a random vector the latent variables, or independent components and \mathbf{A} is a $m \times n$ mixing matrix. The task is to find both \mathbf{s} and \mathbf{A} . The basic assumption in ICA is that the components s_i are independent of each other: that is,

$$P(s_i, s_j) = P(s_i)P(s_j). \quad (6.4)$$

Further, the distributions of s_i can be assumed to be unknown, except that they may not be normal. If the data is composed of more than one normally distributed **components** ICA is impossible. **There are two limitations in ICA.** First, it is impossible to determine the variances of the independent components. This is because both \mathbf{A} and \mathbf{s} are unknown: the variance of s_i can be changed at will by adjusting the corresponding column of \mathbf{A} appropriately. Second, because both \mathbf{A} and \mathbf{s} are unknown, the order of the independent components cannot be determined: it is possible to change the order of one of these, if the other is changed to match. Furthermore, as the variances cannot be determined there is no obvious yardstick for determining the relative importance of the different components.

6.5.2 Preprocessing of data

Before applying an ICA algorithm on the data, some preprocessing is usually needed.

Centering

The most basic and necessary preprocessing is to center \mathbf{x} , i.e. subtract its mean vector $\mathbf{m} = E\{\mathbf{x}\}$ so as to make \mathbf{x} a zero-mean variable. This implies that \mathbf{s} is zero-mean as well, as can be seen by taking expectations on both sides of equation 6.3. This preprocessing is made solely to simplify the ICA algorithms. After estimating the mixing matrix \mathbf{A} with centered data, the estimation is completed by adding the mean vector of \mathbf{s} back to the centered estimates of \mathbf{s} . The mean vector of \mathbf{s} is given by $\mathbf{A}^{-1}\mathbf{m}$, where \mathbf{m} is the mean that was subtracted in the preprocessing.

Whitening

Another useful preprocessing strategy in ICA is to first whiten the observed variables. This means that before the application of the ICA algorithm (and after centering), the observed vector \mathbf{x} is transformed linearly so that a new vector $\tilde{\mathbf{x}}$ is obtained which is white, i.e. its components are uncorrelated and their variances equal unity. In other words, the covariance matrix of $\tilde{\mathbf{x}}$ equals the identity matrix:

$$E\{\tilde{\mathbf{x}} \tilde{\mathbf{x}}^T\} = \mathbf{I}. \quad (6.5)$$

One popular method for whitening is to use the eigen-value decomposition (SVD) of the covariance matrix $E\{\mathbf{xx}^T\} = \mathbf{E}\mathbf{D}\mathbf{E}^T$, where \mathbf{E} is the orthogonal matrix of eigenvectors of $E\{\mathbf{xx}^T\}$ and \mathbf{D} is the diagonal matrix of its eigen values, $\mathbf{D} = \text{diag}(d_1, \dots, d_n)$. $E\{\mathbf{xx}^T\}$ can be estimated in a standard way from the available sample $\mathbf{x}(1), \dots, \mathbf{x}(T)$. Whitening can now be done by

$$\tilde{\mathbf{x}} = \mathbf{E}\mathbf{D}^{-1/2}\mathbf{E}^T \mathbf{x} \quad (6.6)$$

where the matrix $\mathbf{D}^{-1/2}$ is computed by a simple component-wise operation as $\mathbf{D}^{-1/2} = \text{diag}(d_1^{-1/2}, \dots, d_n^{-1/2})$. $E\{\tilde{\mathbf{x}} \tilde{\mathbf{x}}^T\} = \mathbf{I}$, can be checked.

Whitening transforms the mixing matrix into a new one, \tilde{A} . We have from (6.3) and (6.6):

$$\tilde{x} = \mathbf{E}\mathbf{D}^{-1/2}\mathbf{E}^T\mathbf{A}\mathbf{s} = \tilde{A}\mathbf{s} \quad (6.7)$$

The utility of whitening resides in the fact that the new mixing matrix \tilde{A} is orthogonal.

This can be seen from

$$E\{\tilde{x}\tilde{x}^T\} = \tilde{A}E\{\mathbf{s}\mathbf{s}^T\}^T = \tilde{A}\tilde{A}^T = \mathbf{I}. \quad (6.8)$$

Process of whitening also reduces the number of parameters to be estimated. Instead of having to estimate the n^2 parameters that are the elements of the original matrix \mathbf{A} , the new, orthogonal mixing matrix \tilde{A} needs to be estimated. An orthogonal matrix contains $n(n-1)/2$ degrees of freedom. For example, in two dimensions, an orthogonal transformation is determined by a single angle parameter. In larger dimensions, an orthogonal matrix contains only about half of the number of parameters of an arbitrary matrix. Thus one can say that whitening solves half of the problem of ICA. Because whitening is a very simple and standard procedure, much simpler than any ICA algorithms, it is a good idea to reduce the complexity of the problem this way. It may also be quite useful to reduce the dimension of the data at the same time as we do the whitening. The Eigen values d_j of $E\{\mathbf{x}\mathbf{x}^T\}$ which are too small can be discarded, as is often done in the statistical technique of principal component analysis. This has often the effect of reducing noise. Moreover, dimension reduction prevents over-learning, which can sometimes be observed in ICA (Hyvärinen et al., 1999).

6.5.3 Fast ICA

The FastICA algorithm, as presented by Hyvärinen and Oja (1999), starts with a proposed weight vector \mathbf{w} . The task is to find a direction for \mathbf{w} so that the projection $\mathbf{w}^T\mathbf{x}$ maximizes the non-normality, as measured by the negentropy $J(\mathbf{w}^T\mathbf{x})$. The variance of $\mathbf{w}^T\mathbf{x}$ — and, as the data has already been whitened and centered as a preprocessing step, the norm of \mathbf{w} is constrained to unity.

The FastICA is based on a fixed-point iteration scheme for finding a maximum of the non-gaussianity of $\mathbf{w}^T \mathbf{x}$, as measured in (Hyvärinen and Oja, 1997; Hyvärinen, 1999a). It can be also derived as an approximate Newton iteration (Hyvärinen, 1999a). Denote by g the derivative of the non-quadratic cost function G and the derivatives of the functions

$$\begin{aligned} g_1(u) &= \tanh(a^1 u), \\ g_2(u) &= u \exp(-u^2/2) \end{aligned} \quad (6.9)$$

where $1 \leq a^1 \leq 2$ is some suitable constant, often taken as $a^1 = 1$.

The algorithm for finding one independent component is as follows:

1. Choose an initial weight vector \mathbf{w}
2. Let $\mathbf{w}^+ = E\{\mathbf{x}g(\mathbf{w}^T \mathbf{x})\} - E\{g_0(\mathbf{w}^T \mathbf{x})\}\mathbf{w}$
3. Let $\mathbf{w} = \mathbf{w}^+ / \|\mathbf{w}^+\|$
4. If not converged, go back to 2

Convergence in step 4 means that the old and new values of \mathbf{w} point in the same direction that is, $\mathbf{w}_{\text{old}} \cdot \mathbf{w} = 1$. The algorithm presented above computes only one of the independent components; **to get all it is necessary** to repeat the process. This can be done in parallel, with different weight vectors; however, $\mathbf{w}_1^T \mathbf{x}, \dots, \mathbf{w}_n^T \mathbf{x}$ have to be decorrelated after every iteration, to prevent the different vectors from converging to the same maxima. Hyvärinen and Oja (1999) present a couple of different ways to accomplish this, and is taken care in EPICA algorithm

6.5.4 Application of EPICA to Dynamic Wrist Images

The value of the q th voxel of the PET image at time, t , is described by

$$x(q,t) = s_p(q)c_p(t) + s_t(q)c_t(t) \quad (q=1, \dots, Q) \quad (6.10)$$

where Q is the total number of voxels, $s_p(q)$ is determined by the ratio of the tissue blood volume to the q th voxel, $s_t(q)$ is determined by the scale of the t TAC values and the ratio of the brain tissue to the q th voxel, and $c_p(t)$ and $c_t(t)$ are the p TAC and the t TAC,

respectively. The history of the concentration of FDG at the q th voxel, $x(q)$, can be represented by

$$x(q) = s_p(q)c_p + s_t(q)c_t \quad (6.10)$$

where $x(q)$, c_p and c_t are column vectors. In matrix notation, can be represented as

$$X = [c_p \ c_t] [s_p \ s_t] = CS \quad (6.11)$$

Here, X , is the dynamic PET image matrix, and s_p and s_t are the blood volume image and the tissue image, respectively.

As seen in section 6.5.1, C and S are regarded as the mixing matrix and the source matrix the ICA model, respectively. The dynamic PET image sequence is assumed to be a linear combination of spatially independent images, namely the blood volume image and the tissue image. The pTAC is a column of the mixing matrix. Note that independence is not assumed in time-activity curves (TACs), but in their spatial distributions.

Procedure of EPICA

The EPICA procedure is summarized below. (Naganawa, 2005)

Step 1) Append negative images to achieve the zero-mean source signal that the ICA algorithm requires.

Step 2) Standardize each voxel's TAC by the time integral to emphasize pTAC-related information.

Step 3) To obtain a stable estimation, reduce the dimension of the dynamic PET image sequence to two using principal component analysis (PCA).

Step 4) Apply FastICA (a deflation approach) to the dynamic PET images.

After the curve is estimated it is scaled using recovery coefficients as previously used for the IDIF extracted using ROIs

6.5.5. ICA vs. ROI analysis

Figure 6.6 below shows a ROI IDIF and an IDIF from ICA technique implemented using EPICA. The characteristics match well and the CMR_{glu} only varied by 5% between the two techniques. The arterial plasma input function is also shown. However, the statistical uncertainty may introduce bias in the metabolic rates, this bias can be reduced by using venous samples past later times, a method proved to give comparable binding potential values for [7-methyl-¹¹C]-(E)-8-(3,4,5-trimethoxystyryl)-1,3,7-trimethylxanthine ([¹¹C]TMSX) (Naganawa, 2007)

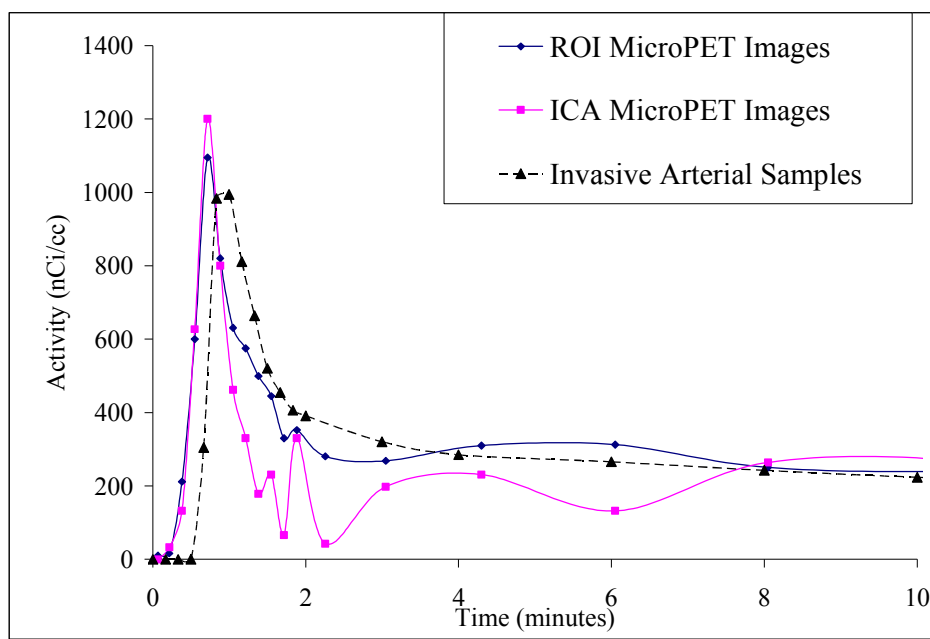


Figure6. Input functions obtained from invasive arterial samples, ROI and independent component analysis are compared

The need to correct for the peak of the IDIF obtained from ICA, limits the feasibility of this technique. The results from ICA did not differ from the input function extracted from dynamic images by drawing ROIs. Since the latter technique is not computationally intensive and relatively straight forward, it may be preferred over independent component analysis.

6.5 Future Work

Theoretically spatial resolution and sensitivity of current tomographs seem to be adequate for accurate quantification of the blood radioactivity concentration from blood vessels (ulnar/radial and internal carotid arteries) imaged in dynamic PET studies. Preceding chapters have shown that this goal can be partly achieved, requiring considerable image processing and providing with adequate results only in limited conditions. As predicted in figure 3.5 b; PET images acquired with the state of art tomograph should contain a number of voxels, at least in the largest blood vessels, which are not contaminated by partial volume effects. With the implementation of head motion correction methods (Bloomfield, 2003), the degradation of the spatial resolution frequently observed when studying human subjects should no longer be a limiting factor in derivation of reliable time-activity curves from small brain regions. These major technical developments open up new possibilities. Alternatively, sophistication of the system matrix used in iterative reconstruction algorithms could eventually allow the partial volume and spillover correction to be performed on sinogram data in the reconstruction rather than in the PET image post-reconstruction (Reader, 2007).

Need for venous samples for metabolite correction limit the technique presented from being totally non-invasive. Although invasive this technique requires only few temporally spaced samples to calibrate the wrist scanner and correct for presence of metabolites if any.

The technique explored in the thesis has only been validated completely for two C-11 based radiotracers, [^{11}C]raclopride and [^{11}C]clorgyline and will have to be validated for other tracers.

Appendix A

Description of the commercial robot system used for metabolite analysis.

Metabolite analysis in terms of identification of metabolic pathways of a compound of interest as well as quantification of their metabolic products for a given period of time has been shown to be a prerequisite for quantitative PET investigations and moreover to be of interest for a deeper understanding of physiological as well as pathological processes in the body.

Laboratory Automation System

Figure A1 shows the robot table configuration of laboratory automation hardware used at Brookhaven National Laboratory. The laboratory automation system (Zymark PyTechnology II) consisted of the following: (Alexoff, 1996)

- Py-Section™ compatible hardware/software modules from Zymark Corporation, Hopkinton, Massachusetts
- A Zymate II+ arm with Accutrak™ rotary feedback control or an XP robot arm
- A general purpose hand for manipulating 16 x 100 mm glass test tubes
- A 1 mL pipetting hand
- Two 50-position 16 x 100 mm test tube racks
- A six solvent Liquid/Solid Extraction PySection™
- A 3000 rpm centrifuge
- A Mettler AE200 balance PySection™
- A six solvent Dilute and Dissolve (w/vortex) PySection™
- Three Master Laboratory syringe pump PySections™
- A Power and Event Controller input/output PySection™

The Zymark's solid phase extraction station is modified to include liquid level sensing using an optical proximity detector. The SmartEye™ (Tritonics, Tampa, FL) detector is mounted to the BondElut station just under the pneumatic nozzle. Slotted brackets permit limited vertical, depth, and horizontal adjustment. The detector's output signal is used to verify the presence of a cartridge and to control the duration of solvent elution on the cartridge.

A custom "PySection" for radioactivity measurement using a NaI (3 inch crystal) well counter was constructed and interfaced with Zymark's PyTechnology system. The custom PySection accepts standard 16 x 100 mm test tubes and provides a two-position lead rack for temporary sample storage. A Plexiglas insert for the well counter was built to locate reproducibly a 16 x 100 mm test tube in the center of the well. An extraction cartridge parking station made from rubber stopper, mounted upside down, also resides on the lead rack. The robot turns a standard extraction cartridge upside down and rests it on the inverted stopper attached to the lead rack. The stopper ensures that the cartridge remains upright while the robot positions itself to regrip the cartridge at the standard container grip position before inserting it into the well counter. The hazardous waste station consists of a three-tiered disposal system designed for recycling and sorting solid waste. Empty cartridges used for purging the solvent delivery lines to the solid phase extraction station are recycled by the robot. Plasma-contaminated cartridges and test tubes are sorted and placed directly into appropriate waste containers (sharps for human waste) residing directly on the robot table. The waste is sterilized before disposal.

The laboratory automation system is controlled by a custom microcomputer and operating system named System V (ver. 1.52) running System Productivity Software (SPS) version 1.3. This system is controlled remotely from an IBM PS/2 Model 60 microcomputer running DOS 3.30 using Zymark's high speed serial interface and PCREMOTE software. The PSI2 is also connected via RS-232 to standard NIM electronics interfacing the NaI well counter. The signal output from the counter/timer is connected to one of the robot's digital inputs (TTL) at the Power and Event Controller.

This signal allows the robot to determine when the counter has finished counting a sample.

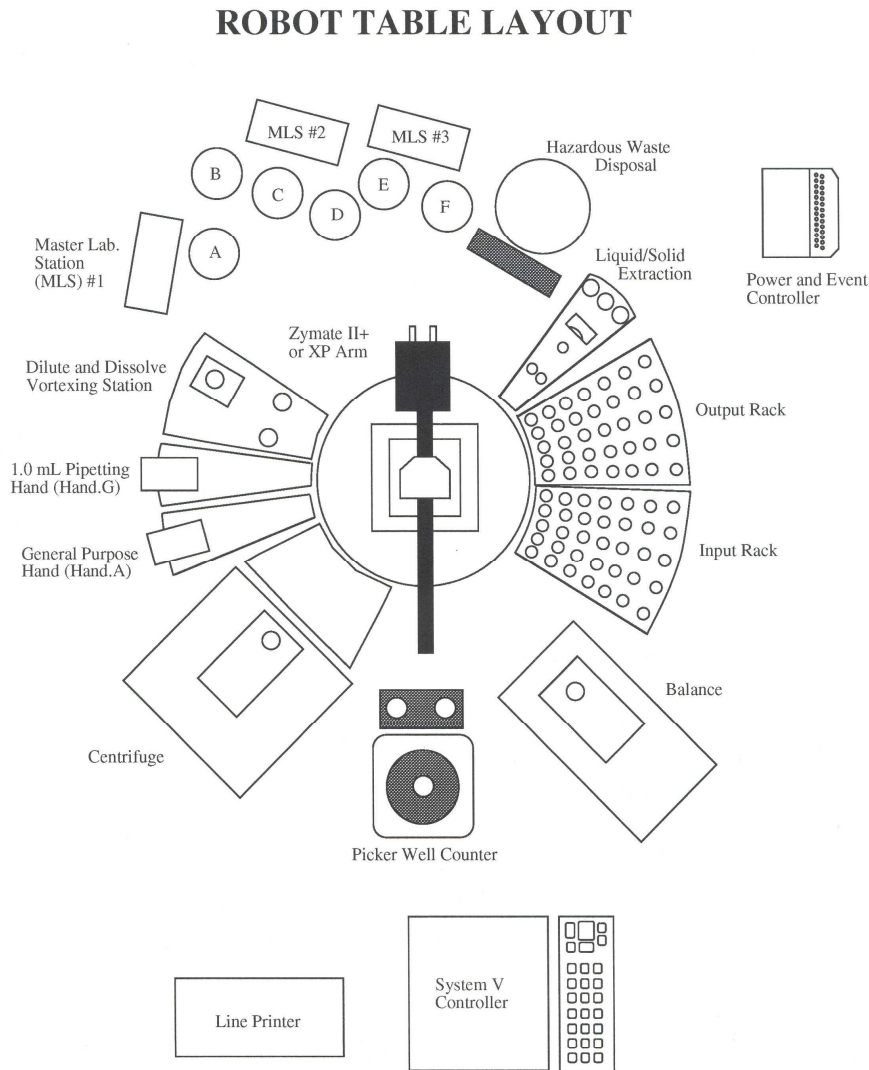


Figure A1. Robot table (5' x 8') diagram depicting physical layout of all robot hardware required for automated (Courtesy David Alexoff)

Plasma radioactivity assay

Arterial whole blood samples (0.2-0.4 mL) are obtained with an automated blood sampling device (Ole Dich, Denmark) every 2.5 s for 2 min post-injection of the tracer.

Blood samples are stored in heparinized 1.5 mL Eppendorf centrifuge tubes that are manually inserted (cap off) down to the bottom of 16 x 100 test tubes residing in the robot's input rack. Samples were centrifuged (3000 rpm for 2 min), pipetted, weighed, and counted in a NaI well counter by the robot automatically. An iterative, gravimetric feedback control algorithm was developed to obtain sufficient plasma free of red blood cells for radioactivity counting by the robot. The algorithm uses the value of the PET subject's hematocrit and the maximum whole blood volume in all the tubes to calculate a "safe vertical distance" (3 mm) above the calculated cell interface. This distance is about two times the vertical reproducibility specification of the robot. After the robot positions the pipette tip at the calculated safe vertical position, the computer program calculates the volume of plasma above this position and draws up a volume corresponding to this estimate. This plasma aliquot is then weighed in a tared 16 x 100 mm tube. If the weight exceeds 0.020 g, the sample is counted. If the weight is less than 0.020 g, an additional plasma aliquot is drawn in the following manner. Since the volume of plasma the robot attempted to draw when the pipette tip was nominally 3 mm above the first estimate of the cell plasma interface is known, a revised estimate of the maximum whole blood volume can be made by subtracting the calculated pipette volume from the original estimate of the whole blood volume. This revised estimate of the volume of whole blood is used to calculate a new position of the cell plasma interface and a new safe vertical distance. The pipette tip is repositioned at this new level and another aliquot is drawn. This process continues until either a total plasma weight of more than 0.020 g is reached or when the calculated volume of whole blood is less than 0.075 mL.

Solid Phase Extraction (SPE) parent compound assays human plasma (0.05-1.0 mL) is added to 3 mL water and stored at room temperature before being applied onto activated BondElut cartridges that are pre-loaded with 2 mL deionized water. These combined water and plasma volumes are termed the "dead volume." After application onto the cartridge, a series of solvent rinses is carried out sequentially by the robot to remove the metabolite fractions. For each parent compound assay, the robot measures the radioactivity of the sample tube before and after pouring onto the SPE cartridge, and assays the radioactivity of the dead volume and each of the solvent washes. A regulated

nitrogen gas pressure of 6-10 psi is used to drive liquid through the column. The radioactivity of the rinsed SPE cartridge is measured before disposal. All liquid fractions and empty sample tubes are stored in the test tube racks until automated clean-up during the evening when each tube is emptied into the infectious waste container and then discarded in a large sharps container at the hazardous waste station.

This simultaneous sequence of events including shuffling tubes and cartridges, acquiring radioactivity data, and moving liquids through the cartridge continues until all the samples are processed. Typically eight samples are processed for each study using a sampling protocol of 1,5,10,20,30,45,60,90 minutes post injection.

The quantity of parent compound present in each plasma sample is reported as a percent of the total radioactivity based on the radioactivity measured in the "pure" fraction, usually the SPE cartridge, after correction for background radioactivity, container geometry-dependent counting efficiency, total radioactivity recovery, and radionuclide decay.

Most often the problem of separating all metabolites from the parent compound in a PET study can be reduced to the problem of separating more polar molecules from their larger more non-polar parent radiotracer. Only the radioactive metabolites need be separated, further simplifying the assay. Figure A2 shows the simple method development process used at Brookhaven National Laboratory to develop robotic SPE-only assays of PET radiotracers in plasma to meet these goals.

Results of a screening protocol that included a basic aqueous wash and several washes of varying methanol/water mixtures is presented in Figure A3. This figure shows a clear shifting of the [^{11}C]raclopride radioactivity from the mixtures of less methanol to more methanol as the polarity of the bonded-phase is decreased. These same bonded phases were used in a baboon experiment to determine the selectivity of the bonded phases for [^{11}C]raclopride and its radioactive metabolites at a single time-point post injection.

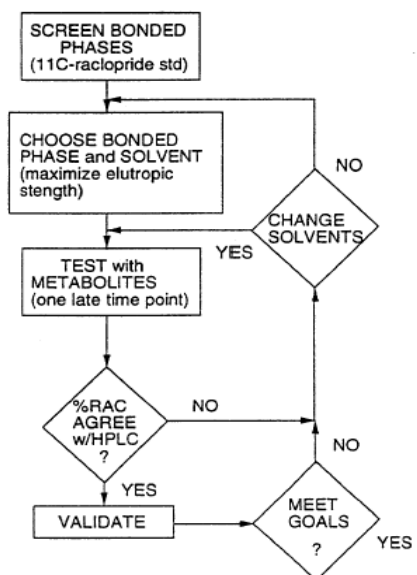


Figure A2: Simple SPE-only methods development strategy for non-polar extraction of parent compound from plasma. (Courtesy David Alexoff)

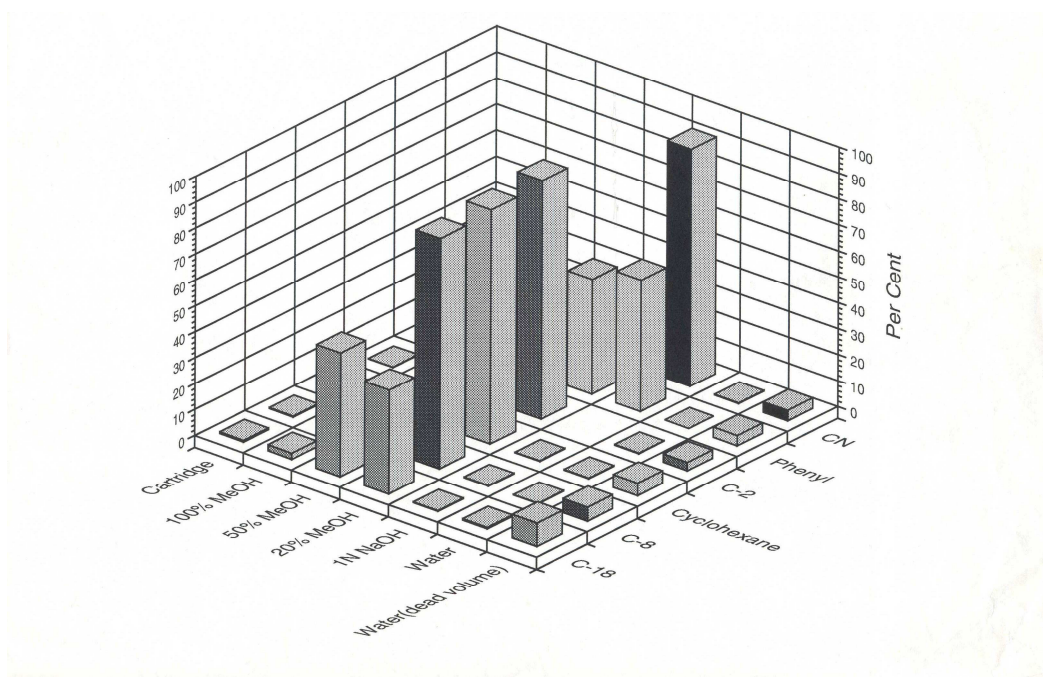


Figure A3: Results of non-polar extraction screening run with [11C]raclopride. (Courtesy David Alexoff)

The table below shows the robotic SPE metabolite assays.

¹¹ C radiotracer	SPE	Rinse1 (mL)	Rinse2 (mL)	Rinse3 (mL)	Unchanged*
Raclopride	CBA	Water (5)	pH 7 PB (5)	pH 7 PB (5)	CBA
Clorgyline	CN	Water (5)	100% ME		100% ME

CBA: Weak cation Exchange (carboxylic acid)

PB: Phosphate buffer

ME: Methanol

* Refers to the parent radiotracer. CBA means that the parent radiotracer is retained on weak cation exchange While 100% ME means that it is eluted in 100% methanol. Elution in this case is necessary since a label metabolite is also retained by the solid phase.

References

Alexoff D, Shea C, Fowler J, King P, Gatley S, Schlyer D, Wolf A Plasma input function determination for PET using a commercial laboratory robot Nucl Med Biol. Oct;22(7):893-904. 1995

Appendix B

Catalog of Independent Component Analysis: Motivation, Derivation and Process.

Most measured quantities are actually mixtures of other quantities. Typical examples are

- (a) sound signals in a room with several people talking simultaneously,
- (b) an electroencephalogram (EEG) signal, which contains contributions from many different brain regions, and
- (c) a person's height, which is determined by contributions from many different genetic and environmental factors.

Science is, to a large extent, concerned with establishing the precise nature of the component processes responsible for a given set of measured quantities. Under certain conditions, the signals underlying measured quantities can be recovered by making use of Independent Component Analysis (ICA). (Comon, 1994)

The success of ICA depends on one key assumption regarding the nature of the physical world. This assumption is that independent variables or signals are generated by different underlying physical processes. If two signals are independent, then the value of one signal cannot be used to predict anything about the corresponding value of the other signal. As it is not usually possible to measure the output of a single physical process, it follows that most measured signals must be mixtures of independent signals. Given such a set of measured signals (i.e., mixtures), ICA works by finding a transformation of those mixtures, which produces independent signal components, on the assumption that each of these independent component signals is associated with a different physical process. The measured signals are known as signal mixtures, and the required independent signals are known as source signals

The classical application of the ICA model is blind source separation. In blind source separation, the observed values of x correspond to a realization of an m dimensional discrete-time signal $x(t)$, $t = 1, 2, \dots$. Then the independent components $s_i(t)$ are called source signals, which are usually original, uncorrupted signals or noise sources. If two people are speaking simultaneously and there are two microphones held in different positions. The microphones gives two recorded time signals, which denoted $x_1(t)$ and $x_2(t)$, with x_1 and x_2 the amplitudes, and t the time index. Each of these recorded signals is a weighted sum of the speech signals emitted by the two speakers, $s_1(t)$ and $s_2(t)$. Expressing this as a linear equation,

$$\begin{aligned} x_1(t) &= a_{11}s_1 + a_{12}s_2 \quad (1) \dots\dots\dots B1 \\ x_2(t) &= a_{21}s_1 + a_{22}s_2 \quad (2) \dots\dots\dots B2 \end{aligned}$$

where a_{11}, a_{12}, a_{21} , and a_{22} are some parameters that depend on the distances of the microphones from the speakers. The task is now to separate the two original speech signals $s_1(t)$ and $s_2(t)$, using the recorded signals $x_1(t)$ and $x_2(t)$. This is called the cocktail-party problem. As an illustration, consider the waveforms in figure B1 and figure B2. The problem is to recover the data in Figure B1 (the original speech signals) using only the data in Figure B2 (the mixed signals) (Hyvärinen. 2001).

One approach to solving this problem would be to use some information on the statistical properties of the signals $s_i(t)$ to estimate the a_{ij} . It is assumed that $s_1(t)$ and $s_2(t)$, at each time instant t , are statistically independent. The technique of ICA, can be used to estimate the a_{ij} based on the information of their independence, which separates the two original source signals $s_1(t)$ and $s_2(t)$ from their mixtures $x_1(t)$ and $x_2(t)$. Figure B3 gives the two signals estimated by the ICA method. As can be seen, these are very close to the original source signals (their signs are reversed, but this has no significance.)

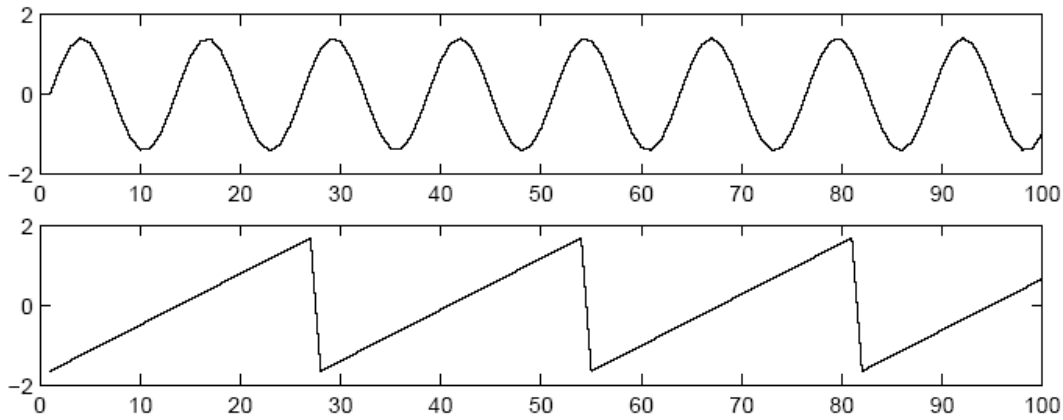


Figure B1: The original signals.

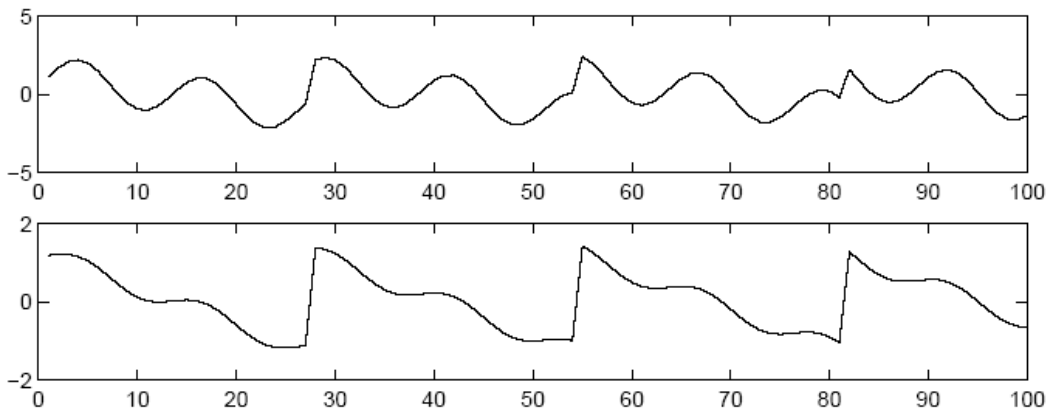


Figure B2: The observed mixtures of the source signals in Figure B1.

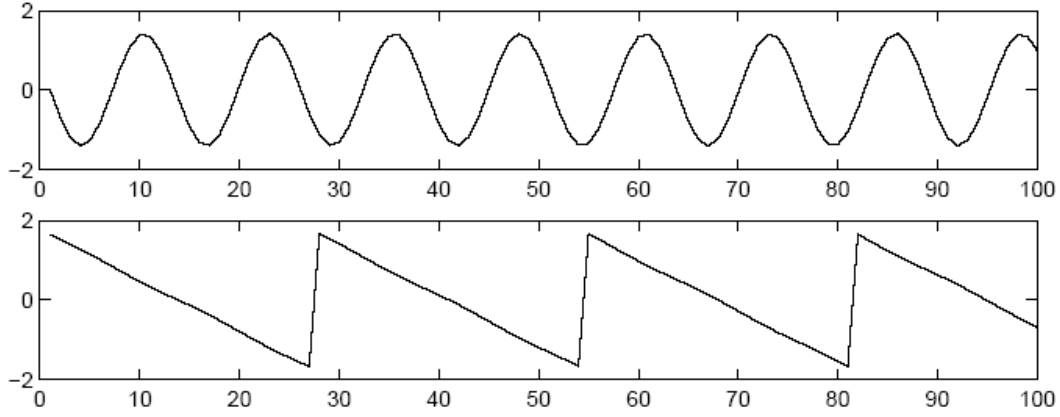


Figure B3: The estimates of the original source signals, estimated using only the observed signals in Figure. B2 The original signals were very accurately estimated, up to multiplicative signs

Another example is electrical recordings of brain activity as given by an electroencephalogram (EEG). The EEG data consists of recordings of electrical potentials in many different locations on the scalp. These potentials are presumably generated by mixing some underlying components of brain activity. This situation is quite similar to the cocktail-party problem: to find the original components of brain activity, but only mixtures of the components can be observed. ICA can reveal interesting information on brain activity observed giving access to its independent components.

Independent Component Analysis

Statistical independence

Denote by y_1, y_2, \dots, y_m some random variables with joint density $f(y_1, \dots, y_m)$, with zero-mean. The variables y_i are mutually independent, if the density function can be factorized:

$$f(y_1, \dots, y_m) = f_1(y_1)f_2(y_2)\dots\dots\dots f_m(y_m) \quad (B3)$$

where $f_i(y_i)$ denotes the marginal density of y_i . This property is called statistical independence.

Independence must be distinguished from uncorrelatedness, which means that

$$E\{y_i y_j\} - E\{y_i\}E\{y_j\} = 0; \text{ for } i \neq j: \quad (B4)$$

Independence is in general a much stronger requirement than uncorrelatedness. If the y_i are independent, then

$$E\{g_1(y_i)g_2(y_j)\} - E\{g_1(y_i)\}E\{g_2(y_j)\} = 0; \text{ for } i \neq j: \quad (B5)$$

for any 2 functions g_1 and g_2 . This is clearly a stricter condition than the condition of uncorrelatedness. There is, however, an important special case where independence and uncorrelatedness are equivalent. This is the case when y_1, \dots, y_m have a joint Gaussian distribution. Due to this property, independent component analysis is not possible for Gaussian variables.

Definitions of linear independent component analysis

In the literature, at least three different basic definitions for linear ICA can be found (Comon, 1994, Juten1991). In the definitions, the observed m -dimensional random vector is denoted by $x = (x_1, \dots, x_m)^T$.

The first and most general definition is as follows:

Definition 1 (General definition)

ICA of the random vector x consists of finding a linear transform $s = Wx$ so that the components s_i are as independent as possible, in the sense of maximizing some function $F(s_1, \dots, s_m)$ that measures independence. This definition is the most general in the sense that no assumptions on the data are made, which is in contrast to the definitions below.

Definition 2 (Noisy ICA model)

ICA of a random vector x consists of estimating the following generative model for the data:

$$x = As + n \quad (B6)$$

where the latent variables (components) s_i in the vector $s = (s_1, \dots, s_n)^T$ are assumed independent. The matrix A is a constant $m \times n$ 'mixing' matrix, and n is a m -dimensional random noise vector. This definition reduces the ICA problem to ordinary estimation of a latent variable model. However, this estimation problem is not very simple, and therefore the great majority of ICA research has concentrated on the following simplified definition:

Definition 3 (Noise-free ICA model)

ICA of a random vector x consists of estimating the following generative model for the data:

$$x = As \quad (B7)$$

where A and s are as in Definition 2.

Here the noise vector has been omitted. The noise-free model is considered a tractable approximation of the more realistic noisy model.

Relations to classical methods

ICA is closely related to several of the methods used for blind source separation problem

1. By definition, ICA can be considered a method for achieving redundancy reduction. Indeed, there is experimental evidence that for certain kinds of sensory data, the conventional ICA algorithms do find directions that are compatible with existing neurophysiological data, assumed to reflect redundancy reduction (Hyvärinen, 1999)

2. In the noise-free case, the estimation of the ICA model means simply finding certain 'interesting' projections, which give estimates of the independent components. Thus ICA can be considered, a special case of projection pursuit. The conventional criteria used for finding the 'interesting' directions in projections pursuit coincide essentially with the criteria used for estimating the independent components.

3. Another close affinity can be found between ICA and blind deconvolution. Due to the assumption that the values of the original signal $s(t)$ are independent for different t , this problem is formally closely related to the problem of independent component analysis. Indeed, many ideas developed for blind deconvolution can be directly applied for ICA, and vice versa.

4. In factor analysis, the following generative model for the data is postulated:

$$x = As + n \quad (B8)$$

where x is the vector of the observed variables, s is the vector of the latent variables (factors) that cannot be observed, A is a constant $m \times n$ matrix, and the vector n is noise, of the same dimension, m , as x . All the variables in s and n are assumed to be Gaussian. In addition, it is usually assumed that s has a lower dimension than x . Thus, factor analysis is basically a method of reducing the dimension of the data, in a way similar to Principal Component Analysis (PCA).

Comparing equation B6 in Definition 2 with the definition of factor analysis (B8), the connection between factor analysis and ICA becomes clear. Indeed, ICA may be considered a non-Gaussian factor analysis. A combination of factor analysis and ICA can be obtained using factor rotations.

5. Using Definition 1, the relation to principal component analysis is also evident. Both methods formulate a general objective function that define the 'interestingness' of a linear representation, and then maximize that function. A second relation between PCA and ICA is that both are related to factor analysis, though under the contradictory assumptions of Gaussianity and non-Gaussianity, respectively. PCA and ICA define their objective functions in quite different ways. PCA uses only second-order statistics, while ICA is impossible using only second-order statistics. PCA emphasizes dimension reduction, while ICA may reduce the dimension, increase it or leave it unchanged.



Figure B4: The relations between ICA and some other methods. The lines show close connections, and the texts next to the lines show the assumptions needed for the connection. (Hyvärinen, 1999)

The connections between ICA and some other methods are illustrated in figure B4. The lines in the diagram indicate very close connections, under the assumptions given next to the lines. First, if no assumptions on the data are made, and in particular no noise is postulated in the data, ICA can be considered a method of exploratory data analysis, as projection pursuit. Indeed, using Definition 1, ICA means simply finding some interesting projections of the data. If a noisy data model is assumed, as in Definition 2, ICA can be considered a variation of factor analysis for non-Gaussian data. ICA according to Definition 3, or the noise-free ICA data model, is something between these two approaches. As for PCA, its connection to ICA can be considered indirect, since it can be used to perform factor analysis for Gaussian data.

References

- Comon C. Independent component analysis a new concept? *Signal Processing*, 36:287–314, 1994.
- Hyvärinen, A Survey on Independent Component Analysis *Neural Computing Surveys* 2, 94–128, 1999
- Hyvärinen A, Fast and robust fixed-point algorithms for independent component analysis, *IEEE Trans. Neural. Networks*, vol. 10, no. 3, pp. 626–634, May 1999.
- Hyvärinen A, Karhunen J, and Oja E, ICA by maximization of nongaussianity in *Independent Component Analysis*. New York: Wiley- Interscience ch. 10, pp. 165–202. 2001
- Jutten C and Herault J. Blind separation of sources, part I: An adaptive algorithm based on neuromimetic architecture. *Signal Processing*, 24:1–10, 1991.

Bibliography

Alexoff D, Shea C, Fowler J, King P, Gatley S, Schlyer D, Wolf A Plasma input function determination for PET using a commercial laboratory robot Nucl Med Biol. Oct;22(7):893-904. 1995

Aykac M, Hichwa RD, Watkins GL. Investigation of a Noninvasive Detector System for Quantitative [^{15}O] Water Blood Flow Studies in PET IEEE Trans Nucl Sci 48:31-37 2001

Badawi RD and Marsden PK Developments in component-based normalization for 3D PET Phys. Med. Biol. 44(2):571-594 1999

Bailey DL, Townsend DW, Kinahan PE, Grootenboer S and T Jones An investigation of factors affecting detector and geometric correction in normalisation of 3-D PET data. IEEE Trans. Nucl. Sci. 43(6), 3300-3307 1996

Bloomfield PM, Spinks TJ, Reed J, Schnorr L, Westrip A.M, Livieratos L, Fulton R, Jones T The design and implementation of a motion correction scheme for neurological PET Physics in Medicine and Biology, Volume 48, Number 8, pp. 959-978(20) 2003

Carson R E Precision and accuracy considerations of physiological quantitation in PET J. Cereb. Blood Flow Metab. 11 A45-5 1991

Casey ME and Nutt R A Multicrystal Two Dimensional BGO Detector System For Positron Emission Tomography IEEE Trans. Nucl. Sci. 33(1),460-463 1986

Casey ME and Hoffman EJ Quantitation in Positron Emission Computed Tomography: 7. A technique to reduce noise in accidental coincidence measurements and coincidence efficiency calibration J. Comput. Assist. Tomogr. 10,845-850 1986

Chen K, Bandy D, Reiman E, Huang S-C, Lawson M., Feng D, Yun L-S, Palant A Noninvasive Quantification of the Cerebral Metabolic Rate for Glucose Using Positron Emission Tomography and ^{18}F -Fluoro-2-Deoxyglucose, the Patlak Method, and an Image-Derived Input Function. J. Cereb. Blood Flow and Metab. 18, 716-723, 1998

Cherry SR, Shao Y, Silverman RW, Meadors K, Siegel S, Chatziioannou A, Young JW, Jones WF, Moyers JC, Newport D, Boitefnouchet A, Farquhar TH, Andreaco M, Paulus MJ, Binkley DM, Nutt R and Phelps ME MicroPET: A High Resolution PET Scanner for Imaging Small Animals IEEE Trans. Nucl. Sci., 44(3), 1161-1166 1997

Cherry S, Sorenson J, Phelps M Physics in Nuclear Medicine, 3rd Edition Saunders; 3 edition ISBN-10: 072168341X, 2003

Colsher JG Fully three-dimensional positron emission tomography

Phys. Med. Biol. 25(1) 103-115 1980

Cho ZH and Farukhi MR Bismuth Germanate as a Potential Scintillation Detector in Positron Cameras The Journal of Nuclear Medicine Vol. 18 No. 8 840-844 1977

Cobelli C, DiStefano JJ 3rd Am J Physiol. Parameter and structural identifiability concepts and ambiguities: a critical review and analysis Jul;239(1):R7-24 1980

Witherspoon ME and Muehllehner G, Treatment of axial data in three-dimensional PET J. Nucl Med. 28, 1717-1724 1987

Defrise M Implementation of three-dimensional image reconstruction for multi-ring positron tomographs Phys. Med. Biol. 35 1361-1372 1990

Defrise M A factorization method for the 3D X-ray transform Inverse Problems 11 983-994 1995

Defrise M, Kinahan PE, Townsend DW, Michel C, Sibomana M and Newport DF Exact and approximate rebinning algorithms for 3D-PET data IEEE Trans. Med. Imag. 16(2) 145-158 1997

Derenzo Phantom: Data Spectrum, Chappel Hill, North Carolina

Doshi N, Cherry S, and Silverman R Novel design of a modular detector for the maxpet breast cancer imaging system J. Nucl. Med. 40 278P, 1999

Dekemp RA, Nahmias C. Attenuation correction in PET using single-photon transmission measurement. Med Phys. 21:771-8 1994

Eriksson L, Kanno I. Blood Sampling Devices and Measurement Medical Progress through Technology 17:249-257 1991.

K Erlandsson 3D reconstruction for a multi-ring PET scanner by single-slice rebinning and axial deconvolution Phys. Med. Biol. 39 619-629 1994

Evans RD 1955 The Atomic Nucleus McGraw-Hill, New York, 1955

Feng D, Wang Z, Huang SC, A study on statistically reliable and computationally efficient algorithms for the measurement of local cerebral blood flow with positron emission tomography IEEE Trans Med Imag 12:182-188 1993

Feng D, Wong KP, Wu CM and Siu WC, A technique for extracting physiological parameters and the required input function simultaneously from PET image measurements: theory and simulation study. IEEE Trans. Inf. Technol. Biomed. 1 4, pp. 243-254 1997

Fowler J, Volkow N, Wang GJ, Pappas N, Logan J, Shea C, Alexoff D, MacGregor R, Schlyer D, Zezulkova I and Wolf A. Brain monoamine oxidase A inhibition in cigarette smokers Proc. Natl. Acad. Sci. USA Vol. 93, pp. 14065-14069, 1996

Gambhir SS, Schwaiger M, Huang SC, Krivokapich J, Schelbert HR, Nienaber CA, Phelps ME. "Simple Noninvasive Quantification Method for Measuring Myocardial Glucose Utilization in Humans Employing Positron Emission Tomography and Fluorine-18 Deoxyglucose" J Nucl Med 30:359-366. 1989.

Germano G, Chen B, Huang S-C, Gambhir S, Hoffman E, Phelps M Use of the abdominal aorta for arterial input function de termination in hepatic and renal PET studies. J Nucl Med 33:613-620, 1991

Gunn, R, Lammertsma A, Hume S, and Cunningham V, Parametric imaging of ligand receptor binding in PET using a simplified reference region model. NeuroImage 6, pp. 279–287, 1997.

S Grooten Correction for scatter in 3D brain PET using a dual energy window method Phys. Med. Biol. 41 2757-2774 1996

Hamacher, K., H. H. Coenen Efficient stereospecific synthesis of no-carrier added 2-[18F]-fluoro-2-deoxy-D-glucose using aminopolyether supported nucleophilic substitution J Nucl Med 27(2): 235-8. 1986

Huang S-C, Hoffman EJ, Phelps ME, Kuhl DE. Quantitation in positron emission computed-tomography: 2. effects of inaccurate attenuation correction. J Comput Assist Tomogr.; 3:804–14 1979

Hoffman EJ, Huang SC, Phelps ME and Kuhl DE Quantitation in Positron Emission Computed Tomography: 4. Effect of Accidental Coincidences. J Comput Assist Tomogr 5(3):391-400 1981

Hoffman EJ, Huang SC, Plummer D, Phelps ME. Quantitation in positron emission computed tomography: 6. Effect of nonuniform resolution J Comput Assist Tomogr. 6:987–999. 1982

Hoffman EJ, Guerrero TM, Germano G, Digby WM and Dahlbom M PET system calibrations and corrections for quantitative and spatially accurate images IEEE Trans. Nuc. Sci. 36(1), 1108-1112 1989

Hyvärinen A, Fast and robust fixed-point algorithms for independent component analysis, *IEEE Trans. Neural. Networks*, vol. 10, no. 3, pp. 626–634, May 1999.

Hyvärinen A, Karhunen J, and Oja E, ICA by maximization of nongaussianity in *Independent Component Analysis*. New York: Wiley- Interscience ch. 10, pp. 165–202. 2001

Huang S, Phelps M, Hoffman E, Sideris K, Selin C and Kuhl D Noninvasive determination of local cerebral metabolic rate of glucose in man Am J Physiol Endocrinol Metab 238: E69-E82 1980

Iida H, Rhodes CG, de Silva R, Araujo LI, Bloomfield PM, Lammertsma AA, Jones T Use of the left ventricular time activity curve as a noninvasive input function in dynamic oxygen-15 water positron emission tomography. J Nucl Med 33:1669-1677, 1992

Jacquez JA , Compartmental analysis in biology and medicine (2nd ed.), University of Michigan Press 1988

Jan S GATE: a simulation toolkit for PET and SPECT Phys. Med. Biol. 49 4543–61 2003

Jan S Monte Carlo simulation of the microPET FOCUS system for small rodents imaging applications IEEE Trans. Nucl. Symp. Conf. Rec. 3 1653–57 2005

Johnston JA, Some observations upon a new inhibitor of monoamine oxidase in brain tissue. Biochem. Pharmacol. 17, pp. 1285–1297 1968

Junnarkar SS, Purschke ML, Pratte JF, O'Connor P, and Fontaine R An FPGA-Based, 12-Channel TDC and Digital Signal Processing Module for the RatCAP PET Scanner IEEE Nuclear Science Symposium Conference Record, 2005.

Karp JS. Against: Is LSO the future of PET? Eur J Nucl Med 29:1525–8 2002

Karp JS, Muehllehner G, Qu H and Yan XH Singles Transmission in Volume-Imaging PET with a Cs-137 Source Phys. Med. Biol. 40 (5) 929-944 1995

Kessler R, Ellis JR, Eden M Analysis of emission tomographic scan data: limitations imposed by resolution and background J Comput Assist Tomogr 8:514–522, 1984.

Kinahan PE and Rogers JG Analytic 3D Image Reconstruction Using All Detected Events IEEE Trans. Nucl. Sci. 36(1), 964-968

Knoll Some puzzling effects of monoamine oxidase inhibitors Adv Biochem Psychopharmacol 5 393-408 1972

Knoll Radiation Detection and Measurement John Wiley and Sons (WIE); 2Rev Ed edition 1989

Kriplani A, Stoll SP, Schlyer DJ, Shokouhi S, Vaska P, Villanueva A.Jr, Woody CL, Light output measurements of LSO single crystals and 4/spl times/8 arrays: comparison of experiment with Monte Carlo simulations ; Nuclear Science Symposium Conference Record; Pages: 3036 - 3040 Vol.5 2003

Landaw EM, DiStefano JJ 3rd Multiexponential, multicompartmental, and noncompartmental modeling. II. Data analysis and statistical considerations *Am J Physiol.* 246(5 Pt 2):R665-77 1984

Lee JS, Lee DS, Ahn JY, Cheon G, Kim SK, Yeo JS, Seo K, Park KK, Chung JK, and Lee MC Blind separation of cardiac components and extraction of input function from H(2)(15)O dynamic myocardial PET using independent component analysis *J. Nucl. Med.*, vol. 42, no. 6, pp. 938-943 2001

Lewitt RM 1994 Three-dimensional image reconstruction for PET by multi-slice rebinning and axial image filtering *Phys. Med. Biol.* 39 321-339

Liptrot A, Adams K, Martiny L, Pinborg L, Lonsdale M, Olsen N, Holm S, Svarer C, and Gitte M. Knudsen Cluster analysis in kinetic modelling of the brain: a noninvasive alternative to arterial sampling *NeuroImage* 21, 483–493, 2004

Litton J, and Eriksson L, Transcutaneous Measurements of the Arterial Input Function in Positron Emission Tomography. *IEEE Trans. on Nuclear Science*, 37:627-628, 1990

Logan J, Fowler JS, Volkow N, Wolk AP, Dewey SL, Schlyer DJ, Macgregor RR, Hitzmann R, Bendriem B, Gatley SJ, Christman DR Graphical analysis of reversible radioligand binding from time-activity measurements applied to [N- 11C-methyl(-)-cocaine PET studies in human subjects. *J Cereb Blood Flow Metab* 10:740-747 1990

Logan J, Fowler JS, Volkow ND, Ding YS, Wang GJ, Alexoff DL. A strategy for removing the bias in the graphical analysis method. *J Cereb Blood Flow Metab.* 21(3):307-20, 2001

Logan J, Fowler JS. Evidence for reduced arterial plasma input, prolonged lung retention and reduced lung monoamine oxidase in smokers. *Nucl Med Biol.* 32:521–529 2005.

Ludziejewski, Moszynska Advantages and Limitations of LSO Scintillator in Nuclear Ph. 1995

MacGregor RR, Halldin C, Fowler J, Wolf A, Arnett C, Langström B, Alexoff D. Selective, irreversible in vivo binding of [11C]clorgyline and [11C]-L-deprenyl in mice: potential for measurement of functional monoamine oxidase activity in brain using positron emission tomography. *Biochem Pharmacol.* 34(17):3207-10. 1985

McGeer PL, McGeer EG, Suzuki JS. Aging and extrapyramidal. function. *Arch Neurol* 34:33–5. 1977

McGeer PL, Eccles JC, McGeer EG Molecular neurobiol-. ogy of the mammalian brain, 2nd edn. Plenum Press, New York 1987

McKeown MJ and Sejnowski TJ Independent component analysis of fMRI data: examining the assumptions *Hum. Brain Mapp.*, vol. 6, no. 5-6, pp. 368-372, 1998.

Meyer E Simultaneous correction for tracer arrival delay and dispersion in CBF measurements by the H215O autoradiographic method and dynamic PET. *J Nucl Med.* 30(6):1069-78 1989

Mintun MA, Raichle ME, Kilbourn MR, Wooten GF, Welch MJ A quantitative model for the invivo assessment of drug binding sites with positron emission tomography *Am Neurol* 15:217-227 1989

Moisan C Count Rate Model for PET and Its Applications to an LSO HR PLUS Scanner *IEEE* pp. 1186-1190 1997

Naganawa M, Kimura Y, Ishii K, Oda K, Ishiwata K, and Matani A Extraction of a plasma time activity curve from dynamic brain PET images based on independent component analysis," *IEEE Trans. Biomed. Eng.* vol. 52, no. 2, pp. 201-210, Feb.2005.

Naganawa M, Kimura Y, Ishii K, Oda K, Ishiwata K, and Matani Quantification of adenosine A2A receptors in the human brain using [11C]TMSX and positron emission tomography *Eur J Nucl Med Mol Imaging* 34:679–687 2007

National Electrical Manufacturers Association, “Performance Measurements of Positron Emission Tomographs,” NU 2-1994, 1994.

Nishizawa, Leyton M, Okazawa H, Benkelfat C, Mzengeza S and Diksic M Validation of a Less-Invasive Method for Measurement of Serotonin Synthesis Rate With α - [11C]Methyl-Tryptophan *Journal of Cerebral Blood Flow & Metabolism* 18, 1121–1129; 1998

Nutt R. Is LSO the future of PET? *Eur J Nucl Med*; 29 1523–1524 2002

JM Ollinger Detector efficiency and Compton scatter in fully 3D PET *IEEE Trans. Nucl. Sci.* 42(4) 1168-1173 1995

JM Ollinger Model-based scatter correction for fully 3D PET *Phys. Med. Biol.* 41 153-176 1996

John M. Ollinger and Jeffrey A. Fessler. Positron-emission tomography. *IEEE Signal Processing Magazine*, January:43–55, 1997.

Pajevic S, Daube-Witherspoon M.E, Bacharach S.L, Carson R.E, Noise characteristics of 3-D and 2-D PET images Div. of Comput. Res. & Technol., Nat. Inst. of Health, Bethesda, MD 1998

Patlak C, Blasberg RG, Fenstermacher JD (1983) Graphical evaluation of blood-to-brain

transfer constants from multiple-time uptake data. J Cereb Blood Flow Metab 3:1-7.

Patlak C, Blasberg RG (1985) Graphical evaluation of blood-to-brain transfer constants from multiple-time uptake data. Generalizations. J Cereb Blood Flow Metab 5:584-590.

Phelps, M.E., Huang, S.C., Hoffman, E.J., Selin, C., Sokoloff, L., and Kuhl, D.E., Tomographic Measurement of Local Cerebral Glucose Metabolic Rate in Humans with (F-18)2-Fluoro-2-Deoxy-D-Glucose: Validation of Method. Neurol. 6:371-388, 1979.

Phelps M, Mazziotta J and Schelbert H. Positron emission tomography and autoradiography - principles and applications for the brain and heart Raven Press, ISBN 0-88167-118-5, 1986

Pike V Positron-emitting radioligands for studies in vivo-probes for human psychopharmacology. J Psychopharmacol 7, 139-158 1993

Pratte J.-F, De Geronimo G, Junnarkar S, O'Connor P, Yu B, Robert S, Radeka V, Woody C, Stoll S, Vaska P, Kandasamy A, Lecomte R, Fontaine R Front-end electronics for the RatCAP mobile animal PET scanner IEEE Transactions on Nuclear Science, 51(4): 1318 – 1323 2004

Pratte J-F, Robert S, De Geronimo G, O'Connor P, Stoll S, Pepin C.M, Fontaine R, Lecomte R Design and performance of 0.18 μ m CMOS charge preamplifiers for APD-based PET scanners IEEE Transactions on Nuclear Science, 51(5) 2004.

Proteus, Inc. 120 Senlac Hills Drive, Chagrin Falls, OH 44022, <http://www.apacescience.com/proteus/>

Purschke M, Fontaine R, Junnarkar S, Krishnamoorthy S, O'Connor P, Pratte, J-F., Schlyer D, Stoll S, Vaska P, Villanueva A, and Woody C, The Data Acquisition System of the RatCAP Conscious Small Animal PET Tomograph IEEE Nuclear Science Symposium Conference Record, 2005.

Rajeswaran S, Bailey DL, Hume SP, Townsend DW, Geissbuhler A, Young J, Jones T. 2-D and 3-D Imaging of Small Animals and the Human Radial Artery with a High Resolution Detector for PET IEEE Trans Med Imaging 11:386-391 1992

Rannou F R, Kohli V, Prout D L and Chatziioannou A F Investigation of OPET performance using GATE, a Geant4-based simulation software IEEE Trans. Nucl. Sci. 51 2713–17 2004

Reader AJ, Matthews JC, Sureau FC, Comtat C, Trebossen, R.; Buvat, I. Iterative Kinetic Parameter Estimation within Fully 4D PET Image Reconstruction Nuclear Science Symposium Conference Record, 2006. IEEE Volume 3, Oct. 29 Page(s):1752 – 1756 2006

Rey M, Simon L, Strul D, Viera J M and Morel C Design study of the ClearPET LSO/LuAP phoswich detector head using GATE Mol. Imag. Biol. 5 119 2003

Rickey DW, Gordon R and Huda W On lifting the inherent limitations of positron emission tomography by using magnetic fields (MagPET) Automedica, 14 355-369 1992

Richards RC Monoamine oxidases: from brain maps to physiology and transgenics to pathophysiology J Neural Transm Suppl 52 173-87 1998

Singer T Monoamine oxidases old friends hold many surprises FASEB J 9 605 610 1995

Strul D, Bendriem B. Robustness of anatomically guided pixel-by-pixel algorithms for partial volume effect correction in positron emission tomography. J Cereb Blood Flow Metab. May;19(5):547-59, 1999

Sokoloff L, Reivich M, Kennedy C, Des Rosiers MH, Patlak CS, Pettigrew KD, Sakurada O, Shinohara M. "The [¹⁴C]deoxyglucose method for the measurement of local cerebral glucose utilization: theory, procedure, and normal values in the conscious and anesthetized albino rat" J Neurochem May;28(5):897-916 1977.

Strother SC, Casey ME and Hoffman EJ Measuring PET Scanner Sensitivity: Relating Count rates to Image Signal-to-Noise Ratios using Noise Equivalent Counts IEEE Trans. Nucl. Sci.37(2):783-788 1990

Takikawa S, Dhawan V, Spetsieris P, Robeson W, Chaly T, Dahl R, Margouleff D, Eidelberg D. Noninvasive Quantitative Fluorodeoxyglucose PET Studies with an Estimated Input Function Derived from a Population-based Arterial Blood Curve Radiology 188:131-136 1993.

Thompson C, Murthy K, Picard Y, and Weinberg N Positron emission mammography PEM: a promising technique for detecting breast cancer IEEE Trans. Nucl. Sci. 41, 1012–1017 1994

Vaska P, Stoll SP, Woody CL, Schlyer DJ, Shokouhi S. Effects of Inter-Crystal Cross Talk on Multi-Element LSO/APD PET Detectors IEEE Trans Nucl Sci, 2003

Voet and Voet Biochemistry, 2nd ed. John Wiley and Sons, Inc. New York.1995

Volkow N, Fowler J, Gatley J, Logan J, Wang GJ, Ding Y and Dewey S PET Evaluation of the Dopamine System of the Human Brain The Journal of Nuclear Medicine Vol. 37 No. 7 1242-1256 1996

Volkow ND, Fowler JS, Wang GJ, Dewey SL, Schlyer D, MacGregor R, Logan J, Alexoff D, Shea C, Hitzemann R, Reproducibility of repeated measures of carbon-11-raclopride binding in the human brain. J Nucl Med 34:609–613, 1993

Wahl L, Asselin MC, and Nahmias C Regions of interest in the venous sinuses as input functions for quantitative PET *Journal of Nuclear Medicine*, 40: 1666-1675, 1999.

Wahl R et al. Principles and practice of Positron Emission Tomography. Lippincott Williams & Wilkins, Philadelphia, PA, 2002

CC Watson, D Newport and ME Casey A single-scatter simulation technique for scatter correction in 3D PET 1996

Wang G-J, Volkow ND, Fowler JS, Logan J, Pappas NR, Wong CT, Hitzemann RJ, Netusil N. Reproducibility of repeated measures of endogenous dopamine competition with [^{11}C]raclopride in the human brain in response to methylphenidate. *J Nucl Med.* 40: 1285-1291 1999.

Weinberg SC. Huang J. Hoffman L. Araujo, C. Nienaber, M. Grover McKay, M. Dahlbom and H. Schelbert Validation of PET-Acquired Input Functions for Cardiac Studies *Journal of Nuclear Medicine* Vol. 29 No. 2 241-247 1988

Wu HM, Huang SC, Allada V, Wolfenden PJ, Schelbert HR, Phelps ME, and Hoh CK, Derivation of input function from FDG-PET studies in small hearts *J. Nucl. Med.*, vol. 37, no. 10, pp. 1717-1722, Oct.1996.

Wu HM, Hoh C, Choi Y, Schelbert HR, Hawkins RA, Phelps ME and Huang SC, Factor analysis for extraction of blood time-activity curves in dynamic FDG-PET studies *J. Nucl. Med.*, vol. 36, no. 9, pp. 1714-1722, Sept.1995.

Xu M, Luk WK, Cutler PD, Digby WM, Local threshold for segmented attenuation correction of PET imaging of the thorax *Nuclear Science, IEEE Transactions on* Volume 41, Issue 4, Page(s):1532 – 153 1994

Xuan L, Defrise M, Michel C, Sibomana M, Comtat C, Kinahan P, Townsend D, Exact rebinning methods for three-dimensional PET Medical Imaging, *IEEE Transactions on* Volume 18, Issue 8, Page(s):657 – 664 1999

Yu, S. K.; Nahmias, C Single-photon transmission measurements in positron tomography using ^{137}Cs *Physics in Medicine and Biology*, Volume 40, Issue 7, pp. 1255-1266 1995